LIFETIMES OF EXCITED NUCLEAR STATES

BY DELAYED COINCIDENCE

LIFETIMES OF EXCITED STATES OF NUCLEI IN THE MASS RANGE 28<A<56 BY DELAYED COINCIDENCE

By

JAMES FREDERICK BOULTER, B.Sc., M. Sc.

A Thesis
Submitted to the School of Graduate Studies
in Partial Fulfilment of the Requirements
for the Degree
Doctor of Philosophy

McMaster University

May 1971

DOCTOR OF PHILOSOPHY
(Physics)

McMASTER UNIVERSITY
Hamilton, Ontario.

TITLE: Lifetimes of Excited States of Nuclei in the Mass Range $28<A<56$ by Delayed Coincidence

AUTHOR: James Frederick Boulter, B.Sc. (Dalhousie University)
M.Sc. (Dalhousie University)

SUPERVISOR: Professor W. V. Prestwich

NUMBER OF PAGES: 176, vx

SCOPE AND CONTENTS:

A study of the inter-multiplet M1 transition probability for states populated by the (n,γ) reaction in a number of odd-odd nuclei has been performed. Using a high resolution delayed coincidence system and specially developed calibration and data analysis techniques, lifetime measurements have been made for low energy transitions in ^{28}Al, ^{32}P, ^{40}K, ^{46}Sc, ^{52}V and ^{56}Mn. A theoretical model which uses the static magnetic dipole moments of the corresponding odd-A nuclei as the base states has been investigated and was shown able to produce a very satisfactory agreement with the experimental intermultiplet B(M1) values.

ACKNOWLEDGMENTS

It is a pleasure to thank my supervisor Dr. W. V. Prestwich. I have greatly benefitted from his many insights and from his stimulating and original approach to physics. His expert and timely advice has always been given clearly and with much enthusiasm.

I also wish to thank Dr. T. J. Kennett for his advice and encouragement and for many good natured discussions.

I am most appreciative to all others at McMaster University who created the very congenial atmosphere in the nuclear physics department. In particular I wish to thank Dr. B. Arad, Mr. P. R. Gardner, Mr. A. M. Lopez and Mr. L. M. Lowe for their many useful suggestions and discussions.

I am grateful to the staff of the McMaster Reactor for their cooperation and help and to the staff of the McMaster Computer Centre for their programming assistance.

The generous financial support provided by McMaster University and by the Ontario Department of University Affairs is gratefully acknowledged.

Finally, but in no sense least, I am indebted to Mrs. Sue Anderson, who accurately and patiently performed the difficult task of typing the manuscript.

ABSTRACT

Using a beam of thermal neutrons obtained from the McMaster reactor, the (n,γ) reaction has been used to populate levels in a number of odd-odd nuclei in the mass range $28 \leq A \leq 56$, and the following delayed coincidence lifetime measurements were performed:

^{28}Al	(31.2 keV level)	$T_{1/2} = 2.15 \pm 0.06$ ns
^{32}P	(77 keV level)	$T_{1/2} = 253 \pm 25$ ps
^{40}K	(29.4 keV level)	$T_{1/2} = 4.26 \pm 0.08$ ns
^{46}Sc	(52 keV level)	$T_{1/2} = 9.62 \pm 0.50$ μs
^{52}V	(17.0 keV level)	$T_{1/2} = 1.08 \pm 0.22$ ns
^{56}Mn	(26.6 keV level)	$T_{1/2} = 8.70 \pm 0.50$ ns
^{56}Mn	(110 keV level)	$T_{1/2} = 5.08 \pm 0.20$ ns

The conversion coefficient of the 17 keV transition in ^{52}V was measured to be $\alpha_{exp} = 4.6 \pm 1.8$ implying a 90% M1 and 10% E2 assignment.

Five of the measured lifetimes can be considered as resulting from transitions between members of the ground state multiplet, and these cases have been interpreted (correlation coefficient $\rho = 0.98$ for $N = 7$) using a model with no fitted parameters in which the static magnetic dipole moments of the neighbouring odd-A nuclei are taken as the base states. This high correlation was reduced to $\rho = 0.87$ when pure shell model

states (i.e. the Schmidt limits), were used in the calculation, indicating that significant nuclear structure effects are manifested in this approach.

An experimental and theoretical examination of the time resolution of a delayed coincidence system, and in particular, the effect of the production of Čerenkov light, was performed. Several new data aquisition and analysis techniques have been investigated and a time-scale calibration procedure which uses a 100 Mhz crystal oscillator as the standard has been developed.

TABLE OF CONTENTS

LIST OF FIGURES

LIST OF TABLES

CHAPTER I

INTRODUCTION

A. General Considerations

An investigation of low energy nuclear structure, and in particular the lifetimes of excited nuclear states in odd-odd nuclei, is described in this thesis. The time which a nucleus exists in an excited state before decaying to a lower energy state follows an exponential distribution; i.e. if N_o nuclei are produced in an excited state, the number remaining in that state after a time t has elapsed is given by

$$N = N_o \, e^{-t/\tau}$$

An exponential mean life, τ, or a transition probability, $T = 1/\tau$ can then be associated with each excited state, and the correct prediction of experimental results provides a sensitive test for any proposed model for the nucleus.

Mean lives in the range $10^{-3} \leq \tau \leq 10^{-10}$ seconds can be directly measured using electronic techniques. In the delayed coincidence method employed here, separate detectors were used to detect the γ radiation signifying the population and depopulation of the

excited state, and the time interval between the 2 events was then electronically measured and recorded. The optimization and calibration of the experimental system, and the methods of data analysis are discussed in the following chapters along with experimental lifetime results for excited states in 6 nuclei.

Under certain limitations, a reasonable description of some nuclear properties can be obtained using the extreme single particle model for the nucleus described in the later sections of this chapter. Within the framework of this model, and for the type of transition classified as inter-multiplet M1, a relatively simple theory is developed in chapter VI which produces a very satisfactory agreement with the experimental lifetime measurements.

B. Single Particle Model for the Nucleus

A nucleus can be pictured as an assembly of neutrons and protons moving around the centre of mass in certain orbits. Inside the nucleus, each nucleon (bound neutron or proton) possesses an intrinsic angular momentum, described by the spin quantum number $s = 1/2$, and a quantized orbital angular momentum described by the integral quantum number ℓ. Depending on their relative orientation, the spin and orbital angular momentum of each nucleon couple to a total

angular momentum, with half integral quantum number j, which is equal to either $j = \ell + s$ or $j = \ell - s$. A single particle state with orbital angular momentum quantum number ℓ has a parity, π, equal to $(-1)^{\ell}$.

In the extreme single particle model, the spins of like nucleons are assumed to pair off so as to form an inert core consisting of closed neutron and proton shells. For a nucleus consisting of either an odd number of neutrons or protons, the low energy properties are determined by the unpaired nucleon. This nucleon can be excited out of the state of lowest energy (ground state) into a discrete number of higher energy orbits, each characterized by a spin and parity. If there is an odd number of both nucleons, the nuclear states are formed by coupling the spins of the odd neutron and proton.

C. States in Odd-Odd Nuclei

Consider the ground state of 2 odd-A nuclei: one consisting of an inert core + a proton in a state with spin j_p and parity π_p, and a second consisting of this same core + a neutron with spin j_n and parity π_n. In the corresponding odd-odd nucleus, consisting of the core + a neutron and proton, the two nucleons

will couple to form a multiplet of states, all with parity $\pi = \pi_n \pi_p$ and with different spins ranging in integral steps from $| j_n - j_p |$ to $j_n + j_p$. If there is no residual interaction between the neutron and proton the members of the multiplet will all lie at the same energy. This degeneracy will be removed if a direct interaction, V_{np}, takes place between the 2 nucleons. For 2 states with spins J_1 and J_2 belonging to the same multiplet, the energy splitting:

$$E_J = \langle J_1 | V_{np} | J_2 \rangle \qquad \text{I.1}$$

can be calculated if a particular form for V_{np} is assumed (e.g. p. 172 in (PR62)). General rules for predicting the energy ordering of the multiplet states have been given by Nordheim (NO50) and more recently by Brennen and Bernstein (BR60).

Because of this energy splitting, the multiplets representing different neutron-proton shell model configurations can lie close in energy. If the states from neighbouring multiplets have the same spin and parity, significant mixing of the 2 states can take place. This configuration mixing is caused by the same neutron-proton interaction which is responsible for the intermultiplet energy splitting. By a direct diagonalization of the 4 element interaction matrix, it follows

(e.g. PR62), that for a multiplet state Ψ_1 at energy E_1, the amount of admixture of a state Ψ_2 at energy E_2 with the same spin and parity, but from a different multiplet, depends on the ratio of the neutron-proton interaction energy to the energy difference between the 2 states. The state Ψ_1 will then be modified to:

$$\Psi_1' = \Psi_1 + \frac{(\Psi_1|V_{np}|\Psi_2)}{E_1 - E_2} \times \Psi_2$$

An example of this coupling of neutron and proton states to form states in an odd-odd nucleus is illustrated in Fig. I.1. A neutron in the ground state $\Psi_1(n)$, with spin $J_1(n)$ and parity $\pi_1(n)$ is coupled to a ground state proton $\Psi_1(p) = J_1(p), \pi_1(p)$ to form the degenerate multiplet of states:

$$\Psi_1 = \pi_1(n)\ \pi_1(p), \sum_{i=1}^{r} \Psi_1(J_i)$$

where the summation is carried out over all possible neutron-proton couplings. As the neutron-proton interaction is applied, the r degenerate states move apart in energy to take up the positions, $E_1(J_i)$, predicted by Eq. I.1. A second multiplet of states $\pi_1(n)\pi_2(p), \sum_{i=1}^{S} \Psi_1(J_i)$, with energies $E_2(J_i)$, was formed by coupling the neutron ground state to an excited proton state $\Psi_2(p) = J_2(p)\ \pi_2(p)$, at energy E_p. If, for

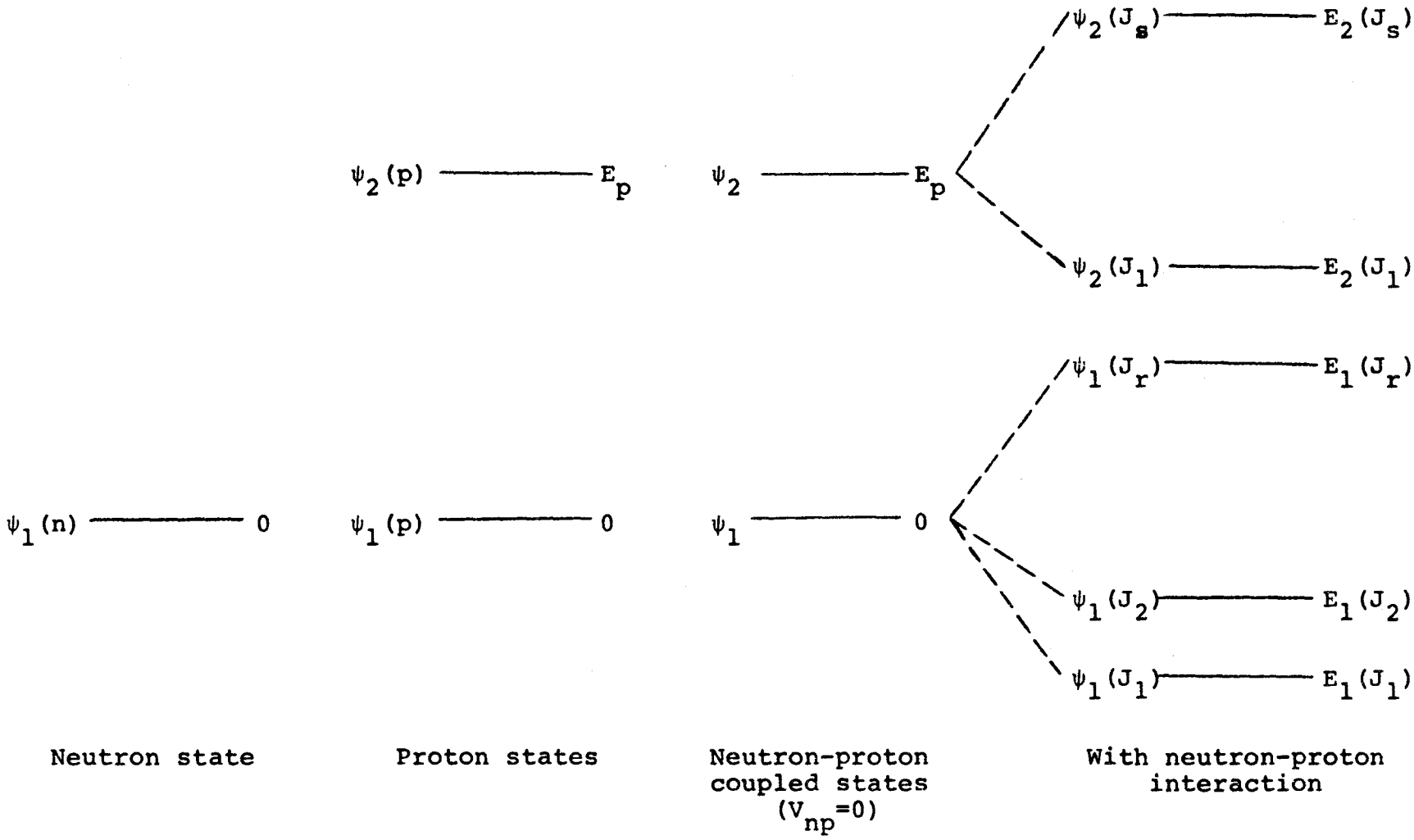

Fig. I.1 Coupling of neutron and proton single particle states in odd-A nuclei to form states in the corresponding odd-odd nucleus. The lower multiplet of states is formed by coupling the proton and neutron ground states while the upper multiplet results from coupling the neutron ground state to the proton excited state at E_p.

example, the 2 multiplets have the same parity and the neighbouring levels Ψ_1 (J_r) and Ψ_2 (J_1) have the same spin, and further if the energy difference $E_2(J_1)-E_2(J_r)$ is comparable to the neutron-proton interaction energy:

$$E = \langle \Psi_2(J_1) \; |V_{np}| \; \Psi_1(J_r) \rangle$$

then each state could be expected to include a mixture of the other. Since some nuclear properties, e.g. static magnetic moments (PR62), are particularly sensitive to the shell model configuration, even a small amount of mixing from a different multiplet can have an appreciable effect.

D. Inter-Multiplet γ-Ray Transitions

In the γ-ray transition between excited nuclear states, the nucleus can be considered as an oscillating electric or magnetic multipole of order λ. For a nucleus in an initial state characterized by spin J_i, parity π_i and energy E_i, changing to a final state (J_f, π_f, E_f) by an electric (Eλ) or magnetic (Mλ) transition, the γ-ray selection rules require that:

$$E_i - E_f = E_\gamma$$

$$|J_i - J_f| = \lambda \geq 1$$

$$\pi_i \, \pi_f = (-1)^{\lambda} \quad \text{for electric transitions}$$

$$= (-1)^{\lambda+1} \quad \text{for magnetic transitions}$$

This thesis is concerned with the measurement and interpretation of the magnetic dipole (M1) transition probability between members of the ground state multiplet for a number of odd-odd nuclei. As discussed in the previous section, states which are assumed to be pure members of a multiplet can also have a mixture of a different single particle state. Hence to first order the M1 transition probability between such states will consist of 2 components: one involving a recoupling of neutron and proton spins only (i.e. a true intermultiplet transition which for M1 corresponds to a neutron or proton spin flip); and a second component involving a single particle transition in which the neutron or proton jumps to a new shell model orbit. In addition, electron conversion (transfer of the nuclear excitation energy to an atomic electron) and emission of higher order multipole γ-radiation (only M1-E2 mixtures are expected to be significant and the E2 component requires the sum $J_i + J_f \geq 2$), can compete with the M1 component. While the effect of conversion and an E2 mixture can be obtained independently from other experiments, the relative size and strength of the single particle component is not readily measurable. A further discussion of this configuration mixing, and of other effects such as collective motion and interference, which are not included in

the theoretical intermultiplet treatment of Chapter VI, will be given later.

E. (n,γ) Reaction

The odd-odd nuclei that were studied were produced by thermal neutron capture on stable odd-proton even-neutron nuclei. The neutron capture reaction leaves the product odd-odd nucleus in a state of excitation equal to the neutron binding energy ($\sim$ 7 - 8 MeV), so that lower lying states which are populated in the subsequent γ-ray decay of the nucleus can be studied.

Because of its low angular momentum with respect to the nucleus, the thermal neutron must be captured into an s ($\ell = 0$) neutron state. If the target nucleus has a ground state spin of j_t and a parity π_t, the capture state will then have the same parity with a spin of either $j_t + 1/2$ or $j_t - 1/2$. The strong El γ-transitions will lead to the predominant population of states of the opposite parity which have spins differing from the capture state by 1 unit of angular momentum. Secondary cascades or weaker transitions of a different multipole order are required to populate other states.

CHAPTER II

EXPERIMENTAL SYSTEM

A. Beam Port Arrangement

1. Shielding and Detector Geometry

The targets were irradiated using a thermal beam of 10^6 - 10^7 neutrons/sec^2 with a 1 cm diameter which was obtained from the number 1 beam port of the McMaster reactor. In order to reduce the fast neutron component, the beam was passed through either an 18" or 30" length of quartz crystal filtering. The action of this filter was to scatter high energy neutrons which had wavelengths comparable to the crystal lattice spacing, out of the beam into a surrounding absorber, while passing, with only a small attenuation, the longer wavelength thermal neutrons.

Neutron scattering into the detectors and surrounding material was reduced by enclosing the beam and target in an ^{6}LiF annulus, while the detectors and the portion of the ^{6}LiF annulus containing the target were enclosed in graded lead γ-ray shielding. The shielding and detector geometry is illustrated in Fig. II.1. In order to minimize attenuation of low energy γ-rays,

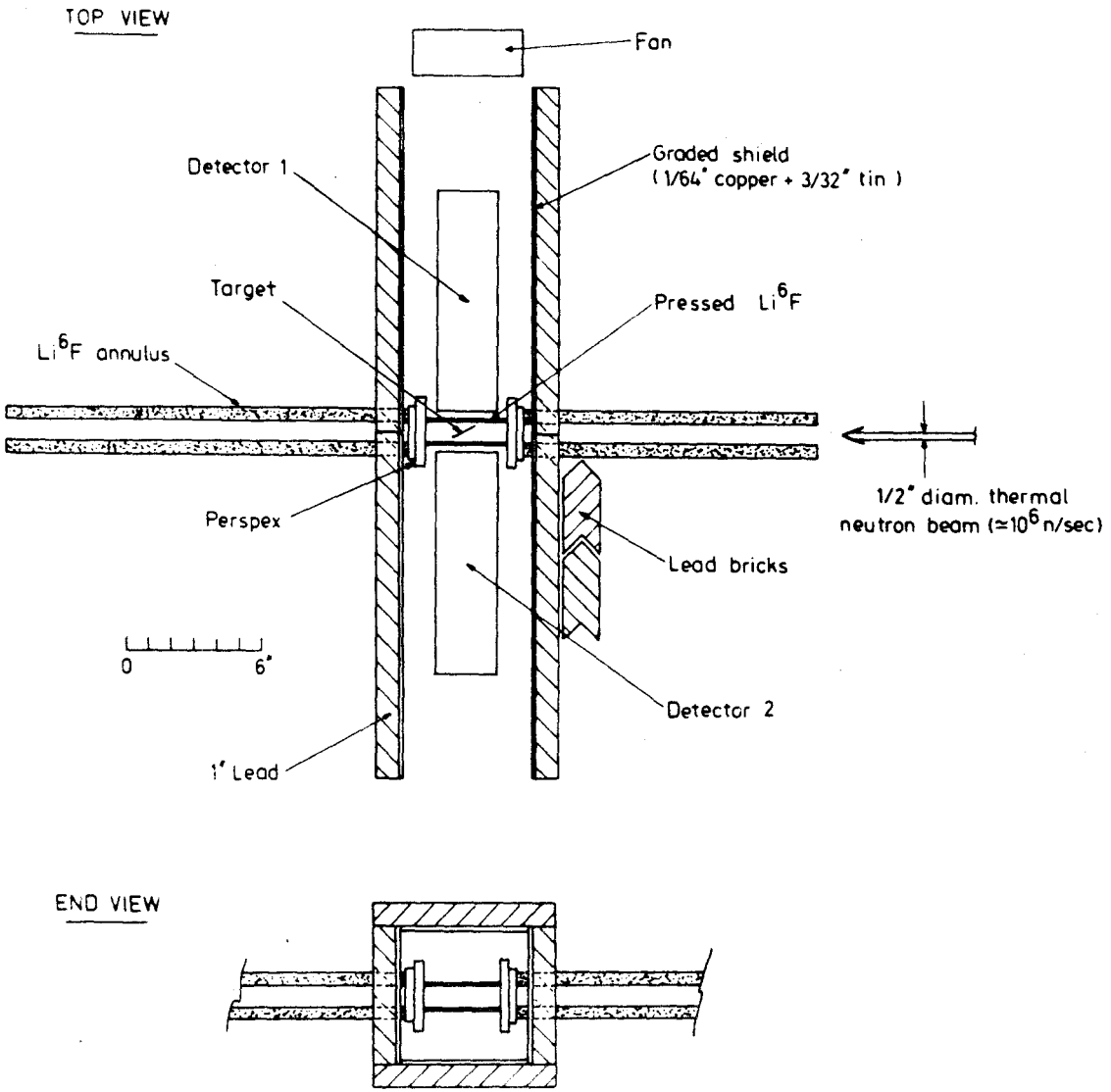

Fig. II.1 Beam port arrangement showing neutron and γ-ray shielding

either 200 mgm/cm^2 pressed ^{6}LiF slabs or ^{6}LiF powder sealed between thin sheets of polyethylene, were used to provide the neutron shielding between the target and detectors. A small electric fan forced air through the lead channel which enclosed the detectors in order to remove the heat generated by the photomultiplier tube bases. The lead surrounding the detectors was covered with 3/32" tin and 1/64" copper to absorb the lead X-ray. A concrete beam catcher placed six feet from the end of the ^{6}LiF annulus stopped the unused portion of the neutron beam.

2. Neutron Reactions in the NaI Detector

Despite the neutron shielding precautions that were taken, several reactions were observed that can be ascribed to the interaction of both fast and thermal neutrons in the NaI detector. A level in ^{127}I at 58 keV excited by inelastic scattering of fast neutrons, and 2 levels in ^{128}I at 30 keV and 137 keV excited by thermal capture, in addition to the 28 keV iodine K X-ray, were the most serious consequences of the neutron leaks. All of these have relatively long lifetimes: $T_{1/2}$(58 keV) = 1.8 ns (GE66), $T_{1/2}$(30keV) = 8.8 ns, and $T_{1/2}$(137 keV) = 8.8 ns (TO61) and hence could seriously influence a lifetime measurement on a target nucleus if the delayed γ-ray of interest is close in energy to any of the detector reactions. However in all experiments, except for

the lifetime measurement of the 77 keV level in ^{32}P, the influence of these NaI reactions was found to be negligible. The effect was investigated by obtaining singles spectra with and without a target in the beam, with a carbon neutron scatterer in place of the target, and by placing lead shielding between the target and detector in order to attenuate the target γ-rays while passing the scattered neutrons. Such measurements were made during the initial setting up of each experiment in order to determine that the detector reactions had been reduced to an acceptable level.

B. Photomultipler Base

Generally an external resistor divider chain is used to maintain each of the PM dynodes at the desired potential. Since the multiplication factor achieved at each dynode depends on the difference in potential between that and the preceeding dynode, to achieve gain stability it is important to keep the inter-dynode potential constant. For a low PM duty cycle, i.e. for low counting rates, capacitors are generally placed across the dynodes to maintain a constant potential over the short duration of the detector pulse. However if the mean current down the later stages of the PM tube becomes significant compared to the current down the resistor chain, then the voltage distribution applied to the PM tube will be changed,

and a counting rate dependent gain shift will occur.

Because NaI has approximately 3 times the light output and 100 times the decay time of a plastic detector, a NaI detector is more succeptible to a gain shift at high counting rates. Using a commercial "Ortec" base at 2500 V, (2ma), large gain shifts were observed with a NaI detector at rates above 10 khz. To reduce this effect, 2 high current bases, passing 10 ma at 2500 V were constructed for use with NaI detectors.

The type II voltage distribution (RC) was operated from a positive high voltage supply in order to allow the photocathode to be at ground potential. While a negative HV supply allows the anode signal to be direct coupled into the timing circuit, the photocathode is at the full power supply voltage and therefore careful electrical shielding must be used in the vicinity of the photocathode in order to prevent leakage current through the PM window. This leakage could greatly increase the rate of emission of single electron noise pulses from the photocathode, and since the optimum timing for NaI is usually obtained for a triggering level below one photoelectron, the timing resolution could be seriously degraded.

To dissipate the 25 watts (at 2500 V) of heat generated in the base, the 3 watt resistors used for the divider chain were enclosed in an open cage which

allowed air from a small electric fan to circulate. The HV supply was connected to the anode and to the divider chain through a 50 Ω resistor and the anode signals were taken out into a 50 Ω coaxial cable from across the resistor. The shield and signal leads of the cable were connected through 0.005 μf 3kV capacitors to the HV and anode sides respectively, of the 50 Ω resistor. The effective capacity, c = 0.0025 μf and the R = 25 Ω, from the parellel combination of the 50 Ω resistor and the 50 Ω cable, differentiated the anode signal with a 62.5 ns RC time constant.

C. Electronics

1. Delayed Coincidence System

A "fast-slow" delayed coincidence system processes the detector signals in 2 separate channels. In the "fast" channel the timing information is extracted from the start and stop detectors and the start-stop time interval is converted to a pulse height proportional to the length of the time interval. In the "slow" channel the energy selection is performed and the start-stop time interval obtained from the fast channel is accepted only if the energy conditions imposed on the start and stop events are satisfied.

A block diagram of a typical experimental system using a plastic start detector and a NaI stop detector

is shown in Fig. II.2. The timing information was obtained from the anode current pulse of the 8575 (or 8550) photomultiplier tubes using leading edge discriminators. In the NaI side, the anode signals were first amplified by a factor of 100 in order to allow the commercial fast discriminator to trigger at the 1 photoelectron level, (approximately 2 mv for an 8575 at 2500 V). The NaI discriminator output was delayed by an appropriate amount and was fed, along with the plastic discriminator output, to the start-stop type time-to-amplitude converter (TAC) which produced a bipolar pulse with an amplitude proportional to the start-stop time interval. A small quantity of charge from the 9th dynode was capacitively coupled to a preamplifier and double delay line amplifier (DDL) in order to provide energy proportional bipolar pulses. These signals were then passed to single channel analysers (SCA) where the energy selection was performed. Each SCA produced a logic pulse output in time with the zero crossing of the input if the input signal, and hence the energy of the event, was within the desired "window" defined by adjustable lower and upper levels. Ideally, the start SCA output would have a width equal to the TAC timescale while the stop SCA output would be a narrow pulse delayed by an amount equal to the delay in the fast stop channel. Coincidences between these 2 SCA pulses, indicating that the 2 energy conditions had been satisfied,

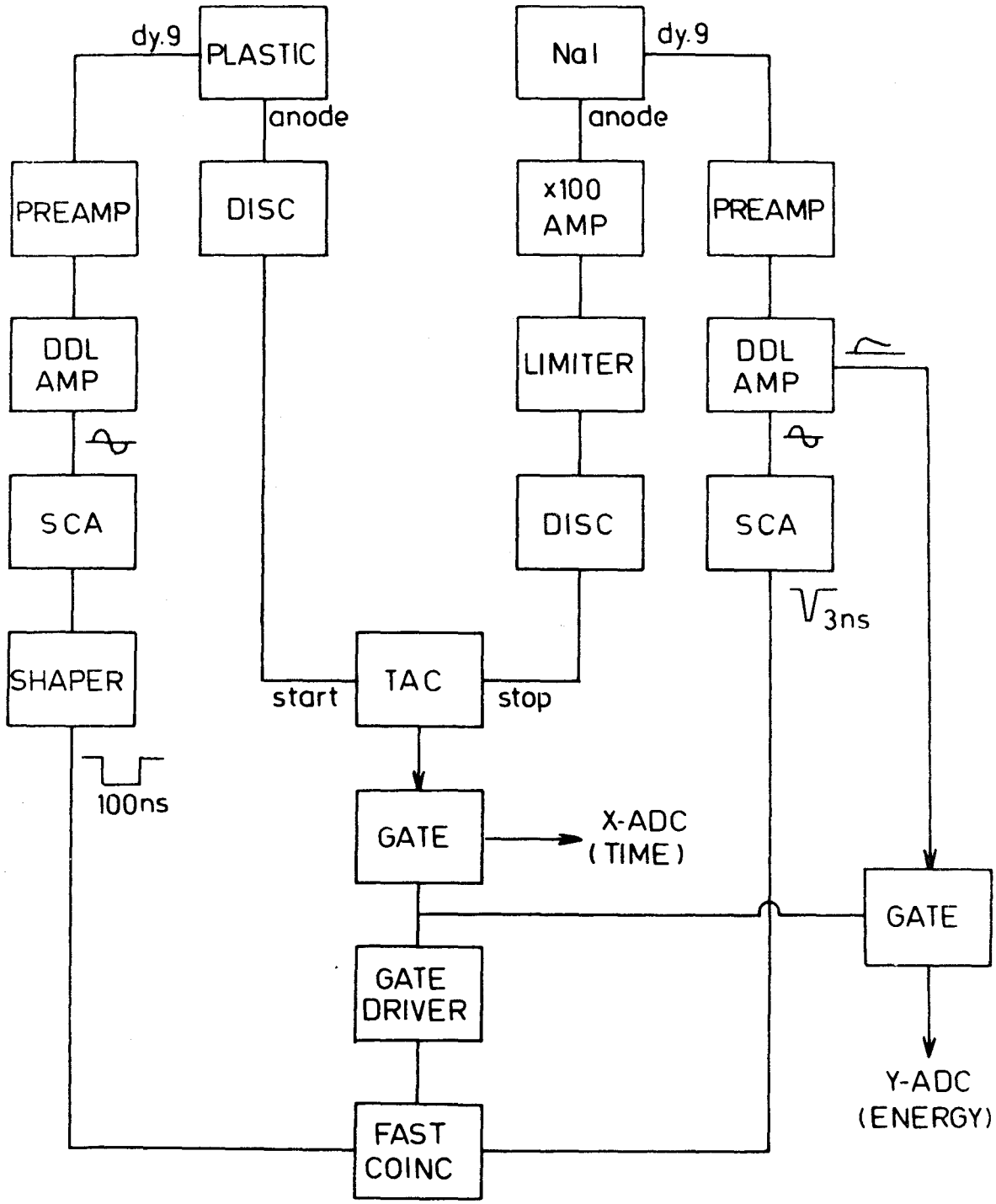

Fig. II.2 Block diagram of the 2 parameter delayed coincidence system

then generated a gating signal which allowed storage of the TAC output. While the above SCA outputs are the optimum values, since gating signals are produced only for on-scale TAC events, both the width and delay of the stop SCA output were generally increased by 50% in order to allow less critical adjustment in setting up the experiment.

In the basic form of the delayed coincidence system, the start and stop SCA's are set to select energy ranges corresponding to the population and de-population of the delayed level. An appropriate TAC timescale is chosen and the gated TAC pulses are stored in a single parameter array. In addition to this conventional single parameter data acquisition, a second procedure was used in which the energy of the stop event was stored along with the TAC output in a 2 parameter array. For this case a second output of the stop DDL and the TAC output, were both gated and stored as shown in the block diagram Fig. II.2. In order to permit storage over the full range of stop energies, the stop SCA upper level was set just below the saturation point of the DDL and the lower level just above the photomultiplier noise.

2. Anode Current Selection

While the photomultiplier output integrated over many halflives of the scintillator decay constant gives the optimum energy resolution, there are advantages in

using the peak of the anode current pulse to perform the energy selection. Since the anode current pulse closely follows the exponential decay of the scintillator (τ = 2ns for plastic, τ = 250 ns for NaI), pileup at high counting rates is greatly reduced compared to the integrated signal. A second advantage in the use of the current pulse for energy selection is that the timing signal can be gated directly by the energy condition so that the start and stop rates applied to the TAC are reduced. The lower start rate gives a lower TAC dead time while the reduced stop rate decreases the slope of the chance background (chapter IV). Thirdly, if anode energy selection can be used on both the start and stop sides, then the slow energy channel can be eliminated entirely resulting in a considerable simplification of the circuit.

Because of the short decay time of plastic detectors, provided that saturation does not occur in the photomultiplier, generally a negligible loss in energy resolution is introduced by using the anode current pulse rather than the integrated signal. For NaI detectors at low energy, the loss in resolution can be significant, however, and the size of this effect was experimentally investigated. The integrated 9th dynode energy spectrum, gated by a window set on the anode current pulses, was obtained in order to display the window contour. Above 100 keV ($\sim$ 1000 photoelectrons) the slopes of the window

were relatively sharp indicating a negligible loss in energy resolution. Below this energy the slopes of the window deteriorated rapidly, the window shape becoming approximately Gaussian for a 20% window at 30 keV.

A typical arrangement for performing anode energy selection on a plastic detector using commercial modules, is shown in Fig. II.3. The start anode signal from the plastic detector was fanned out to a timing discriminator and to a differential discriminator which produced a 200 ns wide pulse if the anode signal was within the selected window. Coincidences between the timing discriminator (delayed by 50 ns), and the differential discriminator were used to start the TAC. The signal from the timing discriminator was sufficiently delayed that the timing information was always obtained from this pulse, while the TAC start was inhibited unless the energy condition imposed by the differential discriminator was satisfied. Coincidences between a second output from the differential discriminator and the stop discriminator were used to generate a gating signal which initiated storage of the TAC output and the stop energy in a 2 parameter array.

3. Circuit for Anode Timing and Energy Selection

a) Introduction

Recent improvements in the switching speed of integrated circuit comparators make these devices suitable

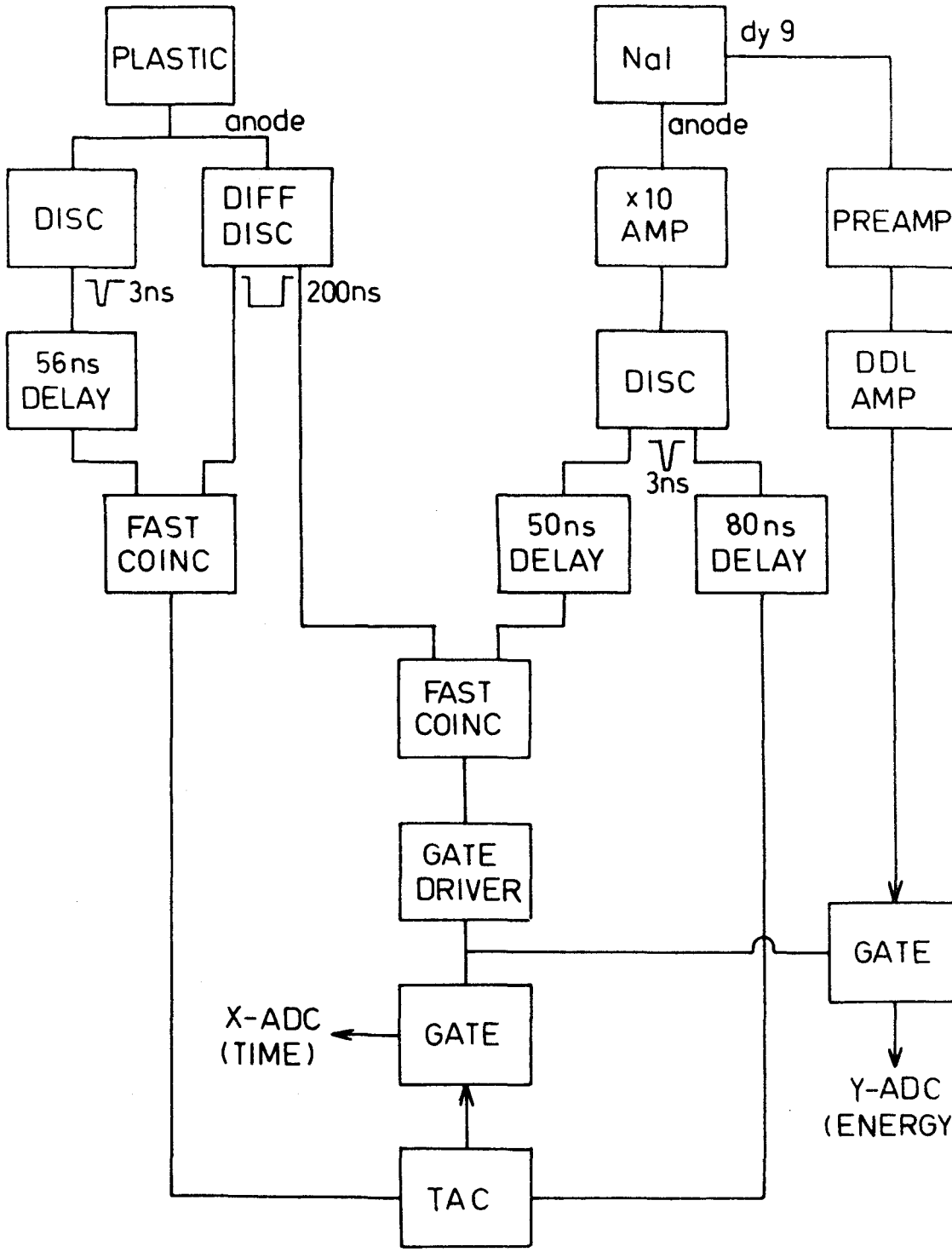

Fig. II.3 Block diagram of a delayed coincidence system for performing anode current selection using commercial electronic modules.

as triggering elements to extract timing information from photomultiplier anode pulses (HE70). To take advantage of the benefits of anode energy selection, and the simplicity and ease of construction offered by the use of integrated circuits, a circuit which obtains a leading edge timing signal and sets an energy window on the anode current pulse was constructed. Three potentiometers allow adjustment of the timing discriminator and of the upper and lower window levels. For an 8575 photomultiplier tube operated at 2600 V, a triggering level below 1 photoelectron can be obtained. The circuit was in operation continuously for several months and during this time showed no significant drift in the window position or in the timing discriminator level. The NaI time resolution which was obtained using this circuit:

FWHM (32 keV) = 2.9 ns

FWHM (511 keV) = 780 ps

FWHM (1330 keV) = 620 ps

is only slightly inferior to the optimum values obtained with a commercial fast-slow delayed coincidence system.

b) Circuit Details

The input anode pulse was fanned out to 3 μA-710 comparators which set the timing and window levels. The pulse from the timing comparator was delayed by 40 ns

and shaped to a 20 ns width. Two other shapers were triggered by the window comparators to produce 200 ns wide pulses. A triple coincidence between the timing and lower level shaper outputs, and the compliment of the upper level shaper output provided the energy selected timing signal. While these delay and pulse widths allow a large variation in the anode pulse risetime, at high counting rates, pileup effects could be reduced by decreasing these values.

A schematic diagram of the comparator circuit is shown in Fig II.4. The triggering level of each comparator is set by applying a variable voltage to the non-inverting input which holds the comparator output in the "off" state. When the anode signal, which is applied to the inverting input, exceeds the level on the non-inverting input by approximately 2 mv, the comparator output switches to the "on" state. In the timing channel, the comparator output impedance is lowered using an emitter follower in order to allow it to drive a 40 ns delay line consisting of 200 times of #28 wire wound on a grounded 1/2" diameter copper tube. The comparator outputs were differentiated and applied to MC1013 flip-flop shapers. The Q and $\overline{Q}$ outputs of each flip flop were connected to the "set" input through a capacitor and resistor respectively. The "on" time of the flip-flop following the application of the comparator trigger pulse to the J and K inputs,

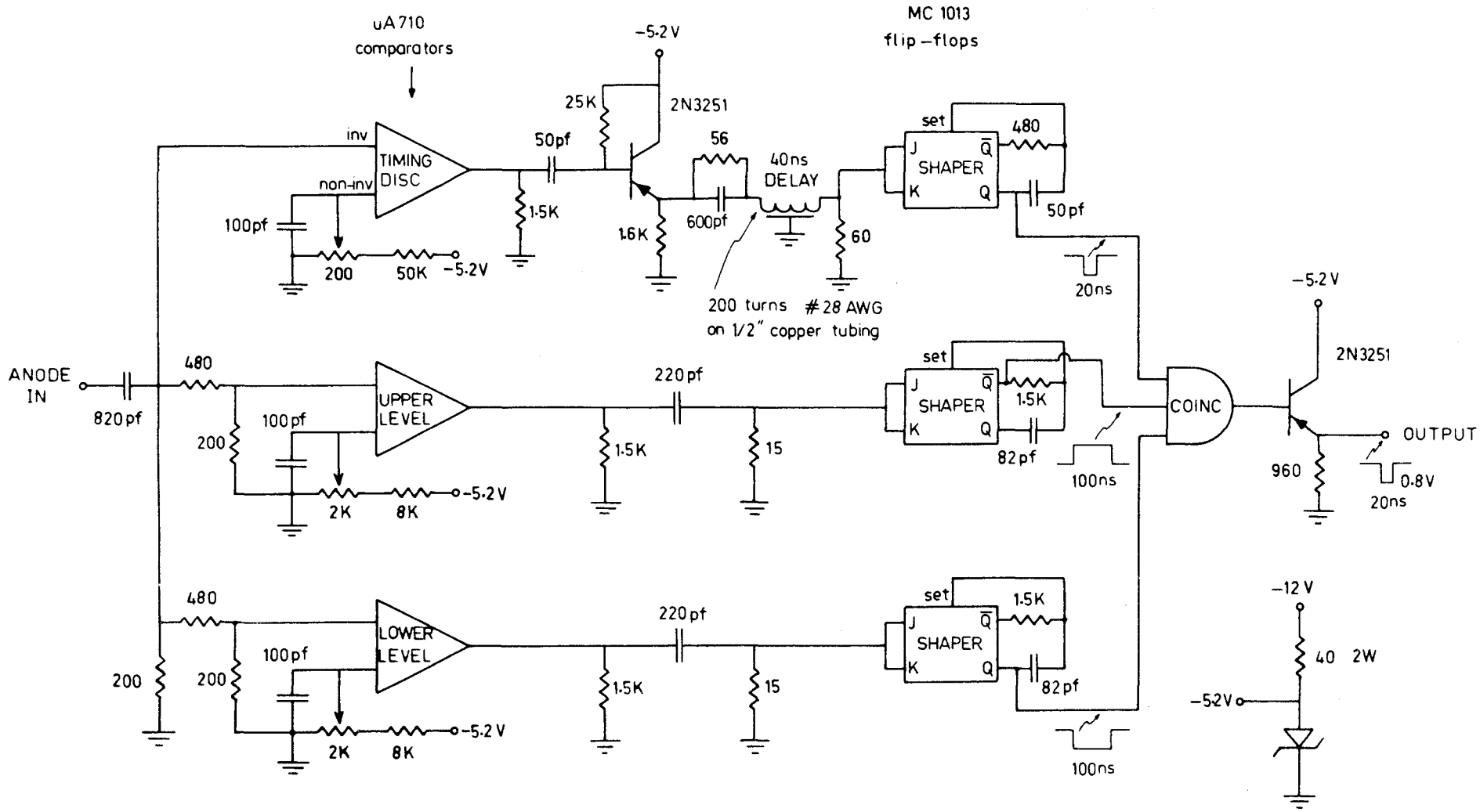

Fig. II.4 Schematic diagram of timing SCA using anode current selection

is then equal to the time required to "set" the flip-flop which is determined by the RC time constant. The output of the MC1023 triple coincidence circuit was shifted to the standard NIM logic of 0 and -0.8 volts using an emitter follower.

D. Data Aquisition and Storage

The 2 parameter data was acquired using an ND3300 multi parameter analyser system while several smaller analysers, Victoreen ST400K, ND3300, ND150F or ND120, were used for the single parameter experiments. The output was recorded on magnetic tape for the 2 parameter case while the single parameter data was typewritten out.

When the analog signals from the delayed coincidence system are applied to a multi-channel analyser, they are first quantized into a number of discrete levels in an analog -to-digital converter (ADC). Each level (or range of levels) is then assigned a storage location in the system memory, and an analog input pulse causes the corresponding digital storage location to be incremented by one count. In the 2 parameter experiment, the memory is divided into a 2 dimensional surface in which the delayed coincidence event, as defined by the outputs of both the energy and time ADC's, is stored.

The core memory of the ND3300 consisted of 16K (18 bit) channels, and this was divided up so as to allow 64 channels for the energy of the stop event and 256 channels for the start-stop time interval. After an experiment had been completed, the data was written as a 16K dump on 7 track magnetic tape for analysis by a CDC 6400 or an IBM 7040 computer.

In order to allow a second experiment to be simultaneously run using the live core memory, the 2 parameter data was often stored directly on magnetic tape and later totalized in the core memory. In this configuration the full 12 bit address from each ADC was stored in a 9200 bit buffer core memory which was automatically dumped onto magnetic tape when full. The tape containing this address recorded data was later totalized in the 64 x 256 channel core memory array and dumped onto a second magnetic tape for the computer analysis.

E. Timescale Calibration

1. Introduction

In a delayed coincidence experiment, it is important to perform an accurate calibration of the TAC timescale so that a systematic error is not introduced into the halflife result. Obtaining the width of each time channel to better than a few percent over the region

of interest of the TAC timescale can often be tedious and time consuming. A discussion of the commonly used calibration procedures will be given in addition to a more detailed description of a calibration method which was developed here. This procedure allows calibration of a range of TAC timescales and in several minutes yields an accuracy of better than 1%.

The usual procedure for calibrating a timescale is to insert a known delay in the path of the start or stop signal and measure the displacement of the prompt time spectrum. Commercial trombone air core delay lines or the helical air core delay line described by Graham et al (GR62) which use the speed of light as the standard, are useful for the calibration of short timescales while longer delays can be obtained using calibrated lengths of coaxial cable. Schwarzschild (SC63) has observed a 4% variance in the signal velocity through cables of the same type but from different batches. Hence in using cable as the delay element, the delay through each length must be first calibrated against some standard. It has been pointed out that the calibration of lengths of cable using standing wave r.f. procedures can lead to errors (BR65b, MR65, BA68, TA68). Since the signal velocity can depend on its frequency (dispersion), the cable delay must be measured over a range of frequencies corresponding to those frequency components present in the logic pulse

which is used to calibrate the TAC. A much simpler method to obtain the delay of the calibrating pulse through the cable has been proposed by Taylor (TA69). The output of a discriminator is fed back through a length of cable to its input and a single pulse allowed to circulate through the loop. The frequency of the oscillation is scaled in order to determine its period. An additional length of cable is then added to the first and the oscillation period redetermined. The difference between the 2 oscillation periods, which can easily be measured to a high accuracy, is then equal to the delay through the second length of cable. The oscillation can be viewed on an oscilloscope to ensure that only a single pulse is circulating through the system.

2. A Time-to-Amplitude Converter Calibration Module

Several procedures for calibrating a time-to-amplitude converter (TAC) using the period of a crystal controlled oscillator as the standard have been described (TH62, EG64, CH67, BA68, BO69). The method consists of correlating the start and stop pulses with a high frequency r.f. signal so that the start-stop time interval is restricted to a random multiple of the r.f. oscillator period. The resulting peaks which are generated across the TAC timescale are

separated by one oscillator period and hence yield the timescale calibration. If enough peaks are displayed across the timescale, an estimation and correction for the integral nonlinearity of the system can be obtained. A numerical analysis of this multiple peak method in connection with a differential linearity measurement in which an essentially flat time distribution is obtained from random start-stop intervals has been given by Baker et al (BA68).

To extend this r.f. oscillator method to cover the shortest timescales on commercial TAC's (50 ns) a self-contained calibration device using Motorola MDTL and high speed MECL II integrated circuits (IC's) and a 100 MHz crystal oscillator has been constructed in a single width NIM module (BO70a). The 100 MHz is scaled down and a switch mounted on the front panel allows selection of a 10, 20, 40 or 80 ns calibration peak spacing so that a range of timescales can be conveniently calibrated.

A block diagram of the arrangement is given in Fig. II.5. Two multivibrators running at frequencies slightly different from 40 KHz and 200 KHz, and hence which have a random relative phase, are shaped to pulses with 2 ns rise and fall times and a 6 ns FWHM. A 100 MHz sine wave oscillator triggers three J-K flip-flops which each scale down the frequency by a factor

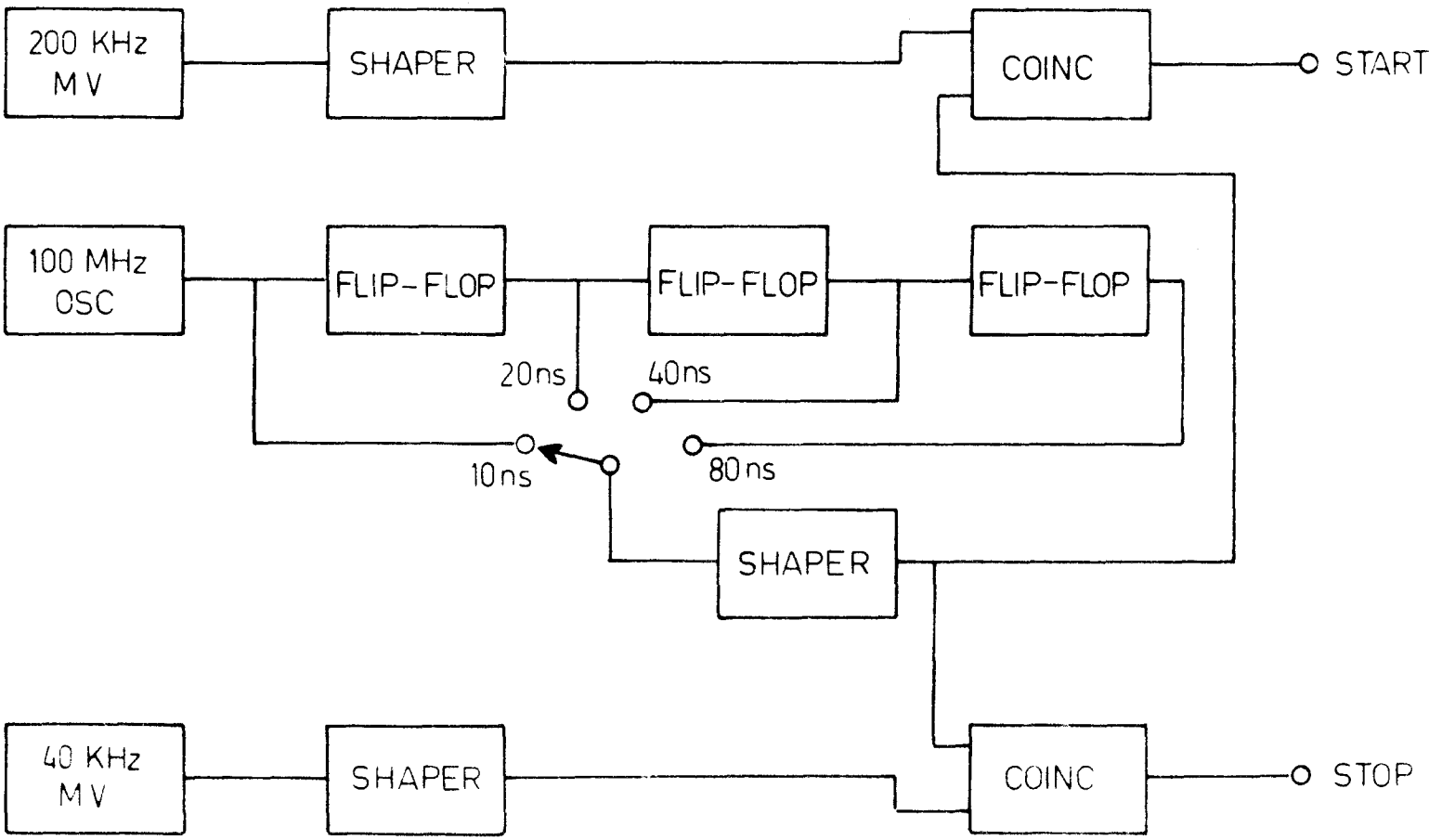

Fig. II.5 Block diagram of TAC calibrator

of two. The desired frequency is selected and then shaped to a 4 ns FWHM clock pulse. The 200 KHz and 40 KHz pulses are clocked by the 100 MHz pulses and used to respectively start and stop the TAC.

Fig. II.6 gives a schematic diagram of the TAC calibrator. The ± 5V required for the IC's were obtained from the ± 12 volt NIM bin power supply using zener diodes. The operation of the individual elements, (multivibrator, shaper and 100 MHz oscillator) has been described in detail in Motorola IC Application Notes (MO). Two MC832 dual four input buffers were fed back so as to act as free running multivibrators and these were each coupled to a shaper using an MC1023 dual four input clock driver which generated fast pulses with a FWHM equal to the cable delay of 6 ns. Originally an MC1023 was used along with a 100 MHz 5th overtone quartz crystal in an oscillator circuit to provide the 100 MHz signal. This however required critical adjustment of the tank circuit, so in order to ensure long term stability it was replaced with a commercial encapsulated 100 MHz osc module*. The output of the oscillator was capacitively coupled through an emitter follower to an MC1017 JK flip-flop

*Type BMO-5u; Bliley Electric Company, 2545 West Grandview Boulevard, Erie, Pa.

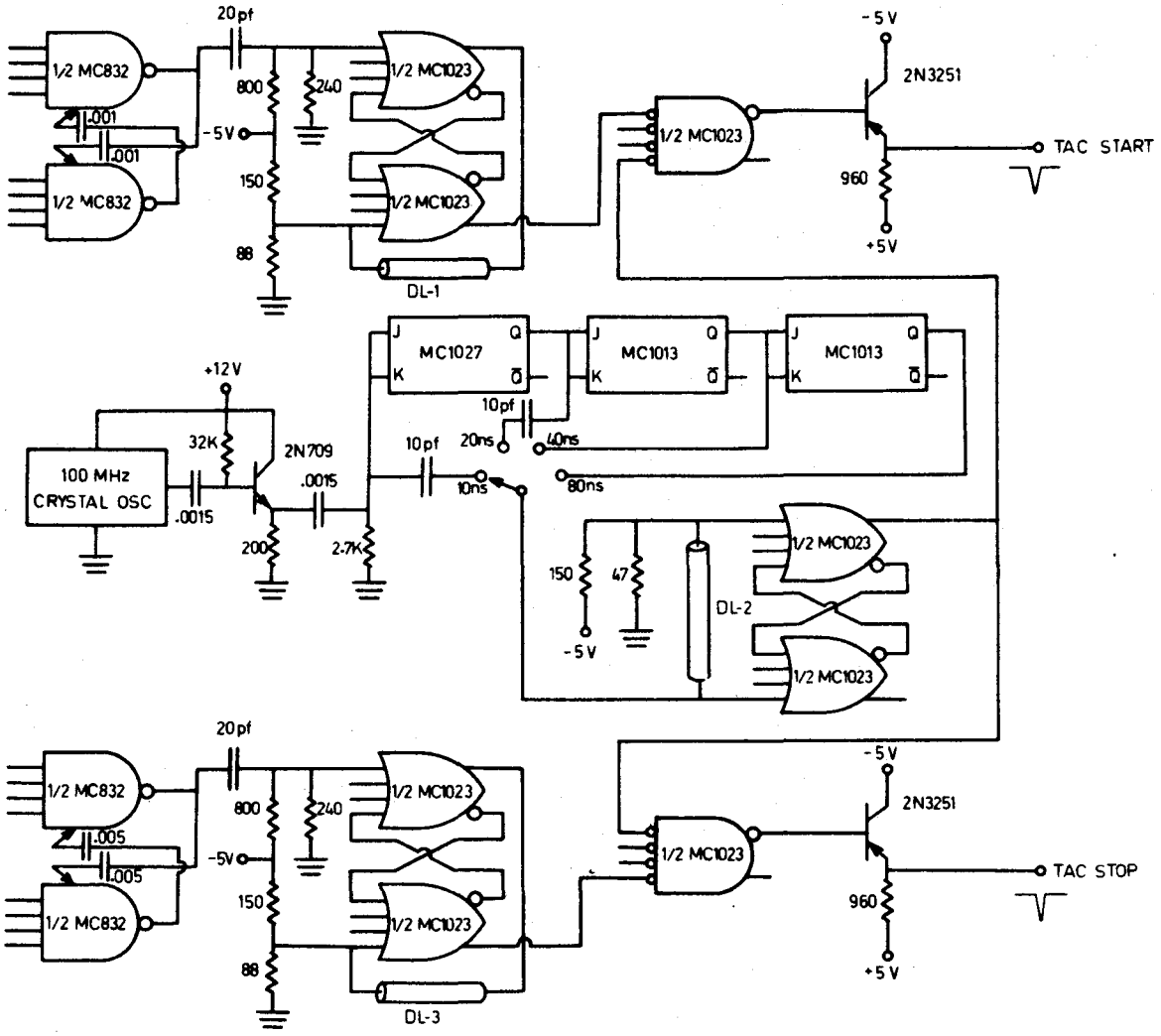

Fig. II.6 Schematic diagram of TAC calibrator. The resistances are in ohms and the capacitances in μf unless otherwise marked. Delay lines DL-1, DL-2 and DL-3 are each 4 feet of RG174μ cable. All unused MC1023 inputs are connected to -5V.

(f_{max} = 120 MHz) and then to two MC1013 JK flip-flops (f_{max} = 70 MHz) for frequency division. A rotary switch selected the desired clock frequency and an MC1023 shaper generated the 4 ns FWHM clock pulses. (For this shaper the width equals the cable delay of 6 ns minus the 2 ns propogation delay of the clock driver.) An MC1023 using complimentary input and output logic was used to clock the multivibrator pulses and capacitively coupled emitter followers were used to provide a low output impedance and to level shift the MECL logic of -0.8 V and -1.6 V to the standard NIM fast logic of 0 V and -0.8 V.

In general component layout was not critical provided that reasonable high frequency practices were followed. Despite a relatively long length of single strand 30 AWG wire carrying 100 MHz to the selector switch (approximately 8 cm each way), after standardization in the shaper, no significant multiple pulsing, radiation effects, or deterioration in pulse shape was observed.

While a narrower calibration peak width reduces the statistical uncertainty in determining its position, if the peak falls entirely in one channel, then, assuming ideal square channel profiles, the uncertainty will equal that channel width. For a sufficiently large number of counts, the accuracy can then be improved by broadening the peak so that it occupies at least two channels. A useful feature of the timescale calibration method presented here is that it allows the calibration peak widths to be

changed to suit a range of timescales and channel resolutions.

There is a distribution in the widths of the clocked output pulses which results from the degree of overlap between the clock and multivibrator pulses. The widest clocked pulses correspond to the best correlation with the clock and hence these will contribute to the centre of the calibration peaks while the narrower clocked pulses will contribute to the wings of the peaks. Thus by integrating the clocked output and setting a threshold on accepted pulses, the width of the calibration peaks can be varied.

The clocked outputs of the TAC calibrator were integrated on stray system capacity and attenuated by variable parallel resistances so as to allow selection of the pulses which exceeded the 200 mV triggering levels of the TAC.

Fig. II.7 shows calibration peaks separated by 10 ns displayed on a 100 ns TAC timescale using 15 ohm parallel resistances. These resistances attenuated the clocked signals by a factor of three so that only the upper 30% of the clocked pulses triggered the TAC. The resistances were then removed in order to broaden the peaks and Fig. II.8 gives the calibration of a 1 μs timescale using the broadened peaks with a separation of 80 ns.

The above method generates peaks whose position

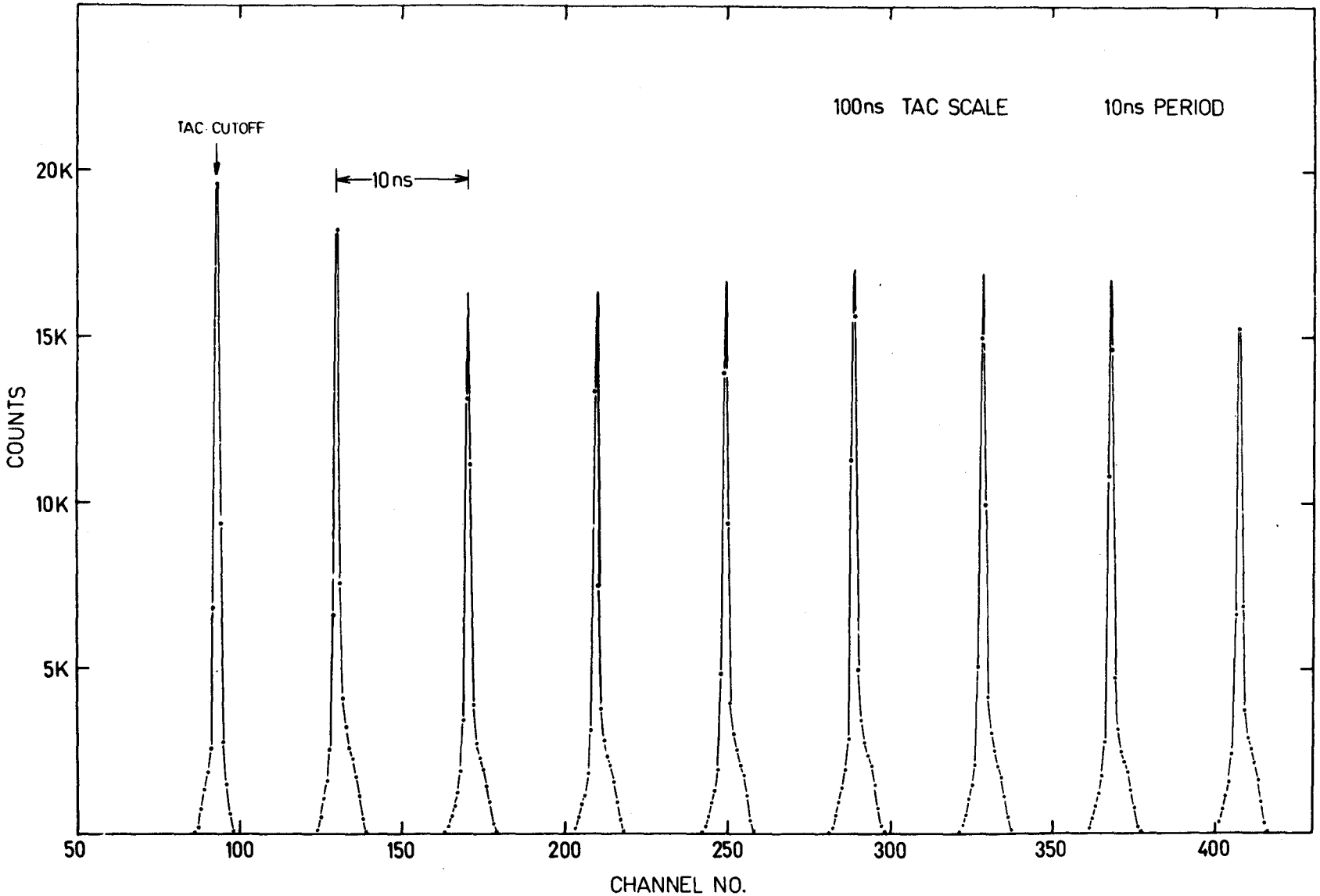

Fig. II.7 A typical calibration run using peaks separated by 10ns to calibrate a 100ns TAC timescale. The upper and lower portions of the 512 channel spectrum are not shown. The first peak is distorted because of the nonlinearity in the region of the TAC cutoff.

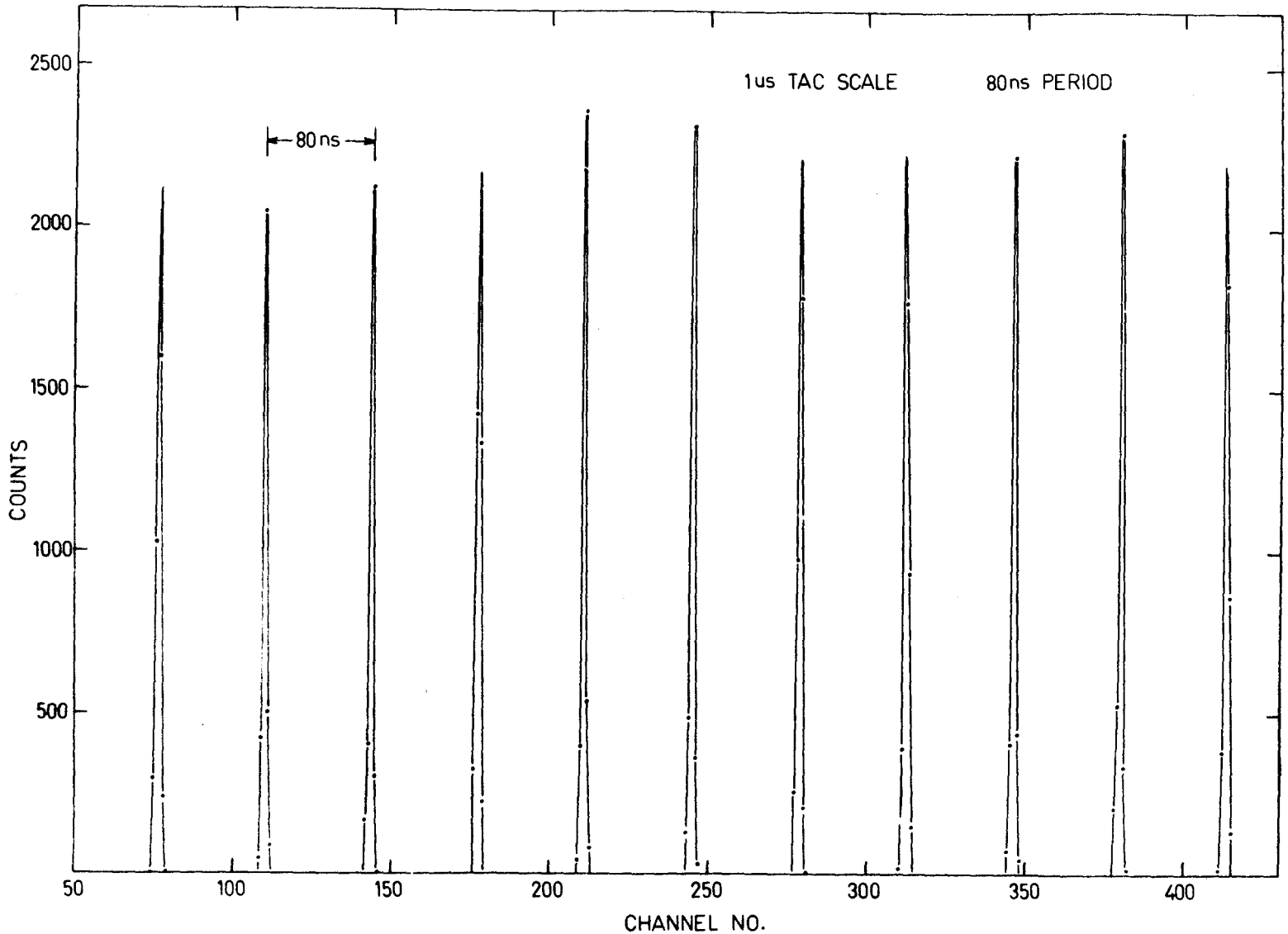

Fig. II.8 A typical calibration run using broadened peaks separated by 80ns to calibrate a 1 μs TAC timescale.

can be easily determined to better than 10 ps and hence is entirely adequate for the calibration of TAC's. For cases where higher precision is desired, narrower calibration peaks can be produced by clocking the multivibrator pulses using a high speed flip-flop instead of the MC1023 clock driver. In this arrangement the multivibrator pulses are applied to the SET input and the clock pulses to the RESET input of the flip-flop. By differentiating the flip-flop output with a time constant which is much shorter than the minimum flip-flop width, the pulse corresponding to the clocked SET-RESET transition can then be selected by its polarity, standardized, and used as the timing signal. The resulting calibration peaks can be broadened to a Gaussian shape by mixing a random noise spectrum with the output of the TAC (HE68).

CHAPTER III

TIME RESOLUTION

A. Theoretical NaI Time Resolution

1. Introduction

The total FWHM resolution, W, of a delayed coincidence system is obtained by adding the resolutions of the start and stop channels in quadrature:

$$W^2 = W_{start}^2 + W_{stop}^2$$

For a fixed start resolution, W_{stop} can be further expressed in terms of contributions from the scintillator - photomultiplier system, W_{SPM}, and from light collection in the scintillator, W_{LC}:

$$W^2 = W_{start}^2 + W_{SPM}^2 + W_{LC}^2 \qquad \text{III.1}$$

In the following sections, expressions for W_{PMS} and W_{LC} are obtained for a cylindrical NaI detector and these are compared with experimental results.

2. Scintillator - Photomultipler Resolution

A large number of theoretical calculations have

been made in an attempt to explain the time resolution properties of the scintillator - photomultiplier system. Several survey articles have been written on this subject (SC63, BI64, GA66, OG66), and more recent references can be found in (LY66, SI67, DO70, WA70). Measurements of the parameters describing the time response of some of the high speed photomultiplier tubes have been made (MI60 , KR65, BR65a, BE66a, BE66b, KE67, PR70), while the time resolution properties of a number of the commonly used scintillators are given in (BI64, MC65, YA66, BE69).

Typical of the theoretical expressions which have been used to describe the time resolution introduced by the scintillator emission statistics and the photomultiplier time dispersion, is that given by El Wahab and El Salam (WA70). Taking the limits

$$\tau_1 << \tau_2$$
$$\nu << R$$

where τ_1 represents the exponential risetime of the photomultiplier , τ_2 = scintillator decay time, ν = triggering level in photoelectrons and R=pE=average number of photoelectrons released from the photocathode at an energy E; which is generally satisfied for NaI mounted on a fast photomultiplier tube, this expression can be reduced to:

$$W_{SPM} = \frac{2.354\tau_2}{2\sqrt{R}} \left[\left(\frac{\nu}{R}\right)^{1/2} + \left(\frac{2\tau_1}{\tau_2} + \frac{\nu}{R}\right)^{1/2} \right] \qquad \text{III.2}$$

Further simplifications can be made in the limits of high and low energy. For NaI, (τ_2 = 220 ns and p = 10 photoelectrons per keV) at a triggering level of 1 photoelectron, and using the value τ_1 = 330 ps, (BR65a), the high energy limit:

$$2\,\frac{\tau_1}{\tau_2} \;>>\; \frac{\nu}{R} = \frac{\nu}{pE}$$

corresponds to an energy:

$$E >> \frac{\nu\tau_2}{2p\tau_1} = 40 \text{ keV}$$

and equation III.2 reduces to

$$W_{SPM} = \frac{2.354}{\sqrt{2}} \left[\frac{\tau_1\tau_2}{R}\right]^{1/2} \quad \text{for } E >> 40 \text{ keV} \qquad \text{III.3}$$

For the low energy limit:

$$2\,\frac{\tau_1}{\tau_2} << \frac{\nu}{R}$$

Equation III.2 becomes

$$W_{SPM} = \frac{2.354}{\sqrt{2}} \quad \frac{\tau_2}{R} \quad \text{for } E << 40 \text{ keV} \qquad \text{III.4}$$

Thus at very low energy, the time resolution

scales as 1/E and is dominated by scintillator statistics in agreement with the photomultiplier independent results of Post and Schiff (PO50), while at high energy where the speed of the photomultiplier becomes significant, the energy dependence changes to $1/\sqrt{E}$.

3. Light Collection Resolution

Reflections of light photons inside the scintillator before they escape to the photocathode will cause a distributed time delay which contributes to the time resolution. Sigfridsson (SI67) has shown that the distribution of time delays introduced by light collection can be approximated by an exponential with a mean life determined by the dimensions of the scintillator, and an expression for the resolution introduced by the light collection was given as

$$W_{LC} = \left[\frac{\pi \tau 2 \Delta T}{pE} \right]^{1/2}$$

where ΔT is the mean photon delay due to reflections. Setting $\Delta T = m\Delta t$, where m is the mean number of reflections and Δt is the mean delay per reflection, and assuming that the scintillator is a cylinder of radius r and height h, gives:

$$m = \frac{\text{total scintillator surface area}}{\text{scintillator window area}} = \frac{2r + 2h}{r}$$

$$\Delta t = \frac{h}{v} \qquad (v = \text{light velocity in scintillator})$$

and hence the light collection resolution is equal to:

$$W_{LC} = \left[\frac{2\pi \tau_2}{pE} \frac{h(r+h)}{rv} \right]^{1/2}$$

4. Optimum Triggering Level

An expression for the optimum triggering level was also given by El Wahab and El Salem:

$$\frac{\nu}{R} = 1 - \frac{\tau_2^2}{(\tau_2-\tau_1)(\tau_2+\tau_1)} e^{-\nu/R} + \frac{\tau_1}{2(\tau_2-\tau_1)} e^{-\frac{\nu}{R}\frac{\tau_2}{\tau_1}}$$

For $\tau_2 >> \tau_1$ and $R >> \nu$, this can be approximated by:

$$\frac{\nu}{R} = \frac{\tau_1}{4\tau_2} e^{-\frac{\nu}{R}\frac{\tau_2}{\tau_1}}$$

Solving this equation for τ_1 = 330 ps, τ_2 = 220 ns and p = 10 photoelectrons/keV, indicates that single photoelectron triggering is optimum up to 800 keV for NaI mounted on an 8575.

Experimental measurements (HO70) have shown that above 300 keV, there is a negligible increase in the width and slope of the time distribution if the triggering level is increased from 1 to 3 photoelectrons.

Thus above 300 keV a higher triggering level can be used to reduce spurious triggering on noise events.

5. NaI Walk Curve

For one of the lifetime analysis procedures described in Chapter IV, it is necessary to know the shape of the walk curve, or centroid-energy-function (CEF), which describes the displacement of the centroid of the time distribution with energy.

The NaI CEF has been experimentally measured (BA60, CU61) for a high triggering level, ($\nu \gtrsim 10$) and was satisfactorally interpreted in terms of the photomultiplier independent results of Post and Schiff (PO50). Recently a more sensitive examination using 1 photoelectron triggering and an 8575 photomultiplier tube operating at 2100 V was made by Hohenemser (HO70) and the results were compared with a simple model which included photomultiplier effects. Reasonable agreement was obtained below 100 keV, while at higher energy the experimental time shifts were lower than the theoretical values. Based on the sensitivity of the shape of the high energy CEF to photomultiplier parameters, and the relative insensitivity to triggering level and detector size, it was suggested that the failure of the model was due to space charge effects in the later dynodes.

At high energy, the current pulse was spread out due to electrostatic repulsion more than at low energy so that the first component of the pulse would arrive earlier at high energy.

For all the halflife measurements which were made here, the range of interest of the CEF extends beyond the low energy limit, $E << 40$ keV, so that the photomultiplier independent model cannot be used. Since there is no current model which gives a good description of the CEF for $\nu = 1$ and $E \geq 40$ keV, in applying the centroid shift lifetime analysis procedure (Chapter IV), an arbitrary second or third order polynomial was fitted to the experimental CEF in order to represent its shape.

B. Experimental Results

1. Photoelectron Yield For NaI

A direct measurement of the number of photoelectrons released from the photocathode of an 8575 per keV of energy deposited in a 1/2" x 1" diameter NaI detector was made using the method of (HO68). The photocathode of the 8575 was grounded and the focus, dynode 1 and dynode 2 electrodes were connected to a low noise charge sensitive preamplifier, and through a 10^8 Ω resistor to +250 volts as shown in Fig. III.1. A 60 cps

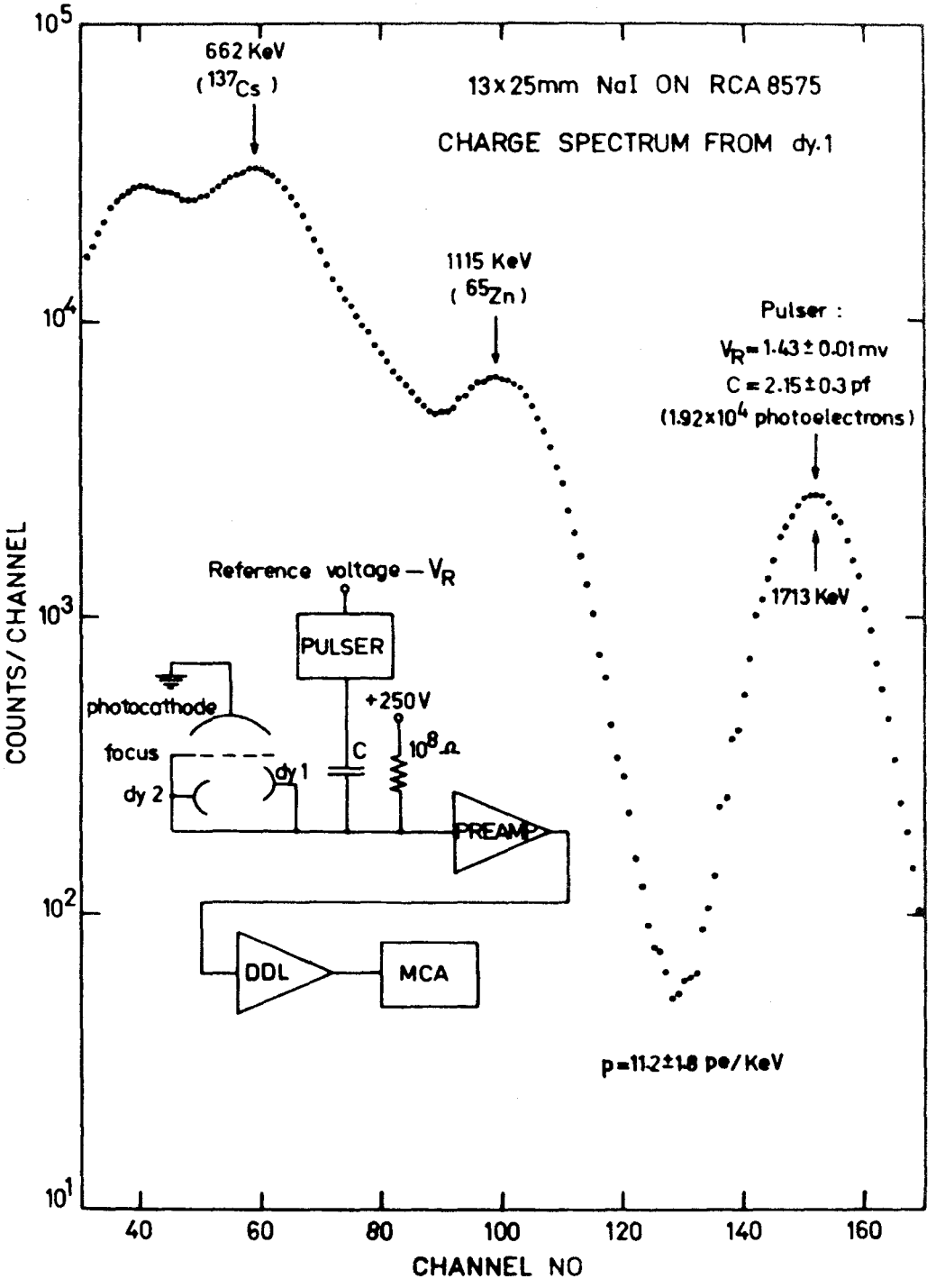

Fig. III.1 Direct measurement of the photoelectron yield for a NaI detector. The charge spectrum from dynode 1 was obtained using a mixed ^{137}Cs and ^{65}Zn source in order to calibrate the energy scale and fix the zero. A pulser which injected a known quantity of charge provided a charge calibration for the same scale and hence a value for the number of photoelectrons/keV.

pulser was connected through a capacitor, C, to the preamplifier input in order to provide the charge calibration. The pulser reference voltage, V_R, was measured to a 0.1% accuracy using a digital voltmeter and each capacitor was calibrated using a capacitance bridge.

Charge spectra were obtained using a ^{65}Zn (1115 keV) and ^{137}Cs (662 keV) mixed source for 4 different capacitors and pulser reference voltages, and a typical spectra is shown in Fig. III.1. The 2 γ-ray peaks were used to obtain the location of the zero energy channel and to calibrate the energy scale. The charge injected by the pulser = CV_R, gave the charge calibration of the same scale and hence a value for the number of photoelectrons per keV.

Reducing the high voltage bias to 150 V produced no change in the γ-ray spectra indicating essentially complete charge collection at 250 V. An estimate for the number of photoelectrons per keV, p, was obtained from each of the 4 different capacitors and pulser reference voltages:

$C = 0.65 \pm 0.33$ pf	$p = 18.2 \pm 9.1$ photoelectrons/keV
2.15 ± 0.32	11.2 ± 1.8
20.0 ± 1.0	8.51 ± 0.43
33.0 ± 1.7	10.00 ± 0.50

The uncertainty in the weighted mean value:

$$p = 9.3 \pm 0.5 \text{ photoelectrons/keV}$$

has been increased from the capacitor error to include possible systematic effects.

The photoelectron yields of 3 additional detectors were measured relative to this calibrated detector. Using a ^{137}Cs source, energy spectra were obtained from the 9^{th} dynode of the 8575 for 4 NaI detectors. Each run was obtained using the same photomultiplier and experimental conditions. The separation between the 31.2 keV X-ray peak and the 662 keV γ-ray peak, which represents the relative light output of each detector, then gave the photoelectron yield relative to the calibrated detector with an estimated error of 3%:

1/8" x 1" diameter NaI	p = 10.6 photoelectrons/keV
1/4" x 1"	10.2
1/2" x 1"	9.3 $\pm$ 0.5 (calibrated)
1" x 1"	9.3

While the photoelectron yield for NaI depends on the thallium activator concentration (BI64) and on the quantum efficiency of the photocathode, the above values are in good agreement with other measurements for commercial "Harshaw" NaI detectors mounted on 8575 photomultiplier tubes. (LY66, HO68). Using indirect measurement techniques, lower values between 1 and 5 photoelectrons/keV have been reported (CU61, BI64, BR65, HO70). These

lower values were obtained as a fitted parameter in a model which was used to describe the experimental time or energy resolution and are therefore probably less reliable than the direct charge measurements.

2. Experimental Time Resolution

For the high energy case, equations III.3 and III.5 can be used in Eq. III.1 to give an expression for the total resolution:

$$W^2 = W^2_{start} + \frac{\tau_2}{pE}\left[2.77\ \tau_1 + 6.28\ \frac{h(r+h)}{rv}\right] \qquad \text{III.6}$$

so that a plot of W^2 vs 1/pE is linear with an intercept = W^2_{start} and slope = $\tau_2[2.77\ \tau_1 + 6.28\ \frac{h(r+h)}{rv}]$. In order to check Eq. III.6 experimental resolution measurements were made at 130 keV, 260 keV, 511 keV and 1330 keV using a 1/8" x 1" NaI and a 1/4" x 1" NaI mounted on an 8550 (operating at 2500 V) in the fast-slow delayed coincidence system shown in Fig. II.2 A 1/2" x 1" Naton 136 plastic scintillator mounted on an 8575, which contributed a resolution W_{start} = 200 ps, was used as the start detector. The experimental values for W^2 were plotted vs 1/E and a straight line with a fixed intercept and an adjustable slope was fitted to the data as shown in Fig. III.2 (a) and (b). The fitted

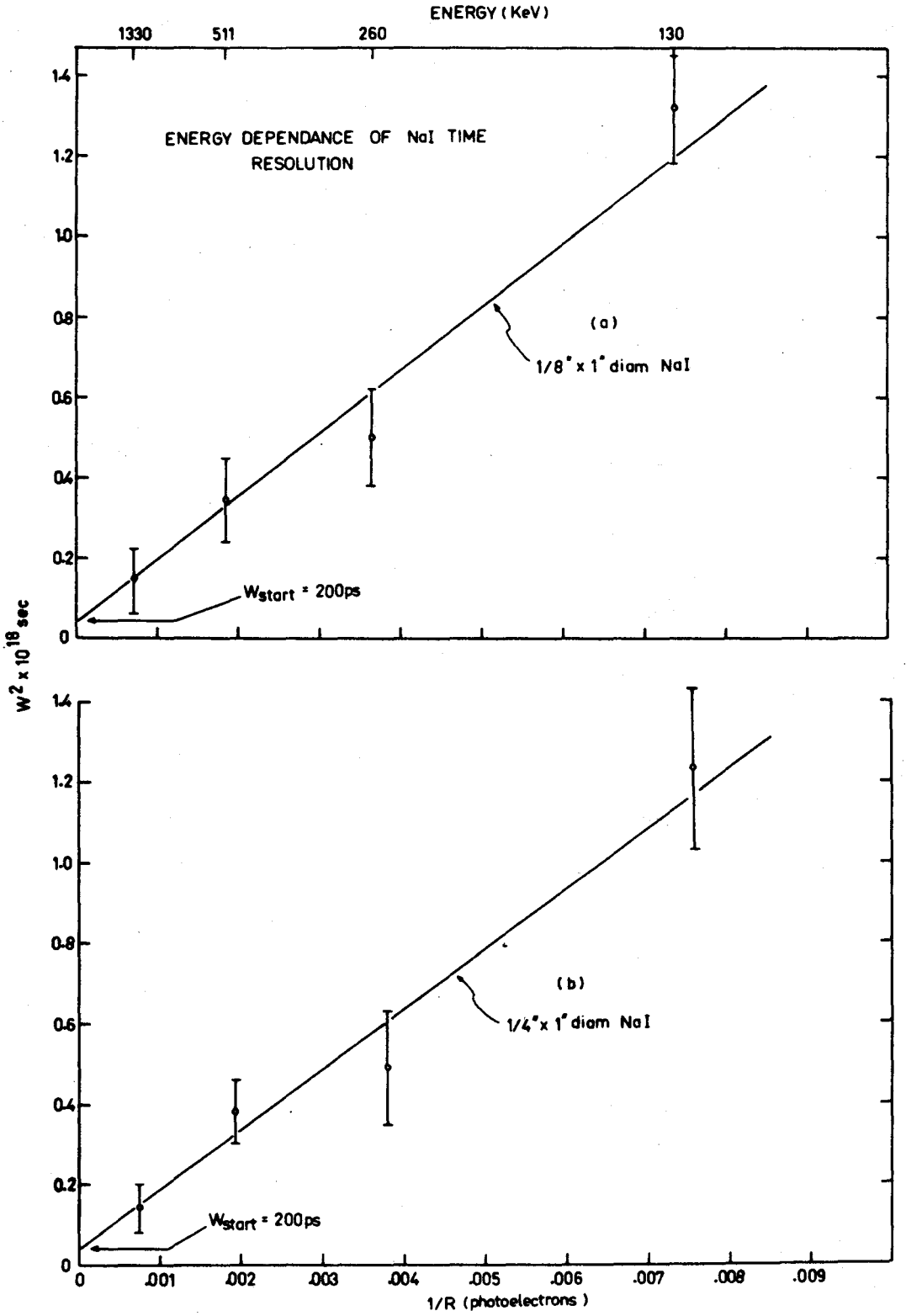

Fig. III.2 Dependence of the time resolution of 2 NaI detectors on energy.

slopes, used in Eq. III.6 along with the measured values for p and v = c/1.77 (where the index of refraction for NaI, 1.77, was taken from BI64), yielded estimates for τ_1:

1/8" x 1" NaI	τ_1 = 210 ps
1/4" x 1" NaI	τ_1 = 120 ps

A direct measurement of the exponential rise of an XP1020 PM tube, which is similar in speed to the 8575, yielded the value τ_1 = 330 ps (BR65a). Present and Scarl (PR70) have obtained a 40% shorter single photoelectron resolving time for an 8550 than for a 8575 PM tube. The τ_1 for an 8550 can then be estimated to be in the range of 200 ps and this is in reasonable agreement with the τ_1 values obtained from the above fitted parameter analysis.

Using the high energy limit, Eq. III.6 can be rearranged to give the dependence of the time resolution on scintillator size:

$$pE(W^2 - W_{start}^2) = \text{constant} + \frac{6.28\tau_2}{v} \quad \frac{h(r+h)}{r}$$

This equation predicts that a plot of $\frac{h(r+h)}{r}$ vs $pE(W^2 - W_{start}^2)$ should be linear with a slope $\frac{6.28\tau_2}{v}$, and was checked at 31.2 keV and 511 keV using various thickness 1" diameter NaI detectors.

The results for detectors of 1/8", 1/4", 1/2"

and 1" thickness, obtained using the same experimental arrangement as for the energy dependence measurements, are given in Fig. III.3. The error bars were obtained assuming a 3% error in p, a 20% error in W_{start}, and errors of 4% at 31.6 keV and 2% at 511 keV in W. Straight lines with adjustable intercepts and fixed slopes = $\frac{6.28\tau_2}{v}$ were fitted to the experimental data using the values v = c/1.77 and τ_2 = 220 ns. As can be seen from Fig. III.3, this model, which uses no fitted parameters, is able to give a reasonable description of the dependence of the NaI time resolution on scintillator size. A better fit to the 31.2 keV data would probably be obtained if Eq. III.2, rather than the high energy approximation, Eq. III.3 had been used.

The results obtained here show that even at low energy, it is important to use as small a NaI detector as possible in order to minimize the time resolution. For a given photomultiplier and detector size, Eq. III.6 can be used to estimate the contribution of the scintillator size to the total time resolution.

C. Čerenkov Time Distribution

If a γ-ray interacts in a transparent medium to produce an electron which has a velocity higher than the speed of light in that medium, then Čerenkov light photons will be produced. The number of Čerenkov photons

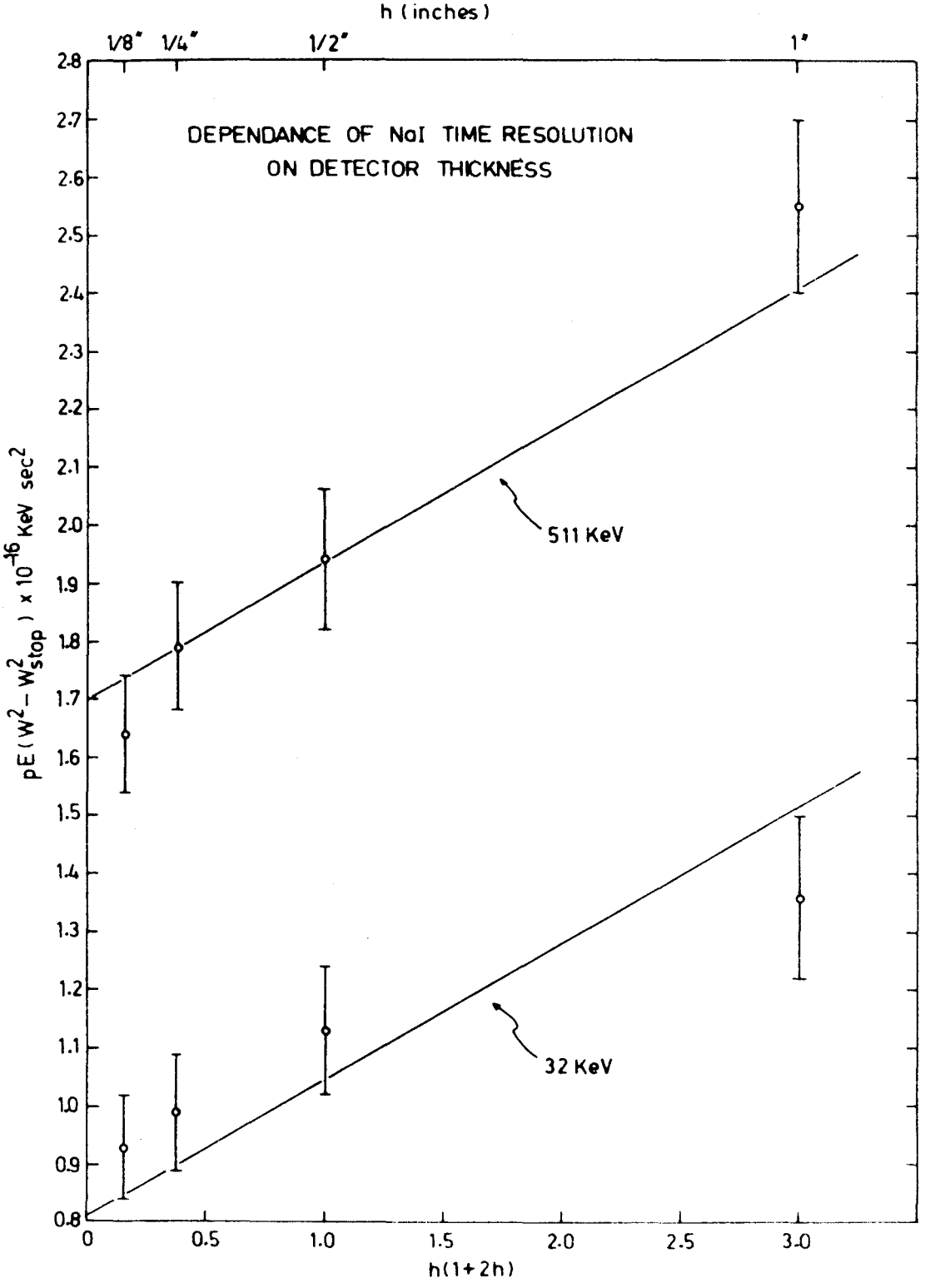

Figure III.3 Dependence of NaI time resolution on scintillator size at 31 keV and 511 keV obtained using 4 cylindrical detectors each with a 1" diameter and with heights, h, of 1/8", 1/4", 1/2" and 1".

emitted by an electron within the spectra range $\lambda_1 - \lambda_2$ is given by (JE58).

$$N = 2\pi\ \alpha\ell\ \left(\frac{1}{\lambda_2} - \frac{1}{\lambda_1}\right)\ \left(1 - \frac{1}{\beta^2 n^2}\right) \quad \text{for } \beta n > 1$$

where α is the fine structure constant = $\frac{e^2}{\hbar c} = \frac{1}{137}$

ℓ = electron path length

β = electron velocity/c

n = average refractive index of the medium

As an example, a 500 keV electron passing through 2 mm of glass (n = 1.46) will produce 29 visible (λ = 4000-6000 Å) light photons which corresponds to a mean pulse height of 9 photoelectrons for a photomultiplier with a 30% quantum efficiency such as the 8575.

For inefficient scintillation detectors exposed to γ-rays above the Čerenkov threshold, a significant fraction of the interactions can occur in the glass photomultiplier and scintillator windows (or an electron produced in the scintillator can escape into the glass), to produce Čerenkov photons. The first photoelectron time distribution will then be the sum of the distributions due to the Čerenkov and scintillator components. Since the Čerenkov photoelectrons are emitted with essentially no delay while the first scintillator photo-

electron has a mean delay $\frac{\tau_2}{R}$, for slow scintillators such as NaI(τ_2 = 220 ns) at low energy (E = 25 keV, R = 250), the 2 time distributions can be significantly displaced from one another so that the overall time resolution is degraded by the presence of the Čerenkov component. Thus in a delayed coincidence experiment where a delayed spectra is obtained by using the photoelectron interaction of low energy γ-rays and the corresponding prompt is obtained using the Compton interaction of high energy γ-rays which are above the Čerenkov threshold, the Cerenkov component must be subtracted out of the prompt spectrum in order to obtain the true response function.

While previous references have been made to the influence of a Čerenkov component in a delayed coincidence experiment (JE58, VO62, MC65, YA66, JO70a), this is perhaps the first case where its effect on a halflife measurement was investigated. Fig. V.8 shows 2 time spectra obtained with a 1 x 25 mm diameter NaI mounted on an 8550 using a 17 keV stop window. The prompt spectrum, obtained using the Compton distribution from high energy (E $\leq$ 7 MeV) γ-rays, shows the Čerenkov component resolved from the scintillator component, while the delayed run, obtained by photoelectric interaction, contains no prompt Čerenkov component.

Using a mercury neutron capture source, the time distribution of the pure Čerenkov component was measured.

The scintillator was removed from the stop photomultiplier and no energy selection, except for the 0.5 photoelectron lower limit imposed by the timing discriminator, was set on the stop energy. The start γ-rays between 2 and 4 MeV were detected in a 25 x 127 mm diameter Naton 136 plastic scintillator mounted on an XP1040. The resulting time distribution, which showed an exponential decay on the stop side with a $T_{1/2}$ = 1.1 ns, is consistent with the resolution introduced by the photocathode to dynode 1 transit time variation assuming that the Čerenkov photons were created uniformly in the photomultiplier entrance window.

Because of the high gain of the first dynode of the 8550 photomultiplier, peaks corresponding to the emission of 1, 2, 3 and 4 photoelectrons from the photocathode, can be individually resolved (MO68). Using a variable intensity pulsed light emitting diode* to illuminate the photocathode, the low energy portion of the 8550 energy spectrum was calibrated from 0 to 20 photoelectrons. Energy spectra in this range were then obtained for ^{57}Co(max γ-energy = 136 keV), ^{137}Cs(max γ-energy = 662 keV), ^{54}Mn(max γ-energy = 835 keV) and

* Type XP21 from Ferranti-Packard Electric Limited, 121 Industry Street, Toronto, Ontario.

^{60}Co(max γ-energy = 1330 keV). No increase in counting rate over background was observed for ^{57}Co which produces electrons below the Čerenkov threshold while the ^{137}Cs, ^{56}Mn and ^{60}Co sources produced predominantly single photoelectron events superimposed on an extended distribution. The cut-off of this extended distribution was energy dependent, corresponding to approximately 15 photoelectrons for ^{60}Co, and was larger than that predicted by random adding during the 3 μs amplifier integrating time constant.

CHAPTER IV

DATA ANALYSIS

A. Fitting Procedures

The experimentally measured "delayed" start-stop time distribution d(t) is given by the convolution of the true distribution of the emitted radiation , f(t), with the system response function p(t):

$$d(t) = \int_{-\infty}^{\infty} f(t')\, p(t-t')\, dt'$$

In general, the delayed distribution, d(t) will be superimposed upon a background of chance coincidences, BG(t), and f(t) will consist of a prompt component $(1 - \eta)\ \delta(t)$ plus a delayed component, $\eta\ f_d(t)$:

$$d(t) = (1-\eta) \int_{-\infty}^{\infty} \delta(t')\, p(t-t')\, dt' +$$

$$\eta \int_{-\infty}^{\infty} f_d(t)\, p(t-t')dt' + BG(t) \qquad \text{IV.1}$$

The simplest case that can be considered is the one where $f_d(t)$ is a single exponential decay:

$$f_d(t) = \frac{1}{\tau} \; e^{-t/\tau}$$

and where τ is much greater than the slope of $p(t)$. When the chance background is subtracted from $d(t)$, the exponential decay is then displayed directly in the resulting spectrum so that τ can be obtained by measuring its exponential slope. The slope method is usually the most reliable procedure for analysing a delayed coincidence experiment since the fitting region can be chosen far enough down on the time spectrum to make the effect of a prompt component and of the prompt response negligible.

As τ becomes comparable to the prompt slope, a knowledge of $p(t)$ and of η becomes more important. One method that can be applied in this case is to construct the complete delayed spectrum $d(t)$ using Eq. IV.1 and fit this to the experimental data. The experimentally measured response function is used for $p(t)$ and the model parameters η and τ are varied in order to obtain the best fit to the data. When $f_d(t)$ cannot be described by a simple exponential decay, then additional model parameters must be used and included in the fitting procedure.

When a model function $Y(t)$ is to be fitted to

a discrete experimental distribution X(t), a goodness of fit criterion χ^2/n can be defined (e.g. LY69):

$$\chi^2/n = \frac{1}{N-\nu} \sum_{t=1}^{N} \frac{[X(t) - Y(t)]^2}{X(t)} \qquad \text{IV.2}$$

where N is the number of data points in X(t)

ν is the number of free parameters in Y(t)

For an experiment in which the correct model and the best values for the parameters have been used, χ^2/n is expected to be equal to 1. However the experimental χ^2/n values will be statistically distributed about this point, the variance in the distribution depending on $N-\nu$. Tables are available (i.e. HA59) which give the probability that a given value for χ^2/n will be exceeded for a particular $N-\nu$. This allows the experimental χ^2/n values to be checked for a significant departure from 1, which would indicate an incorrect choice of the model or model parameters.

The χ^2/n criterion is useful in setting up a procedure to determine the optimum model parameters. A given parameter can be varied in steps and the χ^2/n calculated for each value. The value of the parameter which minimizes the χ^2/n is then the optimum, and the

width of the χ^2/n distribution gives its statistical uncertainty. If there are several parameters to be optimized, it may not be sufficient to optimize each one independently since the location of the minimum of one parameter may depend on the present value of the others. Thus when more than one parameter is to be varied, a procedure for searching out the absolute minimum in the χ^2/n such as that described in Chapter V(C) and in section (E) of the present Chapter must be used.

B. Moment Analysis of Time Spectra

1. Introduction

A second procedure which can be applied for the short τ case is to use the moments of the prompt and delayed time spectra to evaluate τ. Discussions of this moment analysis have been given (BI59, WE60, ME67), but generally these have been limited to the 3^{rd} moment and below, and have neglected the presence of a prompt component in the delayed spectra. Here the moment analysis is extended to the 5^{th} order and prompt correction factors are determined.

Each moment of the delayed spectrum gives a separate estimate for the mean life τ. The use of a number of the higher moments for the analysis of a particular spectrum, then provides a check on the consis-

tency of the experiment, as errors such as those due to

(1) correction for a prompt component in the delayed spectrum

(2) the presence of more than one decay component

(3) subtraction of chance background

(4) statistical bias in each estimator for τ (LY69)

enter into each moment analysis differently. As pointed out by Weaver and Bell (WE60) in their third moment analysis, another advantage in the use of the higher order moments is that the moments of the spectra can be calculated about their own centroids, rather than about a fixed t = 0 in order to make a first order correction for any spurious experimental centroid shifts.

2. Derivation of the n^{th} Moment Estimate for τ

The n^{th} moment of a function g(x) about the point x_o is defined by

$$M_n(g) = \int_{-\infty}^{\infty} (x-x_o)^n \, g(x) \, dx \qquad \text{IV.3}$$

Assuming a single exponential decay, the 1^{st} moment of the "true" time distribution for the radiation, f(t), about t = 0 is then given by

$$M_1(f) = \int_0^\infty [(1-\eta)\ \delta(t) + \eta\ \frac{1}{\tau}\ e^{-(t)/\tau}]t\ dt$$

$$M_1(f) = \eta\tau \qquad \text{IV.4}$$

The higher moments of f(t) are to be calculated about this centroid position:

$$M_n(f) = \int_{-\infty}^{\infty} [t-\eta\tau]^{\,n}\ f(t)dt \qquad \text{for } n \geq 2$$

which gives directly:

$$M_2(f) = (2\eta-\eta^2)\ \tau \qquad \text{IV.5}$$

$$M_3(f) = 2\eta(3-3\eta + \eta^2)\ \tau^3 \qquad \text{IV.6}$$

$$M_4(f) = 3\eta(8-8\eta + 4\eta^2-\eta^3)\ \tau^4 \qquad \text{IV.7}$$

$$M_5(f) = 4\eta(30-30\eta + 15\eta^2 - 5\eta^3 + \eta^4)\ \tau^5 \qquad \text{IV.8}$$

The moments of d(t), p(t) and f(t) are related to one another by Bay's theorem (BA50, BA55), or by application of transform techniques:

$$M_n(d) = \sum_{k=0}^{n} \frac{n!}{k!\,(n-k)!}\ M_{n-k}\ (p)\ M_k(f) \qquad \text{IV.9}$$

Expanding this expression for the cases n = 1 to 5, and using equations IV.4 to IV.8 gives the n^{th} moment estimate for the mean life, τ_n, in terms of η and the experimentally measured moments of p(t) and d(t):

$$\tau_1 = \left[\frac{1}{\eta} \right] \left[M_1(d) - M_1(p) \right] \qquad \text{IV.10}$$

$$\tau_2 = \left[\frac{1}{2\eta-\eta^2} \right]^{1/2} \left[M_2(d) - M_2(p) \right]^{1/2} \qquad \text{IV.11}$$

$$\tau_3 = \left[\frac{1}{\eta(3-3\eta+\eta^2)} \right]^{1/3} \left[\frac{M_3(d) - M_3(p)}{2} \right]^{1/3} \qquad \text{IV.12}$$

$$\tau_4 = \left[\frac{-a\, M_2(p) + \frac{1}{3}[\, 9a\, M_2^2(p) + 3b(M_4(d)-M_4(p))\,]^{1/2}}{b} \right]^{1/2} \qquad \text{IV.13}$$

where $a = -2\eta-\eta^2$

$b = \eta(8-8\eta + 4\eta^2-\eta^3)$

$$c\,\tau^5 + d\,M_2(p)\tau^3 + e\,M_3(p)\tau^2 - [M_5(d) - M_5(p)] = 0 \qquad \text{IV.14}$$

where $c = 4\eta(30-30\eta + 15\eta^2 - 5\eta^3 + \eta^4)$

$d = 20\eta(3-3\eta +\eta^2)$

$e = 10\eta(2-\eta)$

In the derivation of Eqs. IV.11 to IV.14, since the

higher moments are calculated about their centroid positions, $M_1(d)$ and $M_1(p)$ have been set equal to zero. In equation IV.13 the complex root has been dropped.

Eqs. IV.10 to IV.13 give the 1^{st} to 4^{th} moment estimates for τ in terms of the moments of the experimental prompt and delayed spectra, while IV.14 is the equation that the 5^{th} moment estimate satisfies. One real and four complex roots were obtained for the 5^{th} order Equation in all cases, and the real root was selected as the 5^{th} moment estimate for τ.

3. Effect of Prompt Component

The effect of the presence of a prompt component in the delayed spectra is contained in Eqs. IV.10 to IV.14. In order to investigate the size of this effect for each estimator, an n^{th} moment prompt correction factor, δ_n can be defined:

$$\tau(\eta = \eta) = (1 + \delta_n)\ \tau(\eta = 1)$$

For the first 3 moments, the factor $(1 + \delta_n)$ is given in terms of η only, by the quantity inside the first set of square brackets in Eqs. IV.10 to IV.12. The 4th and 5th moment correction factors, however, depend on the relative shape of the prompt and delayed spectra,

in addition to η, so that δ_4 and δ_5 can only be determined for a specific experimental case. Using a typical delayed time spectrum (vanadium run #5, as described in Chapter V(G)), and the corresponding empirical response function, δ_4 and δ_5 were calculated for a range of η. Eqs. IV.13 and IV.14 were solved using a number of values of η and the ratio of each resulting τ to the τ obtained by setting $\eta = 1$, yielded the prompt correction factor. Repeating these calculations using a δ-function response rather than the experimental one, reduced both δ_4 and δ_5 by approximately 30%.

The prompt correction factors obtained for $n = 1$ to 5 and for η between 0.05 and 0.95, are shown in Fig. IV.1. It is interesting that for the higher 3 moments, the influence of the prompt component is greatly reduced, e.g. for a 30% prompt component, δ_3, δ_4 and δ_5 are all less than 3% while $\delta_2 = 5\%$ and $\delta_1 = 43\%$. Thus for experiments where a large prompt component is present, the use of higher moments in determining τ becomes more important.

4. Statistical Error in the Moment Estimators

While higher order estimates for τ can easily be calculated using a computer, the statistical error in the n^{th} moment estimate increases rapidly with n

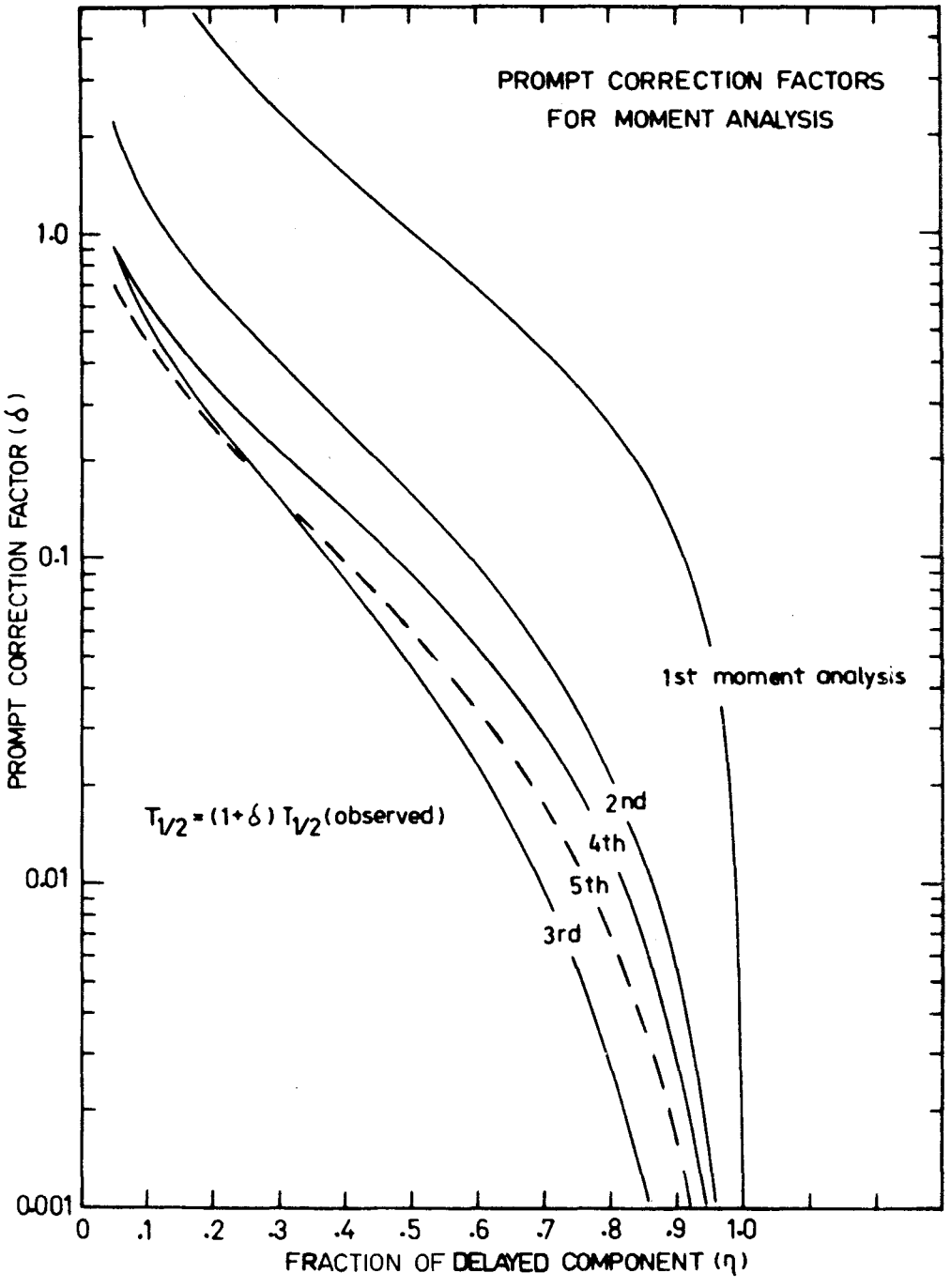

Fig. IV.1 Factors to correct the lifetime as obtained from a moment analysis of the time spectra for the presence of a prompt component.

for n>5. Assuming a δ-function response, the statistical error is the n^{th} moment estimate for τ, εn(τ), has been calculated in Appendix I. For $n \geq 2$, two situations were considered: the case in which the error due to the centroid variance was ignored, and the case where the full centroid variance error was added to case 1. The expressions determined for the two cases are:

$$\varepsilon n(\tau) = \frac{\sqrt{(2n)!}}{nn!} \quad \frac{1}{\sqrt{N_o}} \qquad \text{(no centroid variance)}$$

$$\varepsilon_n'(\tau) = \left[\frac{\sqrt{(2n)!}}{nn!} + \sqrt{2} \right] \frac{1}{\sqrt{N_o}} \qquad \text{(full centroid variance)}$$

(where N_o is the total number of counts in the spectrum)

These errors are plotted in units of $\sqrt{N_o}$ for n = 1 to 8, in Fig IV.2. Because of covariance between the error in the n^{th} moment estimate and the error in the centroid position, the upper curve of Fig. IV.2 will be an over-estimate, and the true statistical error will lie between the two curves. While the calculations of Appendix I in general represent a lower limit to the statistical error, since the large influence of a finite prompt width has been neglected, it is clear from Fig. IV.2 that the rapid increase of the error with n will limit the number of moments that can be usefully applied to calculate τ.

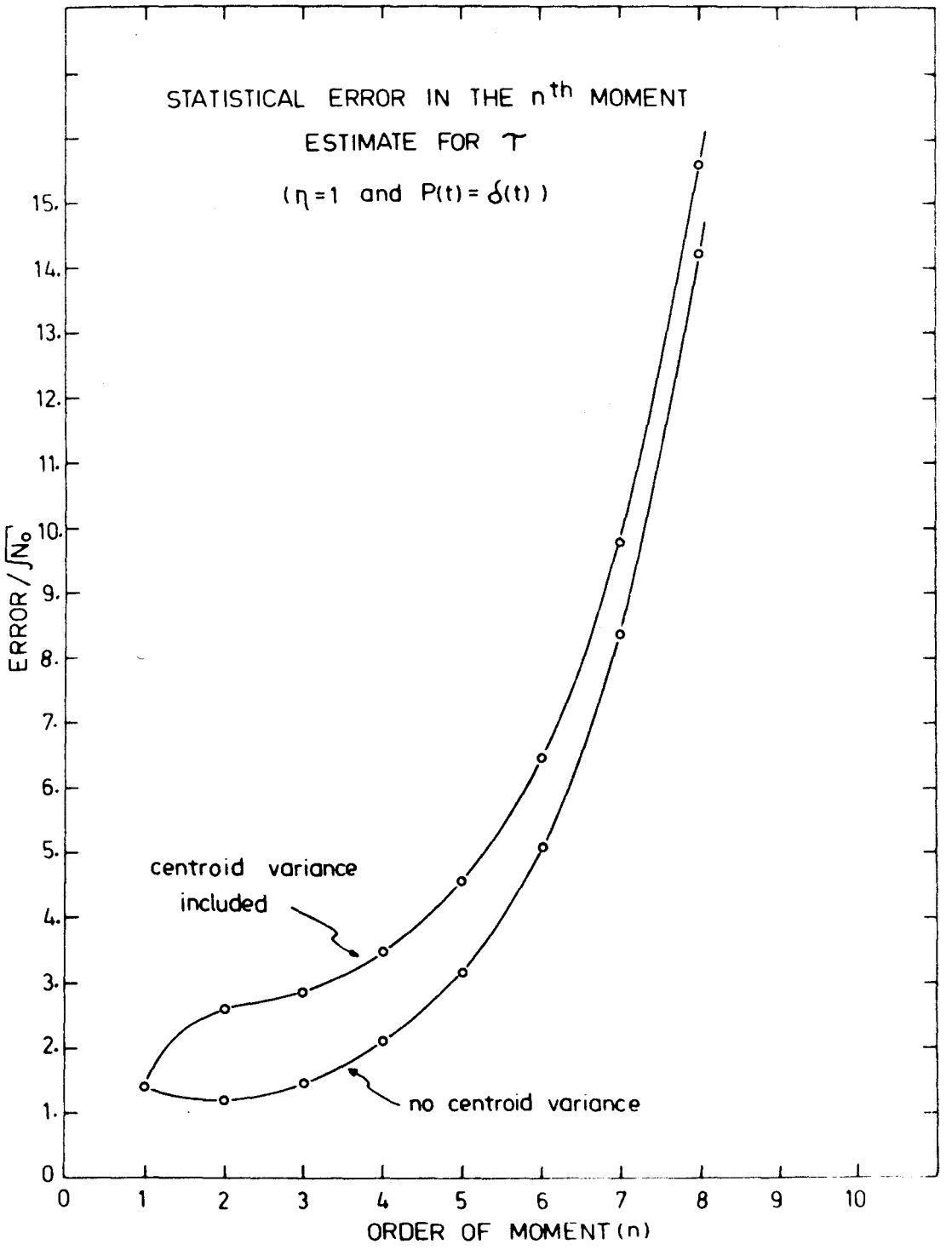

Fig. IV.2 Statistical error in the lifetime estimate obtained from an n^{th} moment analysis of the time spectrum.

C. Two Parameter Centroid Shift Analysis

1. Introduction

The effects which limit the accuracy of the first moment (centroid shift) method of measuring nuclear lifetimes have been extensively discussed (e.g. SC63, BE67). When the prompt and delayed sources are exchanged, spurious shifts can be caused by

1) counting rate effects
2) different pulse height distributions in the energy windows
3) electronic drift and instability
4) scattering of radiation between detectors
5) different effective interaction location in the scintillator for the prompt and delayed radiation.

By the use of small scintillators and appropriate geometry the effects 4) and 5) can be minimized while 1), 2) and 3) are more difficult to reduce. The centroid shift procedure used here consists of recording the time spectra in a two dimensional array S(E,t), where E is the stop energy and t is the start-stop time interval, as described in Chapter II. The centroid position of the time spectrum in each energy group is calculated in order to give the centroid-energy function (CEF) (i.e. walk curve). The shape of the CEF in the prompt

region of the energy scale is then determined and extrapolated to the delayed region in order to obtain the centroid shift. The shifts due to 1), 2) and 3) are hence largely estimated since the prompt and delayed information is simultaneously acquired using the same source.

2. Shape of the CEF

The CEF is given by

$$\langle t(E) \rangle = \frac{\int_0^\infty tS(E,t)dt}{\int_0^\infty S(E,t)dt}$$

The spectrum at any energy can be decomposed into a prompt and delayed component:

$$S(E,t) = S_p(E,t) + S_d(E,t)$$

with time distributions:

$$S_p(E,t) = F_p(E)\ \delta(t-t_o(E))$$

$$S_d(E,t) = \frac{F_d(E)}{\tau} \exp- \left[\frac{t-t_o(E)}{\tau} \right]$$

where τ is the mean life of the delayed component.

Thus the CEF is equal to

$$\langle t(E) \rangle = t_o(E) + \frac{F_d(E)}{F_p(E)+F_d(E)} \tau$$

Statistical analysis by Post and Schiff (PO50) and by Sigfridsson (SI67) have shown that for a NaI detector at a triggering of 1 photoelectron, and for the number of photoelectrons released from the photocathode, R >> 1, it is expected that

$$t_o(E) \underset{\sim}{} \frac{\alpha}{E} + t_D$$

where t_D is a fixed electronic delay.

As a qualitative example, consider the situation in which the prompt distribution is described as a constant, $F_p(E) = \beta$, while the delayed distribution exhibits the gaussian behaviour:

$$F_d(E) = \frac{1}{\sqrt{2\pi}\ \sigma} \exp - \frac{(E-E_o)^2}{2\sigma^2}$$

Also consider the case where the prompt distribution is dominant ($\beta >> 1$). Then $F_p(E) + F_d(E) \underset{\sim}{} \beta$ and

$$\langle t(E) \rangle = \frac{\alpha}{E} + t_D + \frac{\tau}{\beta} \exp - \frac{(E-E_o)^2}{2\sigma^2}$$

In this idealized situation, the CEF can be described as a Gaussian peak of magnitude $\frac{\tau}{\beta}$, centered at E_o, superimposed upon a hyperbolic background. As is well known (BA55), convolution of the prompt response in the time domain does not affect the validity of these results.

It was observed that for a triggering level of 1 photoelectron, the CEF did not display the predicted $\frac{1}{E}$ dependence. Consequently a higher order polynomial was used in the analysis to obtain a satisfactory fit to the prompt region of the CEF.

D. Chance Coincidence Background

In a delayed coincidence experiment, in addition to the "true" start-stop events, there will be a "chance" component in the observed time spectrum which arises from uncorrelated start-stop events. A point which has not generally been recognized however is that the intensity of this chance background will be different above and below the prompt position.

In the absence of a prompt peak, the chance has a distribution:

$$C(t) = \frac{R_{start}}{R_s} e^{-R_s t}$$

where R_{start} is the start counting rate and R_s

is the stop counting rate

If a prompt peak is present in the time spectrum, the chance distribution will be modified to:

$X(t) = C(t) \times$ (Probability that a true event, i.e. an event in the prompt peak, has not been detected)

or:

$$X(t) = \frac{R_{start}}{R_s} e^{-R_s t} \left[1 - \varepsilon \frac{\int_o^t p(t)dt}{\int_o^\infty p(t)dt} \right] \qquad \text{IV.15}$$

where ε is the total probability for detection of a "true" stop event (i.e. for a 2γ cascade in which the first γ ray serves as the start event, ε is equal to the probability for detection of the second γ ray.)

For the case of a Gaussian prompt response with standard deviation σ which is centered at $t = t_o$:

$$p(t) = \frac{1}{\sqrt{2\pi}\ \sigma} e^{-\frac{(t-t_o)^2}{2\sigma^2}}$$

so that $\int_o^\infty p(t)dt = 1$

$$\text{and } \int_o^t p(t)dt = \frac{1}{2} - \frac{1}{2}\,\text{erf}\,\frac{(t-t_o)}{\sqrt{2}\,\sigma} \quad \text{for } 0 \leq t \leq t_o$$

$$= \frac{1}{2} + \frac{1}{2}\,\text{erf}\,\frac{(t-t_o)}{\sqrt{2}\,\sigma} \quad \text{for } t > t_o$$

Thus for the Gaussian prompt response Eq. IV.15 becomes

$$X(t) = \frac{R_{start}}{R_s} e^{-R_s t} \left[1 - \frac{\varepsilon}{2}\left(1-\text{erf}\frac{(t-t_o)}{\sqrt{2}\,\sigma}\right)\right] \quad \text{for } 0 \leq t < t_o \qquad \text{IV.16}$$

$$= \frac{R_{start}}{R_s} e^{-R_s t} \left[1 - \frac{\varepsilon}{2}\left(1+\text{erf}\frac{(t-t_o)}{\sqrt{2}\,\sigma}\right)\right] \quad \text{for } t > t_o$$

In the limit of a δ-function prompt response, i.e. for σ=0:

$$\text{erf}\,\frac{(t-t_o)}{\sqrt{2}\,\sigma} = 1$$

and Eq. IV.16 reduces to:

$$X(t) = \frac{R_{start}}{R_s} e^{-R_s t} \qquad \text{for } 0 \leq t < t_o \qquad \text{IV.17}$$

$$= \frac{R_{start}}{R_s} e^{-R_s t} [1 - \varepsilon] \qquad \text{for } t > t_o$$

Thus for a δ-function prompt response, the intensity of the chance just below the prompt is reduced by the factor $(1 - \varepsilon)$ relative to the intensity of the chance just above the prompt.

For an experimental situation where the chance component, X(t) is to be subtracted out of a measured time spectrum M(t), an iterative procedure can be used. The prompt component is considered to be negligible compared to the chance background outside the upper and lower limits of t_1 and t_2, and the function:

$$F(t) = N_1 e^{-\lambda t} \quad \text{for} \quad 0 < t < t_1$$

$$= N_2 e^{-\lambda t} \quad \text{for} \quad t_2 < t < \infty$$

is then fitted to M(t) over the regions on either side of the prompt region in order to determine N_1, N_2 and λ (Fig. IV.3). Comparing F(t) with the function X(t) defined by Eq. IV.17, it follows that

$$1 - \varepsilon = \frac{N_2}{N_1}$$

or

$$\varepsilon = 1 - \frac{N_2}{N_1} \qquad \text{IV.18}$$

The measured time spectrum, M(t) is equal to the sum of the chance distribution, X(t) and the prompt component, p(t) so that

$$p(t) = M(t) - X(t) \qquad \text{IV.19}$$

Using Eq. IV.18 and Eq. IV.19 in Eq. IV.15 gives an integral equation for p(t) in terms of the measured time

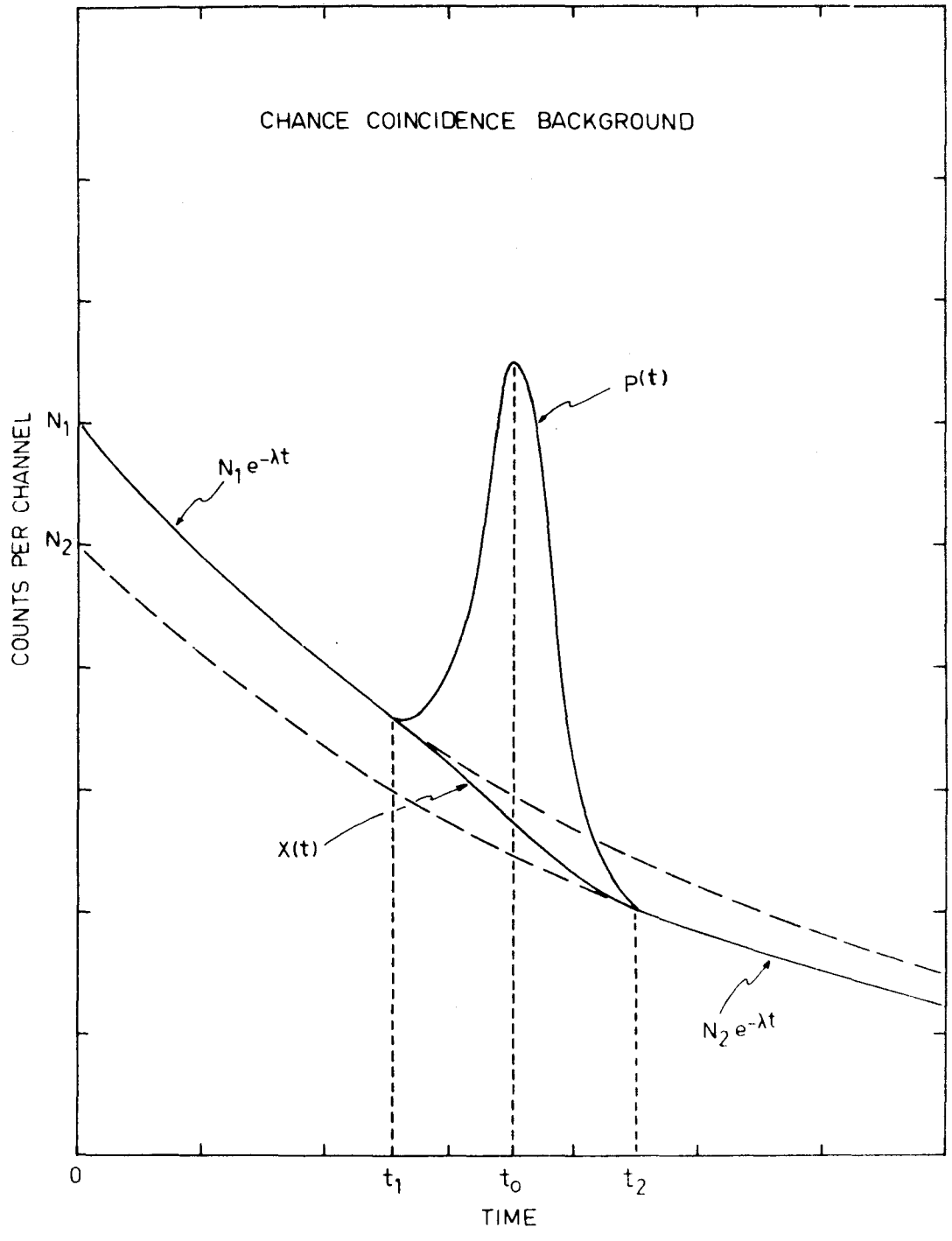

Fig. IV.3 Subtraction of the chance coincidence background from the measured time distribution.

spectrum and the fitted parameters N_1, N_2 and λ:

$$p(t) = M(t) - N_1 e^{-\lambda t}\left[1-(1-\frac{N_2}{N_1})\frac{\int_0^t p(t)dt}{\int_0^\infty p(t)dt}\right] \qquad \text{IV.20}$$

The initial approximation p(t)=M(t) can be made in this equation to obtain an improved estimate for p(t), and the iterations can then be repeated until satisfactory convergence is obtained. This background subtraction procedure is equally valid for the case where p(t) is convolved with an exponential decay function provided an appropriate choice for t_2 is made.

For the case where there is insufficient experimental data to determine either N_1 or N_2, Eq. IV.20 can be rearranged to remove the explicit dependence on either N_1 or N_2. Since the number of counts removed from the chance distribution by the presence of the prompt component must be equal to the area of the prompt, the following relationship holds (Fig. IV.3)

$$(N_1-N_2)\int_{t_o}^{\infty} e^{-\lambda t}\,dt = \int_0^\infty p(t)dt \qquad \text{IV.21}$$

where t_o is the centroid position of p(t):

$$t_o = \frac{\int_0^\infty t\,p(t)dt}{\int_0^\infty p(t)dt} \qquad \text{IV.22}$$

Solving Eq. IV.21 and Eq. IV.22 then gives

$$N_2 = N_1 - \lambda \exp\left[\lambda \frac{\int_0^\infty t\, p(t)dt}{\int_0^\infty p(t)dt}\right] \int_0^\infty p(t)dt$$

which can be used along with Eq. IV.20 to apply the background correction when either N_1 or N_2 is not known.

E. Analysis of Experimental Data

1. Fitting Analysis

For the slope analysis of the time spectra, a fitting program (AR60) was used to fit a flat chance background plus a single exponential to the data. The program iteratively varied the background intensity and the exponential mean life and converged to the values which minimized the χ^2/n. The optimum mean life and background intensity, and their 66% confidence limits as determined from the width of the χ^2/n distribution, were printed out along with the minimum χ^2/n which was obtained.

When fitting to the complete time spectra, a procedure was developed which allowed a two parameter minimization to be made. The time spectra was constructed and the χ^2/n calculated using the experimental response function and trial values for the two parameters to be optimized. The two parameters were then independently varied in steps, and the χ^2/n which was obtained for each case was displayed in the form of constant χ^2/n contours in the space spanned by the two variable

parameters (e.g. Fig. V.6). While each lifetime analysis required approximately one minute of CDC 6400 computing time (depending on the grid size), using this method more reliable information is obtained regarding the location and error in the absolete minimum than when a technique which searches out and converges to the minimum χ^2/n is used.

2. Higher Moment Analysis

A computer program was written to obtain the 2nd, 3rd, 4th and 5th moment estimates for τ. The experimental prompt and delayed spectra, and the delayed intensity η, were read in on punched cards and the moments of each spectrum were calculated about the centroid position. Eqs. IV.11, IV.12 and IV.13 then directly yielded the 2nd, 3rd and 4th moment estimates for τ while the 5th moment estimate was obtained by solving Eq. IV.14. This 5th order equation was iteratively solved using a standard CDC 6400 subroutine and in all cases convergence to 1 real and 4 complex roots was obtained in less than 0.1 second. The real root was then accepted as the 5th moment estimate.

3. Two Parameter Centroid Shift Analysis

In order to determine the centroid shift, the extrapolation of the prompt to the delayed region was made by either fitting a polynomial to the prompt regions

or by obtaining a separate prompt CEF using a mercury capture source and shifting this so as to line up with the delayed CEF over its prompt region. The delayed fraction, $\eta(E)$ was obtained directly from the coincidence energy spectrum, i.e. from the summed counts in each energy group. Estimates for τ were obtained from each energy group in the delayed region using Eq. IV.10, and the mean, weighted according to the statistical error, was then calculated. As an illustration of these procedures, Figs. V.2 and V.3 show the analysis of typical experimental data using the fitted function and fitted prompt methods.

All calculations were performed on IBM 7040 and CDC 6400 computers. In determining the delayed fraction, $\eta(E)$, the prompt background under the delayed photopeak in the coincidence energy spectrum was assumed to be linear. In all cases where the chance background was significant, it was calculated and subtracted separately for the regions above and below the centroid of each time distribution. In the fitted function analysis, the polynomial fitted by least squares to the prompt centroid position had one of two forms:

$$\frac{\alpha}{E} + \beta + \gamma E$$

$$\text{or} \quad \frac{\alpha}{E} + \beta + \gamma E + \xi E^2$$

In cases where there is a significant amount

of Compton interaction of the delayed γ ray in the detector, a portion of the CEF below the photopeak will also have a centroid shift. Thus if the prompt CEF is fitted over this shifted region, an underestimate for τ will be obtained. An iterative procedure was included in the computer programs which allowed a correction for this effect to be made if the detector lineshape was known.

CHAPTER V

EXPERIMENTAL RESULTS

A. Introduction

For all of the lifetime measurements sufficiently long counting times were used that the statistical uncertainty was negligible. The accuracy was then limited by systematic effects and an effort was made to evaluate these errors. The lifetime experiments were repeated using different experimental conditions and each resulting spectrum was analysed using a number of the procedures described in Chapter IV. In addition to allowing the detection of any systematic effects, an estimate for the error in the halflife can be obtained from the distribution in the individual experimental results using the Student t-distribution (e.g. FR62).

The 100 Mhz oscillator procedure described in Chapter V was used to measure the system integral non-linearity and to calibrate the timescale. For all runs, the error in the halflife due to this source was less than 1%.

The Compton distribution from a natural mercury neutron capture source was used to measure the prompt response of the system. As has been shown by Hohenemser et al (HO70), the time response of thin NaI detectors at low energies is essentially the same for the Compton and photoelectric interaction.

Except for ^{40}K and ^{56}Mn, all levels above the delayed level being measured were assumed to have negligible lifetimes. When it was necessary to subtract the chance coincidence background, this was assumed to have a flat distribution.

B. Displaced Source Experiment

Since the two parameter centroid shift technique proved to be a rather useful method for measuring short lifetimes, and since no previous reference could be found to its use, an experiment to test the procedure was performed (BO70c). A β-decay source was moved through measured distances relative to a second fixed source, and the observed centroid shifts were compared to the values predicted using the speed of light.

The fast-slow delayed coincidence system shown in Fig. III.2 was used for the experiment. An SCA selected start γ-rays in the energy range 1100 ± 50 keV as detected in a 38 mm x 50 mm diameter, NaI detector. Stop γ-rays between 50 keV and 1400 keV were detected in a 25 mm x 25 mm diameter NaI and recorded in the

energy dimension.

Two sources were located on the line joining the two detectors. A ^{60}Co source was fixed in position close to the start detector and a ^{46}Sc source mounted on an optical bench was free to move between the ^{60}Co source and the start detector. Both decays lead to two γ cascades in which the intermediate state has a negligible lifetime, $T_{1/2} \leq 4$ ps (LE67) (1.33 MeV and 1.17 MeV for ^{60}Co and 0.89 MeV and 1.12 MeV for ^{46}Sc). The energy spectrum in the stop detector in coincidence with the 1.15 MeV start region thus consists of the 1.33 MeV and 0.89 MeV lines. The 0.89 MeV line will be delayed by an amount equal to twice the separation of the two sources with respect to the 1.33 MeV background and a corresponding centroid shift will appear at this energy and below its Compton edge at 0.69 MeV. The ^{46}Sc source was moved in 1.000 cm steps and the two parameter energy-time spectrum acquired for four different positions. After the four runs, the ^{46}Sc source was removed and a ^{60}Co prompt run obtained.

The centroid shift of the 0.89 MeV line was determined for each ^{46}Sc position using both the fitted function and fitted prompt analysis procedures. The ^{60}Co prompt CEF or the function:

$$\frac{\alpha}{E} + \beta + \gamma E + \xi E^2$$

was fitted over the prompt regions on either side of the 0.89 MeV peak and the centroid shift, equal to the effective mean life, τ, calculated.

The results obtained using the two analysis procedures are shown in Fig. V.1 where the centroid shifts corresponding to effective mean lives in the range 150 to 350 ps are plotted vs. the ^{46}Sc source position (using an arbitrary zero). Because the low photopeak efficiency of the small NaI stop detector reduced the size of the delayed peak relative to the prompt background beneath it, the observed shifts ranged from 75 to 175 ps. A least squares fit of a straight line with a slope fixed by the speed of light was made to the experimental points. The intercept, a, and goodness of fit criterion, χ^2/f, for the two analysis procedures:

Fitted function	$a = -10 \pm 8$ ps	$\chi^2/f = 1.76$
Fitted prompt	$a = 5 \pm 11$ ps	$\chi^2/f = 0.56$

indicate satisfactory agreement within the statistical uncertainty. Because of the poor geometrical efficiency of the experiment, the accuracy of these results was limited by the statistical error.

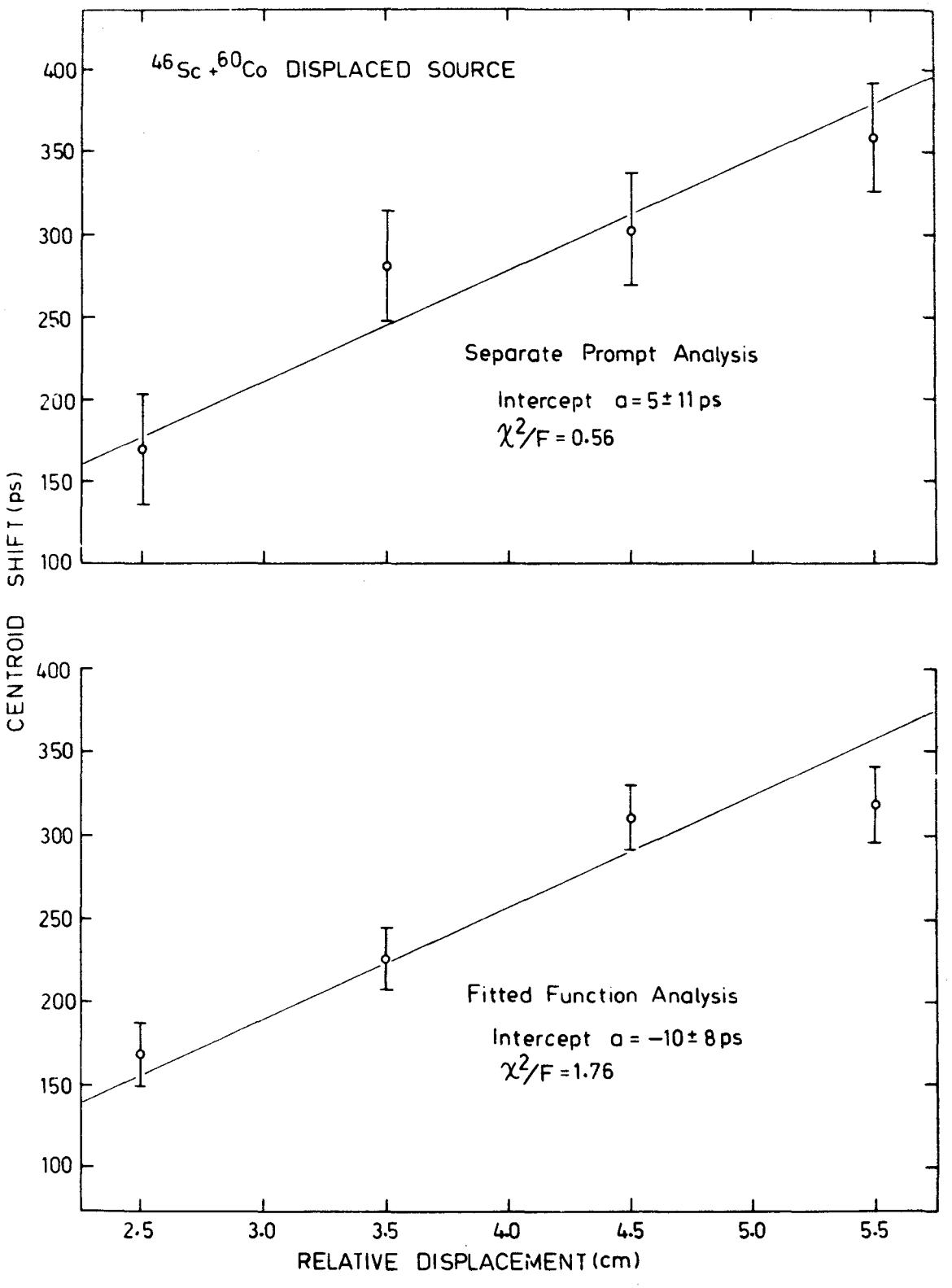

Fig. V.1 Results of displaced source experiment

C. Lifetime of the 31.2 keV Level in ^{28}Al

The halflife of the 31.2 keV level in ^{28}Al populated by thermal neutron capture in natural aluminum was measured using the two parameter fast-slow delayed coincidence system shown in Fig. II.2 (BO70c). Six runs were performed using different experimental conditions, and the two parameter data was analysed using the slope and fitted function centroid shift procedures.

Start γ rays in the range 0.5 MeV to 1.0 MeV were detected in a 38 mm x 46 mm diameter Naton 136 plastic scintillator mounted on an 8575. Stop γ rays between 2 keV and 60 keV were detected in a 12 mm x 25 mm diameter NaI mounted on an 8575 and were stored in the energy dimension.

Fig. V.2 illustrates the analysis of a typical ^{28}Al run. In (a), the points are the experimental centroid position plotted vs. the stop energy while the line is the function

$$\frac{\alpha}{E} + \beta + \gamma E$$

fitted to the CEF. The fit was made over the two regions on either side of the 31 keV photopeak, 10-19 keV and 38-62 keV, where the radiation is prompt. The resulting centroid shift:

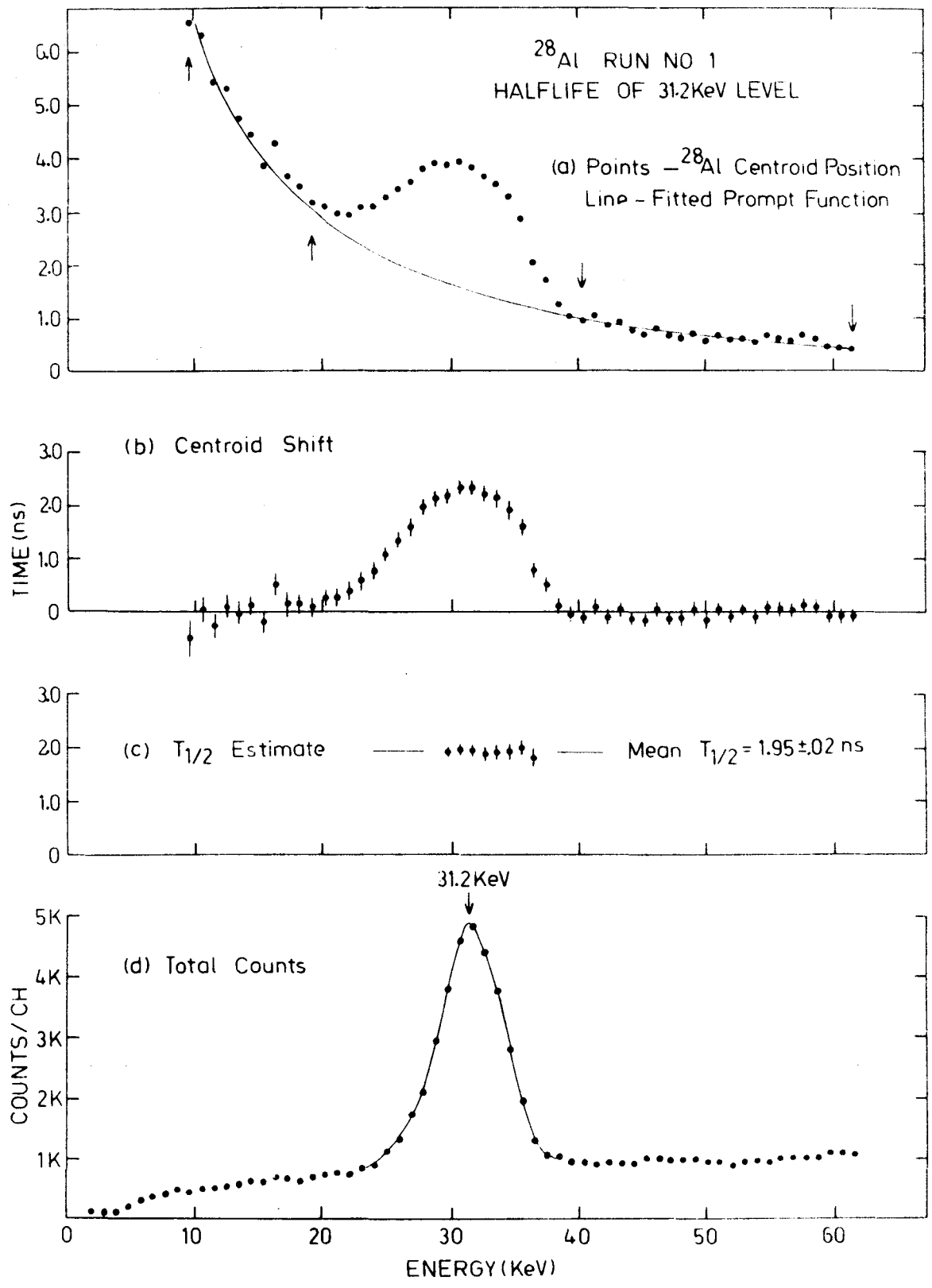

Fig. V.2 Centroid shift analysis to measure the lifetime of the 31.2 keV level in ^{28}Al

$$\langle t(E) \rangle - \left(\frac{\alpha}{E} + \beta + \gamma E\right)$$

is shown in (b). The prompt correction factors for each channel in the region of the 31.2 keV photopeak were calculated from the coincidence energy spectrum, (d), and the resulting estimates for the halflife are shown in (c). Because of the relatively low thermal neutron capture cross section of ^{27}Al ($\sigma \simeq 0.2$ barns), to minimize possible interference from the delayed 30 keV transition in ^{128}I, and from the iodine K X-ray at 28 keV, excited by thermal neutron capture in the NaI detector, the ^{28}Al halflife was determined from the region above 30 keV. The straightness of the halflife estimate plot in Fig. V.2 (c) indicates that the points that were used in the ^{28}Al measurement were not influenced by the ^{128}I.

No correction for chance background was made in determining the centroid of each time distribution, but this was calculated to introduce less than a 1% error in the halflife. A possible error arises in the centroid shift analysis because a fraction of the 31 keV γ rays which escape the photopeak (but are still above the Compton edge at 3 keV) cause a centroid shift in the prompt region below the peak. The lineshape of the NaI detector at this energy was determined by observing the 32 keV X-rays from ^{137}Cs in coincidence with the

conversion electrons. The resulting correction, as described in Chapter IV.E(3), which was applied, increased the halflife estimates by approximately 1%.

Table V.1 shows the halflife results and statistical error for 6 measurements which were made using different target thickness and start energy windows. The centroid shift analysis yielded a mean $T_{1/2}$= 2.14 $\pm$ 0.01 ns which is in good agreement with the value, $T_{1/2}$ = 2.16 $\pm$ 0.02 ns, obtained from a slope analysis of the same data using a digital window on the two parameter spectra. Including the systematic errors due to timescale calibration and background subtraction, and using the 66% confidence interval based on the distribution in the measured results, an overall error of 3% has been assigned. The final result:

$$T_{1/2} = 2.15 \pm 0.06 \text{ ns}$$

is in agreement with a previous measurement, $T_{1/2}$ = 2.3 $\pm$ 0.2 ns, (TO61), while reducing the error by a factor of 3.

D. Lifetime of the 77 keV Level in ^{32}P

1. Introduction

A delayed coincidence measurement of the half-

TABLE V.1

Measured Values for the Halflife of the 31 keV Level in ^{28}Al

Run No.	Halflife (ns) (from slope)	Halflife (ns) (Centroid Shift)
1	2.14 ± .04	1.95 ± .02
2	2.24 ± .04	2.26 ± .02
3	2.22 ± .06	2.14 ± .03
4	2.08 ± .03	2.08 ± .02
5	2.09 ± .04	2.17 ± .02
6	2.18 ± .03	2.26 ± .02
Mean	2.16 ± .02 ns	2.14 ± .01 ns

life of the 77 keV level in ^{32}P has been published by Mendelson and Carpenter (ME68). By a third moment analysis of data acquired using the $^{31}P(d,p\gamma)^{32}P$ reaction, they obtained the result $T_{1/2} = 360^{-40}_{+60}$ ps. The delayed coincidence value determined here for the 77 keV level populated by thermal neutron capture in natural phosphorus, $T_{1/2} = 253 \pm 25$ ps is significantly lower than that reported above. Consequently a study was made to evaluate any possible systematic effects which could influence the measurement (BO70b).

Ten ^{32}P runs were obtained under different experimental conditions, changing the start energy window, target thickness, electronic arrangement and thickness of quartz crystal fast neutron filtering in the beam, and these runs were then analysed using the fitted function centroid shift procedure. In addition, runs 7 to 10 were analysed by applying slope, third moment and fitted prompt centroid shift techniques.

2. Experimental

High energy capture γ rays detected in a 38 mm x 46 mm diameter Naton 136 plastic scintillator mounted on an 8575 provided the start signal. Energy selection on start events was performed by either using an SCA (runs 1 to 6) or a commercial constant fraction discriminator (GE67, GE68) (runs 7 to 10). The start

energy range used for each run is given in Table V.2. Stop γ rays between 10 keV and 160 keV were detected in a 13 mm x 25 mm NaI detector mounted on an 8575 and these were recorded in the energy dimension.

3. Results and Discussion

The results of the fitted function analysis are given in Table V.2 along with the experimental conditions for each of the 10 runs. An illustration of the fitted function analysis procedure applied to phosphorus run number 8 is given in Fig. V.3. In calculating the centroid position, the chance background as determined outside the timescale integration limits of 6.4 ns below and 12.6 ns above the 77 keV centroid position, was subtracted.

Two prompt runs using 0.1 and 0.4 g/cm^2 thick HgO targets were acquired between phosphorus runs 7 and 8, and 9 and 10, respectively. Table V.3 gives the results of the fitted prompt centroid shift analysis along with the shift that was applied to each of the prompt CEF's in order to align it with the phosphorus run over the prompt region of the CEF. These shifts represent the size of the error which would have occurred in a conventional centroid shift analysis. As observed in the slope and third moment results given in Tables V.4 and V.5 the shape of the phosphorus time spectra is relatively constant, so that the shifts probably result

TABLE V.2

Centroid Shift (Fitted Function) Values for the Half-Life of the 77 keV Level in ^{32}P

Run No.	Start Energy (MeV)	Quartz Filtering (inches)	Target Thickness (g/cc)	Half-Life (ps)
1	0.5 - 2	18	5	161
2	0.5 - 2	18	5	167
3	0.2 - 0.5	18	5	239
4	0.2 - 0.5	18	5	250
5	0.5 - 1	18	7.5	266
6	2.5 - 5	18	7.5	189
7	>0.3	30	2.5	271
8	>0.3	30	2.5	194
9	>0.6	30	2.5	229
10	>0.6	30	2.5	175
Mean				214 ps

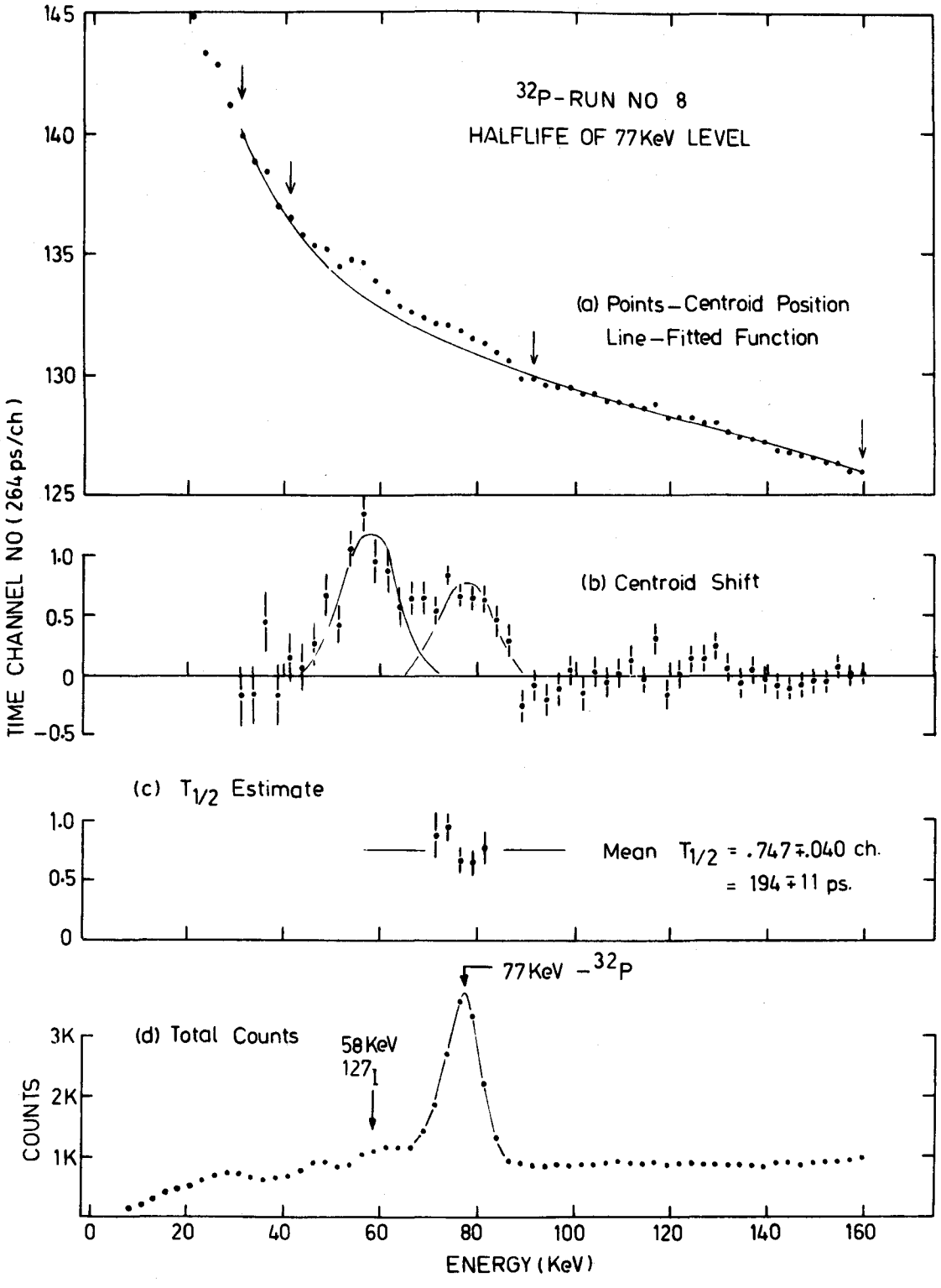

Fig. V.3 Centroid shift analysis to measure the lifetime of the 77 keV level in ^{32}P

from changes in detector geometry or source placement.

A digital window was set to include events in the energy range 72-82 keV and a modified slope analysis of runs 7 to 10 performed. Using the delayed fraction, η, as determined from the coincidence energy spectrum, and the experimental prompt response, delayed time spectra were constructed using Eq. IV.1 for a number of trial values of τ. The slopes of the constructed functions were compared with the slopes of the experimental time spectra in order to determine the values for τ which gave the best fit, and the results, along with the statistical uncertainty, are given in Table V.4. Table V.5 lists the results of a 3rd moment analysis of runs 7 to 10 using the same digital window as for the slope measurement.

As observed in Fig. V.3, a second shifted region exists below the 77 keV peak. Placing a 2 g/cm^2 lead absorber between the target and the detector caused an attenuation of the 77 keV peak and corresponding centroid shift, while a peak and an enhanced centroid shift appeared in the energy spectrum below the 77 keV region. Two additional shifted regions were also observed in this CEF. Based on an energy calibration using a mixed capture source consisting of aluminum (31.2 keV), phosphorous (77 keV) and vanadium (125 keV), these shifted

TABLE V.3

CENTROID SHIFT (FITTED PROMPT) VALUES FOR THE HALF-LIFE OF THE 77 keV LEVEL IN ^{32}P

Run No.	Prompt Shift (ps) (Low Rate Prompt)	Half-Life (ps) (Low Rate Prompt)	Prompt Shift (ps) (High Rate Prompt)	Half-Life (ps) (High Rate Prompt)
7	-82	303	-108	311
8	17	283	- 9	291
9	149	209	121	218
10	175	209	145	223
Mean		251 ps		261 ps

TABLE V.4

SLOPE VALUES FOR THE HALF-LIFE OF THE 77 keV LEVEL IN ^{32}P

Run Number	Half-Life (ps) (Low Rate Prompt)	Half-Life (ps) (High Rate Prompt)
7	250 ± 30	240 ± 30
8	320 ± 36	314 ± 36
9	286 ± 25	279 ± 25
10	252 ± 36	246 ± 36
Mean	277 ps	270 ps

TABLE V.5

THIRD MOMENT VALUES FOR THE HALF-LIFE OF THE 77 keV LEVEL IN ^{32}P

Run Number	Half-Life (ps) (Low Rate Prompt)	Half-Life (ps) (High Rate Prompt)
7	308 ± 28	299 ± 29
8	284 ± 29	274 ± 30
9	275 ± 36	264 ± 38
10	229 ± 48	214 ± 53
Mean	274 ps	263 ps

regions were located at 30 ± 3 keV, 60 ± 3 keV and 135 ± 5 keV, and were ascribed to neutron reactions in the NaI detector.

The centroid shifts at 30 keV and 135 keV were assumed to arise from delayed levels in ^{128}I excited by thermal neutron capture in the NaI detector (chapter II.A(2). However, since the centroid shifts corresponding to these two lines, (and to the 137 keV Compton edge at 47 keV), were not observed in any of the ^{32}P or mercury prompt runs, the effect on the halflife measurement was assumed to be negligible. As the start energy window was raised, or the amount of fast neutron filtering increased, the centroid shift at 60 keV was reduced relative to the shift at 77 keV, following the behaviour expected if this were the 58 keV level in ^{127}I excited by inelastic scattering of fast neutrons in the NaI detector. In the lead absorber run, the intensity of this line was sufficient to allow a slope measurement of its half life. The value obtained was consistent with the measured half life of the 58 keV level in ^{127}I: $T_{1/2}$ = 1.86 ± 0.11 ns (GE66).

The statistical error in the centroid shift methods (less than ± 20 ps in all cases), is not listed in tables V.2 and V.3 since the dominant error, as evidenced by the spread in the measured values, was assumed to arise from systematic effects. It can be

noted that the results obtained using the fitted function centroid shift analysis are significantly lower than those obtained using the other methods. The 60 keV line required that the fitted function be extrapolated over a relatively large region of the CEF and hence the presence of this component adversely affected this method more than it did the others. No systematic correlation with counting rate or on the presence of the delayed 60 keV level (whose relative contribution was altered by changing the start energy window and the ratio of thermal to fast neutron components present in the beam), was observed in the half life results given in table V.2.

In the hope that a systematic error would enter into the different analysis procedures in different ways, the final value for the ^{32}P half life was obtained by averaging the mean values for each method. For runs 7 to 10 these mean values are:

Centroid shift (fitted prompt)	$T_{1/2} = 256 \pm 61$ ps
Slope	$T_{1/2} = 274 \pm 23$ ps
Third moment	$T_{1/2} = 269 \pm 23$ ps

For runs 1 to 10, the mean value is

Centroid Shift (fitted function) $T_{1/2} = 214 \pm 14$ ps

The errors in the results represent the 66% confidence interval based on the distribution in the individual measurements. The error in the final result:

$$T_{1/2} = 253 \pm 25 \text{ ps}$$

has been increased from the 66% confidence interval estimate of ± 10 ps because of possible systematic effects.

E. Lifetime of the 29.4 keV Level in ^{40}K

1. Experimental

Thermal neutron capture on natural potassium was used to populate the 29.4 keV level in ^{40}K (BO69). While naturally occuring potassium is not monoisotopic, 96% of all captures occur in ^{39}K. Two different targets were used: a 3 g/cm^2 sample of potassium metal sealed in a glass tube, and an 0.5 g/cm^2 sample of potassium hydroxide sealed in polyethylene. The different effective source strengths gave different true-to-chance ratios and hence allowed a check on the background subtraction procedure.

The time spectra were stored in a single parameter array using the fast-slow delayed coincidence system shown in Fig. II.2. High energy capture γ-rays between 0.5 MeV and 2.0 MeV were detected in a 38 mm x 46 mm diameter Naton 136 plastic scintillator mounted on an 8575 and these were used to indicate the time of population of the 29.4 keV. level. Full energy 29.4 ± 1 keV events detected in a 1 mm x 46 mm diameter NaI

detector mounted on an 8575 signified the decay of the state.

2. Analysis and Results

Four measurements of the 29.4 keV half life were made changing the timescale, start energy window and target thickness, and the results of a slope analysis of this data are given in table V.6. A typical potassium time spectrum with a constant background of 5 counts per channel subtracted, is shown in Fig. V.4 along with the corresponding prompt (shifted in time).

In addition to the essentially flat chance distribution, the background consisted of a second component with a 340 ns half life. This resulted predominantly from the 29.4 keV level being populated by γ rays which had cascaded through a level at 1.64 MeV with a 340 ns half life (MA68). Other experiments with longer timescales confirmed this and showed that both components were approximately equal in intensity over the region of the 4.26 ns half life which was most sensitive to background subtraction. However a flat background determined from the time spectrum just beyond the point when the 4.26 ns had become negligible was used, and this procedure was calculated to introduce an uncertainty of 1% in the half life.

TABLE V.6

SLOPE VALUES FOR THE HALF-LIFE OF THE 29.4 keV LEVEL IN ^{40}K

Run Number	Half-life (ns)	χ^2/n
1	4.21 ± 0.02	1.50
2	4.28 ± 0.02	1.28
3	4.27 ± 0.03	1.93
4	4.28 ± 0.02	1.57

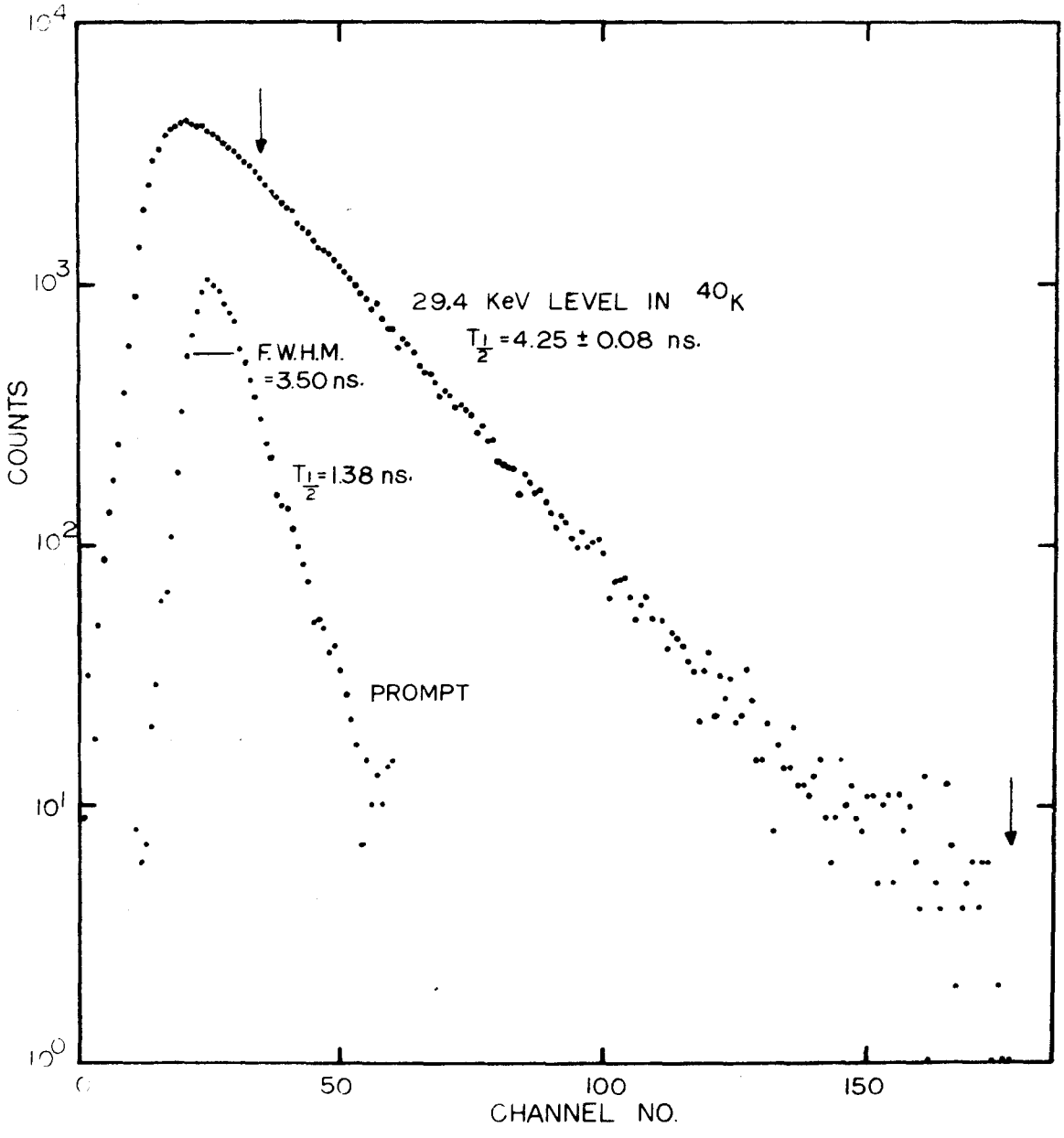

Fig. V.4 Measured time distribution for the 29.4 keV level in ^{40}K

The final result:

$$T_{1/2} = 4.26 \pm 0.08 \text{ ns}$$

is in agreement (with a factor of 4 reduction in the error), with a measurement by Lynch and Holland (LY59) of $T_{1/2} = 3.9 \pm 0.35$ ns, obtained using a pulsed beam technique and the $^{40}Ar(p,n)^{40}K$ reaction.

F. Lifetime of the 52 keV Level in ^{46}Sc

Because of the very long lifetime expected for the 52 keV E2 transition, the effect of the system resolution function was negligible and crossover timing was used in order to reduce the stop rate applied to the TAC. The largest source of error in the measurement was background subtraction and the lower stop rate decreased the intensity of the chance background which had to be subtracted.

A 6 mm x 46 mm NaI and a 1 mm x 46 mm NaI, both mounted on 8575 photomultiplier tubes, were used as the start and stop detectors respectively. The 9th dynode signals were amplified in DDL amplifiers and the bipolar outputs fed to timing SCA's which selected the 215 keV region as the start and the 52 keV region as the stop. The SCA crossover outputs provided the time markers. An additional delay of 6 μs was inserted into the stop side in order to shift the time spectra out along the 80 μs TAC timescale.

The decay of ^{46}Sc following thermal neutron capture has been studied by Bolotin (BO68). From the proposed decay scheme it can be seen that 3 γ-rays will satisfy the 228 keV start window (216 keV, 227 keV and 228 keV) so that in addition to the desired 228 keV - 52 keV cascade, Compton scattered γ rays which satisfy the 52 keV stop window can give rise to additional coincidences. Assuming the 227 keV level to have a negligible lifetime, these coincidences will either be prompt or will have a slope that appears on the start side of the time distribution, so that no interference with the 52 keV measurement is expected.

Seven runs were performed changing the thickness of the scandium oxide target and the width of the stop energy window. The results of a slope analysis of the data, arranged in order of increasing stop rate, are given in table V.7. A check on the background subtraction procedure was provided by changing the stop rate, and as can be seen, the results indicate no significant dependence on the background intensity. A typical ^{46}Sc time spectrum showing the background subtraction, is given in Fig. V.5. The mean value, and an estimate for the error based on the distribution in the measured values:

$$T_{1/2} = 9.62 \pm 0.4 \ \mu s$$

is in agreement with a previous (n,γ) measurement:

TABLE V.7

LIFETIME OF THE 52 keV LEVEL IN ^{46}Sc

Run No.	Stop SCA Rate (cps)	χ^2/n	$T_{1/2}$(μs)
1	13	1.07	10.00 ± 0.41
2	18	0.98	9.22 ± 0.34
3	22	0.94	9.58 ± 0.25
4	35	0.95	10.25 ± 0.45
5	35	1.03	9.04 ± 0.54
6	53	0.92	9.81 ± 0.23
7	69	0.92	9.43 ± 0.18

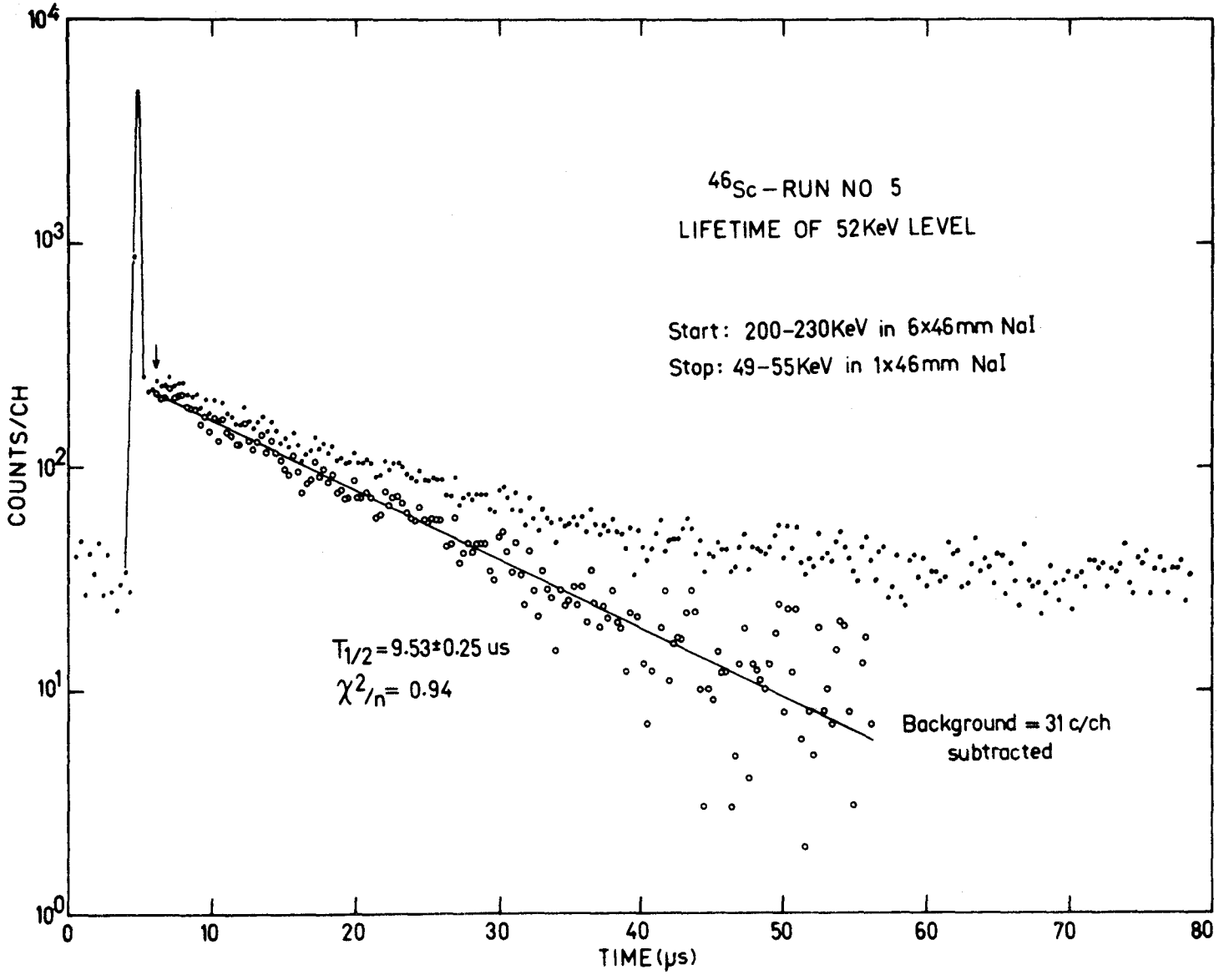

Fig. V.5 Measured time distribution for the 52 keV level in ^{46}Sc

$T_{1/2}$ = 10.6 ± 0.6 μs (KA66) and with the value $T_{1/2}$ = 8.8 ± 0.4 μs (FO68) obtained using the (d,pγ) reaction.

G. Lifetime of the 17.0 keV Level in ^{52}V

1. Experimental

Six measurements of the 17 keV halflife were performed using different experimental conditions, and each run was analysed using a χ^2 fit and second to fifth moment estimators for τ. To minimize self absorption of the 17 keV γ ray, either a 0.001" or 0.004" thick natural vanadium foil was used as the target for the thermal neutrons.

The fast-slow delayed coincidence system shown in Fig. II.2 was used to obtain the data. The start detector was either a 25 x 125 mm diameter Naton 136 plastic scintillator mounted on an XP1040 (runs 1 and 2), a 6 x 25 mm diameter NaI mounted on an 8575 (run 3), or a 50 x 38 mm diameter NaI mounted on an 8575 (runs 4 - 6). The stop detector was a thin window 1 mm x 25 mm diameter NaI, selected for high light output, (~ 11 photoelectrons per keV), mounted on an 8550. In order to optimize the time resolution, the stop timing discriminator was set to trigger at 20% of the single photoelectron pulse height. Energy selection was performed on the start side using an SCA (runs 1 and 2) or by using

the anode energy selection circuit described in chapter II.C(3) (runs 3 - 6). The stop energy selection was obtained using an SCA (run 1) or by acquiring 2 parameter energy-time data and setting a digital window to select the 17 keV photopeak (runs 2 - 6). The prompt response of the system typically displayed a FWHM of 3.3 ns while the slope of the stop side showed a halflife equal to 1.4 ns.

Because of the very low yield of the 17 keV γ ray, (3.0 $\pm$ 1.0 γ-rays per 100 neutron captures, from section (H) of this chapter), and the large γ ray absorption at this energy, a considerable effort was made to obtain a good quality energy spectrum. The 1 mm x 25 mm NaI energy spectrum in coincidence with 2.5 - 5.5 MeV, obtained by summing 17 keV halflife runs 4, 5 and 6, is shown in Fig. V.6. It can be seen that the 17 keV line appears strongly in the spectrum while the line at 30 keV due to neutron reactions in the NaI detector, is almost absent.

2. Analysis and Results

As discussed in chapter III.C, when the very low energy portion of the capture γ ray Compton distribution is used to obtain the system prompt response, the prompt spectrum can be distorted due to the production of Čerenkov light in the NaI detector or in the glass windows of the detector and photomultiplier. This effect was observed

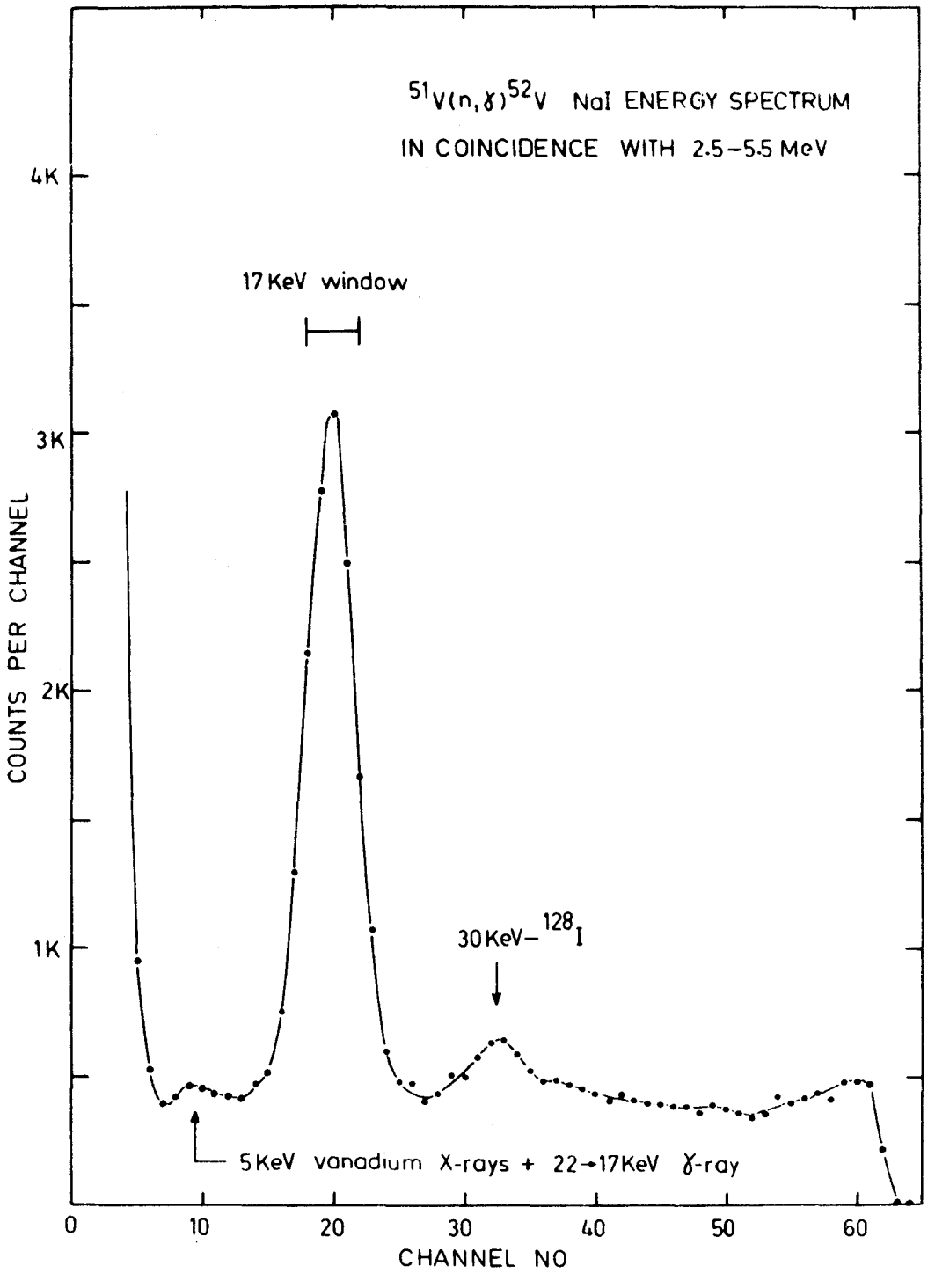

Fig. V.6 ^{52}V coincidence energy spectrum

using the mercury capture source and 17 keV window, and appeared as a shoulder on the start side of the prompt distribution. A 511-511 keV annihilation source, which contained no significant Čerenkov shoulder, was used to represent the system prompt response function $P_1(t)$, while the mercury capture source was used to represent the prompt component, $P_2(t)$, present in the vanadium spectra. Using Eq. IV.1 to describe the shape of the vanadium spectra, a χ^2 analysis was then made. Assuming trial values for the delayed fraction, η, and for the mean life of the 17 keV level, τ, a prompt component $(1-\eta)\ P_2(t)$ was added to the delayed component $\eta\ (P_1(t) * e^{-t/\tau})$, where the star refers to convolution, and this constructed spectrum was fitted to each vanadium time distribution. The constructed curve, normalized to the area of the experimental vanadium spectrum, was moved through in steps of 50 ps, the χ^2/n calculated for each position, and the minimum value chosen. This procedure was repeated for different values of η and τ, and constant χ^2/n contour plots, as illustrated in Fig. V.7 were then constructed for each vanadium run in order to determine the optimum η and τ and their 66% confidence limits. The optimum values for η from this analysis agreed with those obtained from the coincidence energy spectra.

The sum of vanadium runs 4, 5 and 6, and the corresponding mercury prompt, normalized to the area of the vanadium spectrum, is shown in Fig. V.8. Using

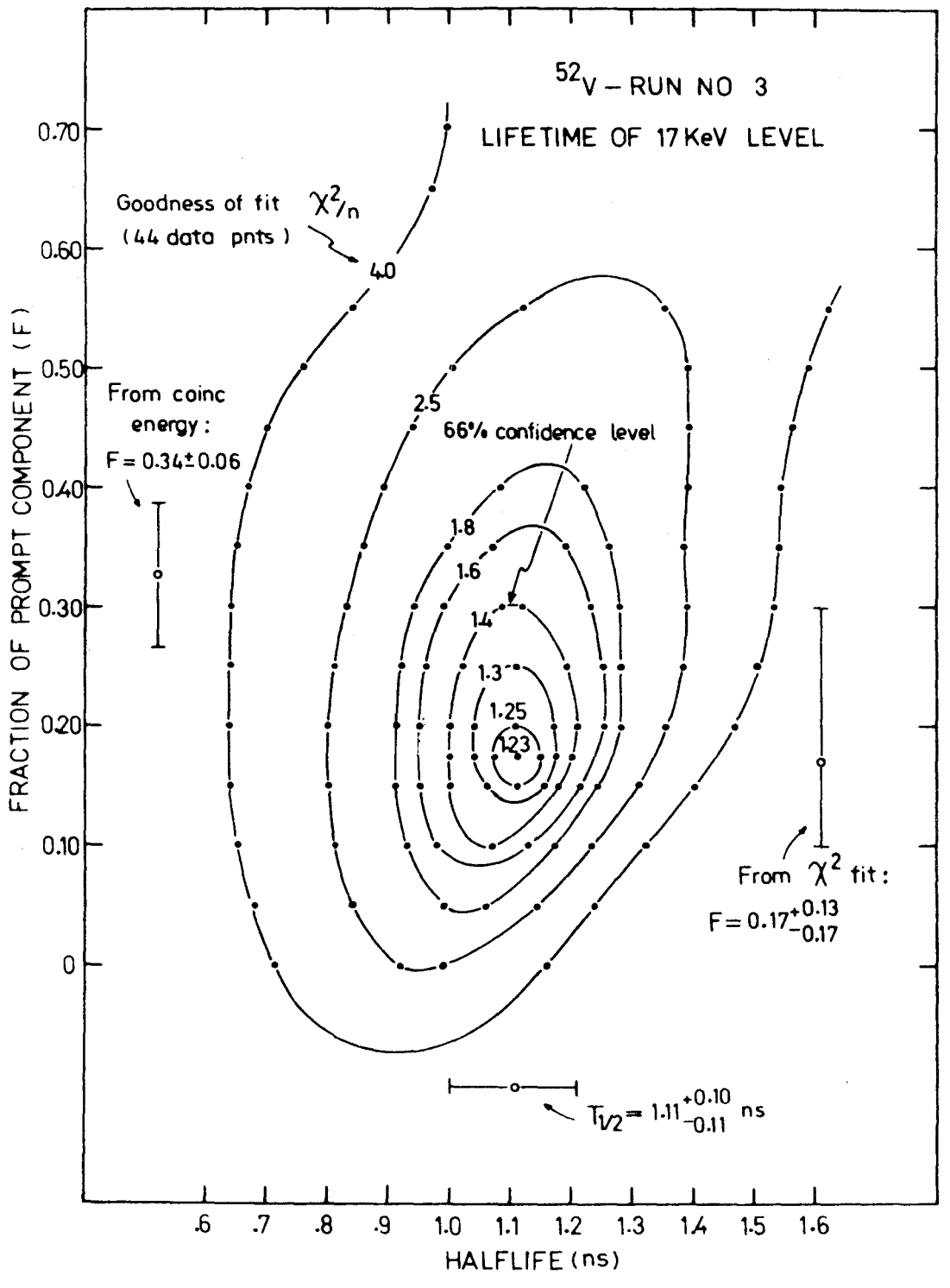

Fig. V.7 χ^2 analysis to measure the lifetime of the 17 keV level in ^{52}V

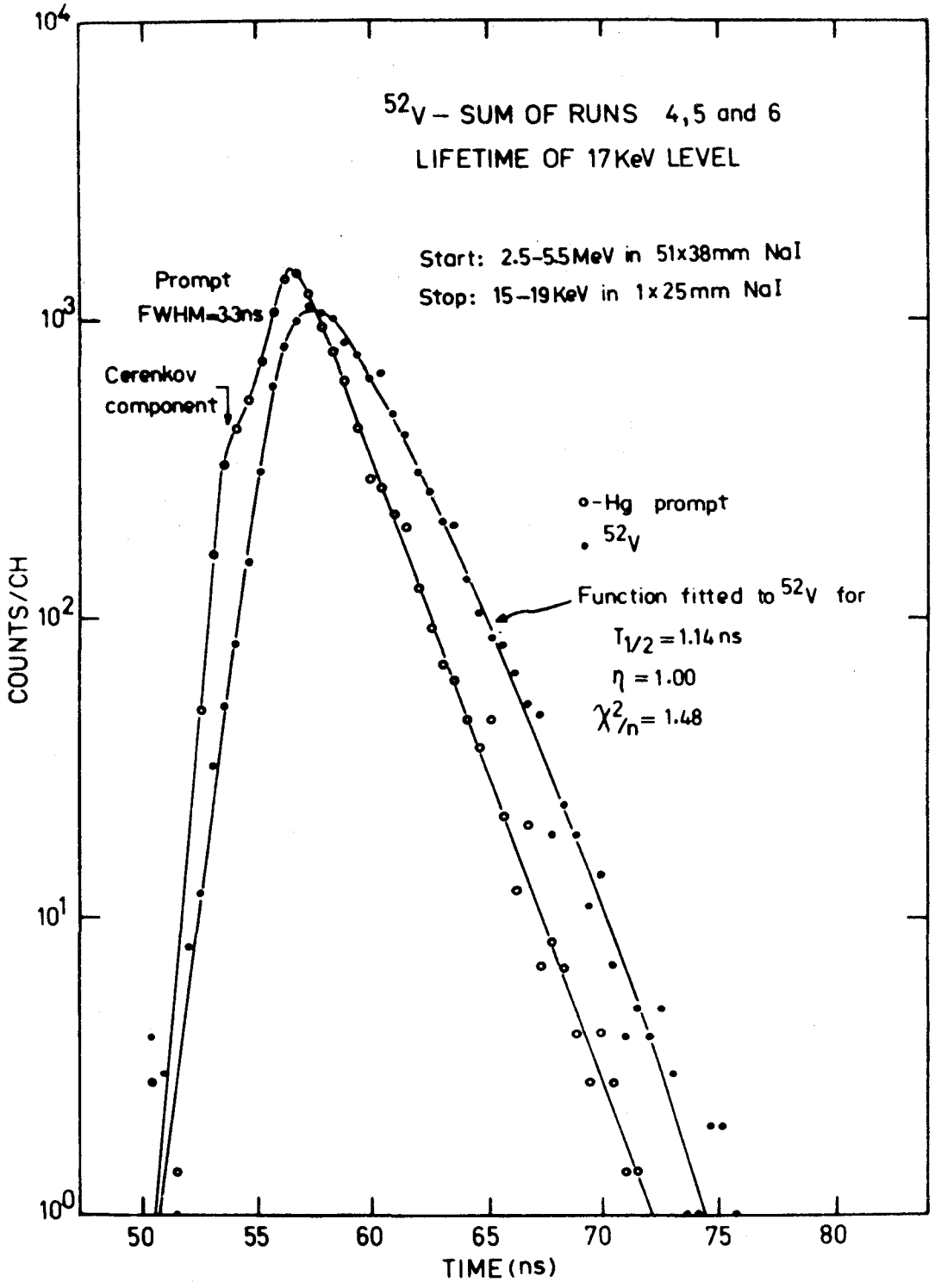

Fig. V.8 Measured time distribution for the 17 keV level in ^{52}V

this normalization it has been shown (NE50) that the prompt spectrum should intercept the delayed spectrum at its maximum value as is observed in these experimental results. The curve through the vanadium spectrum is the optimum fitted function while an arbitrary line has been drawn through the mercury prompt.

An additional analysis using Eq. IV.5 to IV.8 was made using the Čerenkov subtracted prompt response in order to give the 2nd, 3rd, 4th and 5th moment estimates for τ. The results for the 5 analysis procedures are given in table V.8 along with the start energy range for each run. The results, which have been averaged over both the different runs and the different analysis procedures, show no significant dependence on experimental conditions or on the method used to estimate τ.

In run number 3, the 125 keV γ ray, which directly populates the 17 keV level, was selected as the start, and this result rules out the possibility that the observed lifetime is due to a higher energy delayed level. The moment analysis was repeated using the prompt spectra containing the Čerenkov component and this complete neglect of the Čerenkov reduced the mean estimate for τ by 9%. For all runs, the prompt fraction, η, was between 0.2 and 0.35 so that the maximum prompt correction applied to any of the moment estimates was 5%. Based on the recognized systematic errors and on the

TABLE V.8

MEASURED VALUES FOR THE HALFLIFE OF THE 17 keV LEVEL IN ^{52}V

Run No.	Start Energy	χ^2 Fit	2^{nd} Mom	3^{rd} Mom	4^{th} Mom	5^{th} Mom	Mean
1	1-2 MeV (Plastic)	$0.70^{+0.13}_{-0.19}$	0.86 ± 0.12	1.07 ± 0.18	0.93	1.00	0.91
2	1.5-3.0 MeV (Plastic)	$0.88^{+0.36}_{-0.32}$	1.25 ± 0.12	1.00 ± 0.26	1.06	0.86	1.01
3	125 keV (NaI)	$1.11^{+0.10}_{-0.11}$	1.18 ± 0.07	0.97 ± 0.19	1.08	0.93	1.05
4	2.5-5.5 MeV (NaI)	1.01±0.13	1.06 ± 0.09	0.98 ± 0.17	1.02	0.97	1.01
5	2.5-5.5 MeV (NaI)	$1.10^{+0.11}_{-0.09}$	1.21 ± 0.07	1.12 ± 0.15	1.17	1.10	1.14
6	2.5-5.5 MeV (NaI)	$1.18^{+0.18}_{-0.22}$	1.23 ± 0.06	1.13 ± 0.14	1.20	1.18	1.14
Unweighted Mean Runs 1-6		1.00±0.08	1.13 ± 0.04	1.05 ± 0.08	1.08	1.01	

distribution in the individual results, a 20% error was assigned to the **final** result:

$$T_{1/2} = 1.08 \pm 0.22 \text{ ns}$$

H. Conversion Coefficient of the 17.2 keV Level in ^{52}V

The conversion coefficient for the 17.2 keV level was measured using the measured intensity of the 17 keV γ-ray, I_{17}, and the total intensity populating the state, I_p. The absolute population intensity $I_p = 16.7 \pm 2.6$ per 100 neutron captures was taken from the decay scheme of Archer and Kennett (AR57). The γ ray intensity, I_{17}, was experimentally determined by acquiring a NaI singles spectrum which included both the 17 keV line and a second line at 125 keV from ^{52}V with a measured absolute intensity, $I_{125} = 19.7 \pm 3.0$ per 100 neutron captures. The relative detector efficiency at 17 keV and 125 keV was then experimentally measured to give I_{17}.

The 17 keV conversion coefficient is defined as

$$\alpha_{17} = \frac{\text{decay rate by electron emission}}{\text{decay rate by } \gamma\text{-ray emission}}$$

$$= \frac{I_p}{I_{17}} - 1$$

Expressing I_{17} in terms of experimentally measurable quantities:

$$\alpha_{17} = \frac{I_p}{I_{125}} \cdot \frac{\varepsilon_{17}(SA)}{\varepsilon_{125}(SA)} \cdot \frac{\varepsilon_{17}(D)}{\varepsilon_{125}(D)} \cdot \frac{N_{125}}{N_{17}} - 1$$

where $\varepsilon(SA)$ = self absorption factor in vanadium target

$\varepsilon(D)$ = efficiency of detector and shielding arrangement

N = photopeak counting rate

and the subscripts refer to the 17 keV or 125 keV γ-rays.

The NaI detector and shielding arrangement was the same as that used for the lifetime measurement. In order to minimize self-absorption in the source, a **0.001"** thick vanadium foil inclined at an angle of 20° with respect to the plane of the detector was used. With this geometry the self absorption correction

$$\frac{\varepsilon_{17}(SA)}{\varepsilon_{125}(SA)} = 0.642 \pm 0.060$$

was calculated using the attenuation coefficients given by Storm et al (ST57). The γ-ray singles spectrum was similar to that obtained by White et al (WH65) including the line at 30 keV which can be attributed to the 30 keV level in ^{128}I excited by thermal neutron capture in the NaI detector. A ^{57}Co source, which emits 14 keV, 121 keV and 136 keV γ-rays, was used to determine the relative detector-shielding efficiency at 14 keV and 125 keV. The centre of gravity of the 121 keV and 136

keV γ-rays is close to 125 keV and the ratio of this photopeak area (excluding the iodine K-escape peak), to the 14 keV photopeak area, yielded the ratio:

$$\frac{\varepsilon_{14}(D)}{\varepsilon_{125}(D)} = 1.87 \pm 0.16$$

The efficiency, $\varepsilon_{14}(D)$ was extrapolated to 17 keV using the theoretical absorption coefficients:

$$\frac{\varepsilon_{17}(D)}{\varepsilon_{125}(D)} = 2.14 \pm 0.20$$

in order to calculate the 17 keV conversion coefficient:

$$\alpha_{17} = 4.6 \pm 1.8$$

I. Lifetimes of the 26 keV and 110 keV Levels in ^{56}Mn

1. Introduction

The lifetime of the 26 keV level in ^{56}Mn populated by thermal neutron capture has been measured by D'Angelo (AN60), $T_{1/2} = 10.7^{+2}_{-3}$ ns, and by Du Toit and Bollinger (TO61), $T_{1/2} = 11.4^{+2}_{-3}$ ns. In an attempt to eliminate a systematic effect and to reduce the rather large error, the measurement has been repeated here.

The low energy decay scheme for ^{56}Mn following thermal neutron capture as taken from (HU66, CO68, ME70) is shown in Fig. V.9. The intensities I_1 and I_2 represent the sum of transitions from all higher levels. In the two previous 26 keV halflife measurements, the Compton from high energy γ-rays, i.e. I_1 and I_2, was used to provide the start signal. When I_1 or the 84 keV γ-ray are used as the start signal and the 26 keV γ-ray as the stop, the start-stop time distribution will correctly display the exponential decay of the 26 keV level:

$$X_1(t) = \frac{1}{\tau_{26}} e^{-t/\tau_{26}}$$

However if I_2 is used as the start, an extra delay will arise due to the 110 keV lifetime and the 26 keV time distribution will display a "growing-in" shape:

$$X_2(t) = \frac{1}{\tau_{26}} \left(1 + \frac{\tau_{110}}{\tau_{26}}\right) \left(e^{-t/\tau_{26}}\right) \left(1-e^{-t/\tau_{110}}\right)$$

where τ_{26} and τ_{110} are the mean lives of the 26 and 110 keV levels. Thus for a high energy start window, the observed time distribution for the 26 keV γ-ray, X(t), will be a sum of $X_1(t)$, $X_2(t)$ and a prompt component, convolved with the system response function P(t):

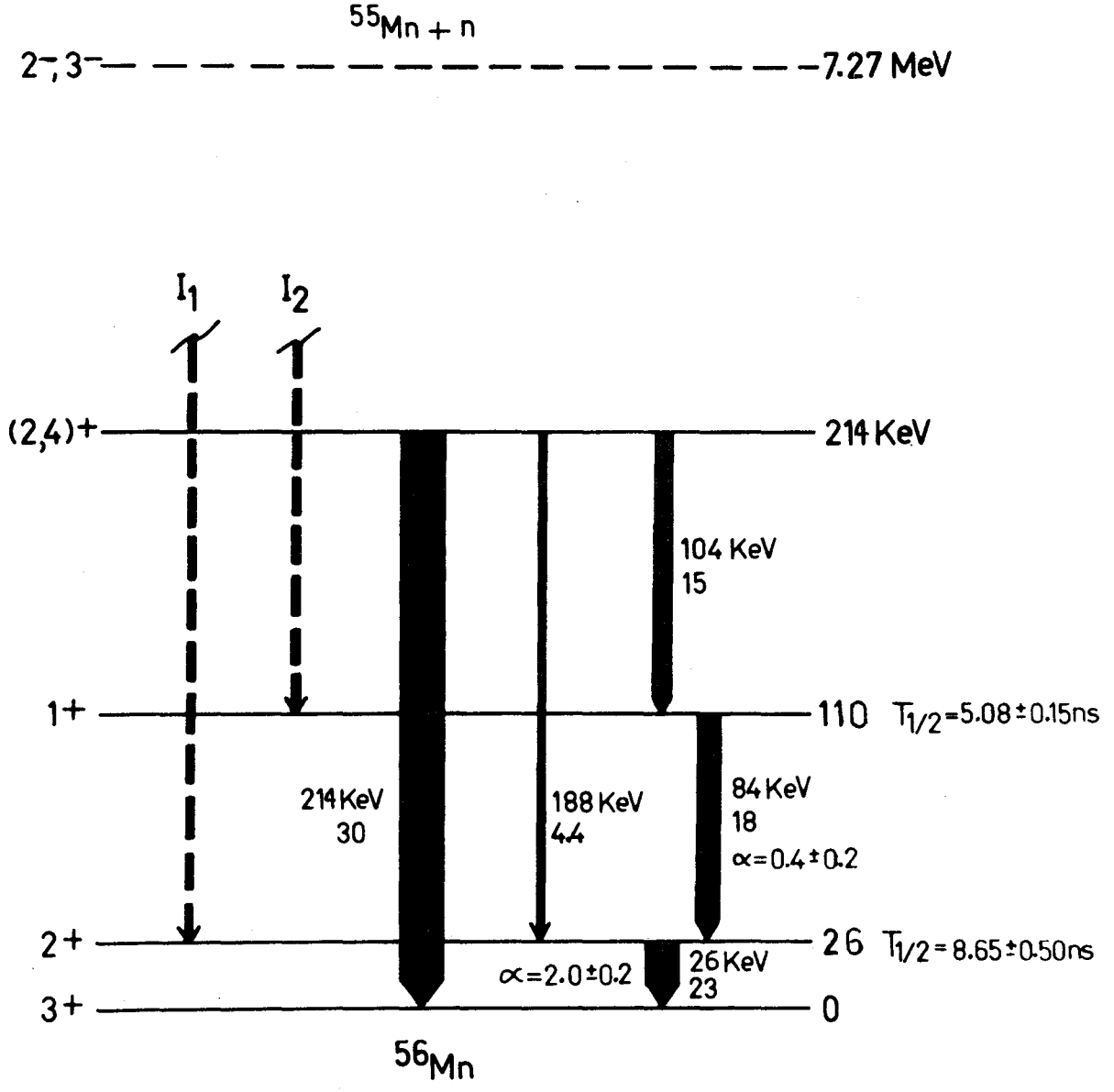

Fig. V.9 Low energy decay scheme of ^{56}Mn following thermal neutron capture

$$X(t) = \int_0^\infty \{P(t-t')\} \{(1-\eta)\,\delta(t') + \eta\,(\frac{1}{\tau_{26}}\, e^{-t'/\tau_{26}})$$

$$(1+\beta\,\frac{\tau_{110}}{\tau_{26}} - \beta\,[1 + \frac{\tau_{110}}{\tau_{26}}]\, e^{-t'/\tau_{110}})\}\, dt' \qquad V.1$$

where η is the fractional intensity of the delayed component and β is the fraction of the time that the 26 keV level is fed through the 110 keV level.

2. Experimental

The slope measurements of the lifetimes of the 26 keV and 110 keV levels in ^{56}Mn populated by thermal neutron capture in natural manganese were made using the basic fast-slow delayed coincidence system shown in Fig. II.2. Two measurements of the 110 keV lifetime using a NaI start detector (84 keV window) were performed along with seven 26 keV lifetime measurements using either a NaI start detector (84 keV window) or a Naton 136 plastic start detector (1-2 MeV window). For 26 keV runs 1 and 2, the start SCA selected the 84 keV photopeak detected in a 6 mm x 46 mm NaI mounted on an RCA 8575 and the stop SCA was set on the 26 keV photopeak detected in a 1 mm x 46 mm NaI mounted on an RCA 8550. For runs 3 and 4 an additional SCA was set on the 104 keV photopeak and the TAC signal routed to

two different groups in the analyser memory depending on which stop energy condition was satisfied using the arrangement shown in Fig. V.10. In this way the 26 keV time distribution was stored in one group and the time distribution for the 110 keV level (reversed in time) stored in the other. Runs 5, 6 and 7 were obtained using a 25.4 mm x 127 mm Naton 136 plastic start detector mounted on an XP-1040 and the stop energy range from 2 to 60 keV, as detected in a 1 mm x 25.4 mm NaI was stored in the energy dimension of a 2 parameter energy-time array.

3. Analysis and Results

The slopes of the 9 time spectra were measured and the halflife results, their statistical uncertainty and the goodness of fit criterion χ^2/n are given in table V.9. For the 3 high energy start runs, the fitting region was limited to late enough times so that the "growing-in" shape had turned to the pure 26 keV exponential decay as determined from the analysis given below. The errors in the mean values: 26 keV level, $T_{1/2} = 8.59 \pm 0.50$ ns and 110 keV level, $T_{1/2} = 5.08 \pm 0.15$ ns have been increased from the statistical estimate to include possible systematic affects.

To examine the influence of the "growing-in"

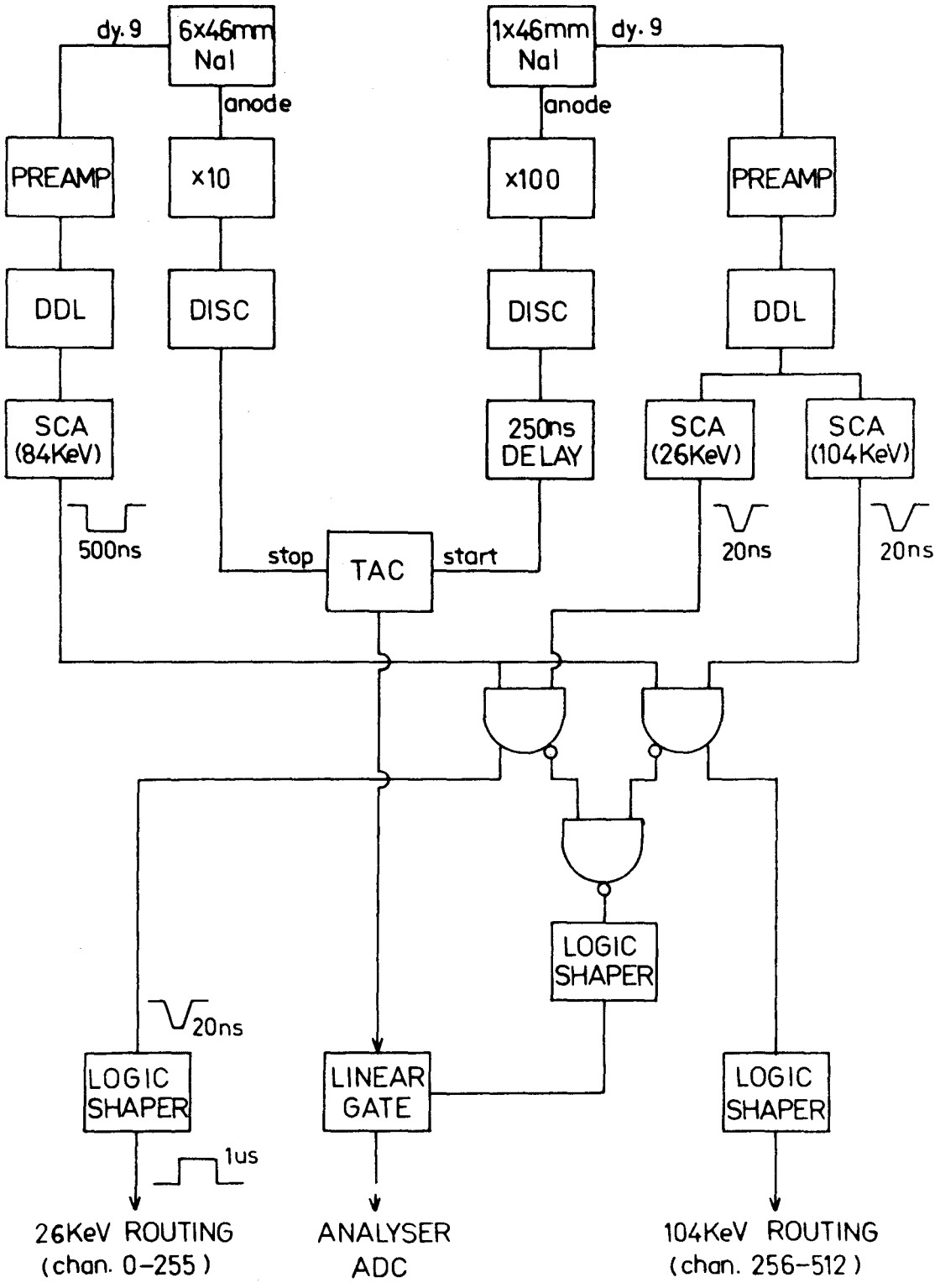

Fig. V.10 Block diagram of the ^{56}Mn routing experiment

TABLE V.9

^{56}Mn 110 keV LIFETIME

Run No.	Start Energy	χ^2/n	$T_{1/2}$(ns)	
1(b)	80-90 keV	1.09	5.06 ± 0.04	Mean = 5.08 ± 0.03
2(b)	80-90 keV	0.85	5.10 ± 0.04	

^{56}Mn 26 keV LIFETIME

Run No.	Start Energy	χ^2/n	$T_{1/2}$(ns)	
1(a)	80-90 keV	0.76	8.74 ± .15	Mean = 8.69 ± .05 ns
2(a)	80-90 keV	0.62	8.33 ± .07	
3	80-90 keV	0.80	8.79 ± .11	
4	80-90 keV	0.75	8.87 ± .27	
5	1-2 MeV	1.00	8.67 ± .20	Mean = 8.59 ± .06 ns
6	1-2 MeV	1.19	8.53 ± .11	
7	1-2 MeV	1.03	8.56 ± .11	
		Mean	8.65 ± .03 ns	

distribution on the measured slope and to determine the fitting region for the high energy start runs, theoretical curves were calculated and fitted to the experimental time spectra. Trial values for η and β were chosen and X(t) as given in Eq. V.1 constructed using the experimental prompt response function. The mean halflives for the 26 and 110 keV levels were determined from the low energy start runs and were held fixed during the fit. The constructed X(t), normalized to the area of the experimental time spectrum Y(t), was moved through X(t) in steps of 100 ps, the goodness of fit criterion, χ^2/n, calculated for each position, and the lowest value for χ^2/n chosen. This procedure was repeated for different values of η and β and the results were represented as a contour plot for constant χ^2/n as illustrated in Fig. V.11. The 3 high energy start runs were analyzed in this way and the η and β values which minimized the χ^2/n along with their standard deviations were determined from the contour plot for each case. The η values obtained from this analysis agreed within statistical error with those obtained from the peak-to-background ratio in the coincidence energy spectrum, and the values for β were consistent with the result calculated using the 26 and 84 keV γ-ray intensities and conversion coefficients (ES60, HU65):

$$\beta = 0.57$$

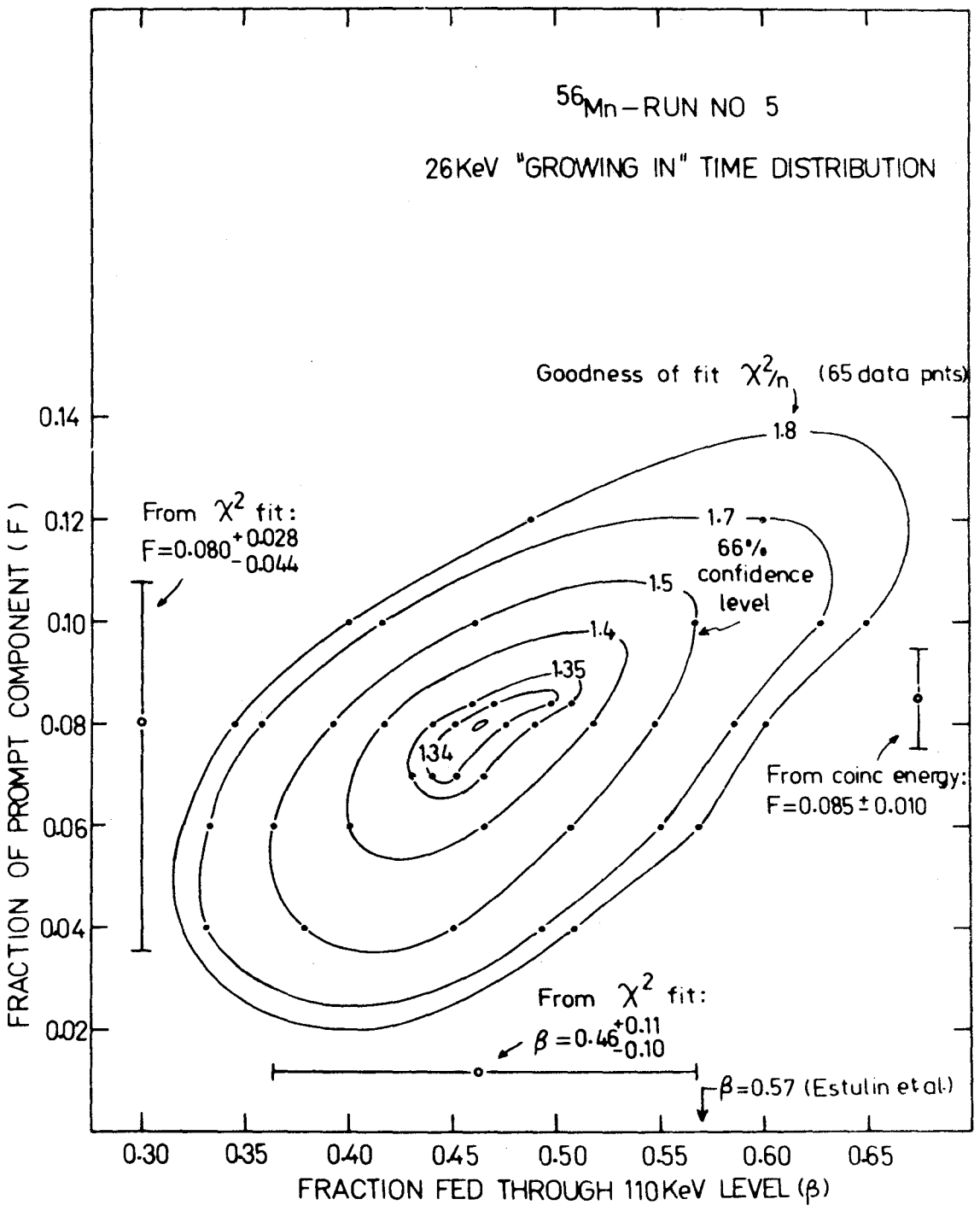

Fig. V.11 χ^2 analysis of the time distribution of the 26 keV level in ^{56}Mn

As observed in Fig. V.12 fitting the halflife over a range determined only by the effect of the prompt would lead to a significant overestimate for the halflife. The prompt response for the two previous lifetime measurements is poorer than that obtained here making the extended rounding off at the top of the time distribution due to the "growing-in" effect more difficult to recognize. It then seems probable that the higher halflife values obtained by D'Angelo and by Du Toit and Bollinger, as compared to the value obtained here, could be attributed to neglecting the true "growing-in" shape of the time spectra.

J. Summary of Experimental Results

The theoretical M1 and E2 total conversion coefficients, obtained by extrapolating the table of Hager and Seltzer (HA69), were used along with the experimental conversion coefficients, in order to determine the multipolarity of each γ-ray, and the results are listed in Table V.10. Using these mixing ratios and the experimental conversion coefficients, the experimental halflife results, which are summarized in Table V.11, were corrected for conversion and the partial M1 and E2 halflives calculated:

$$T_{1/2}(M1) = T_{1/2}(\text{exp}) \; [1+\alpha_{exp}] \; [1 + \frac{I_{E2}}{I_{M1}}]$$

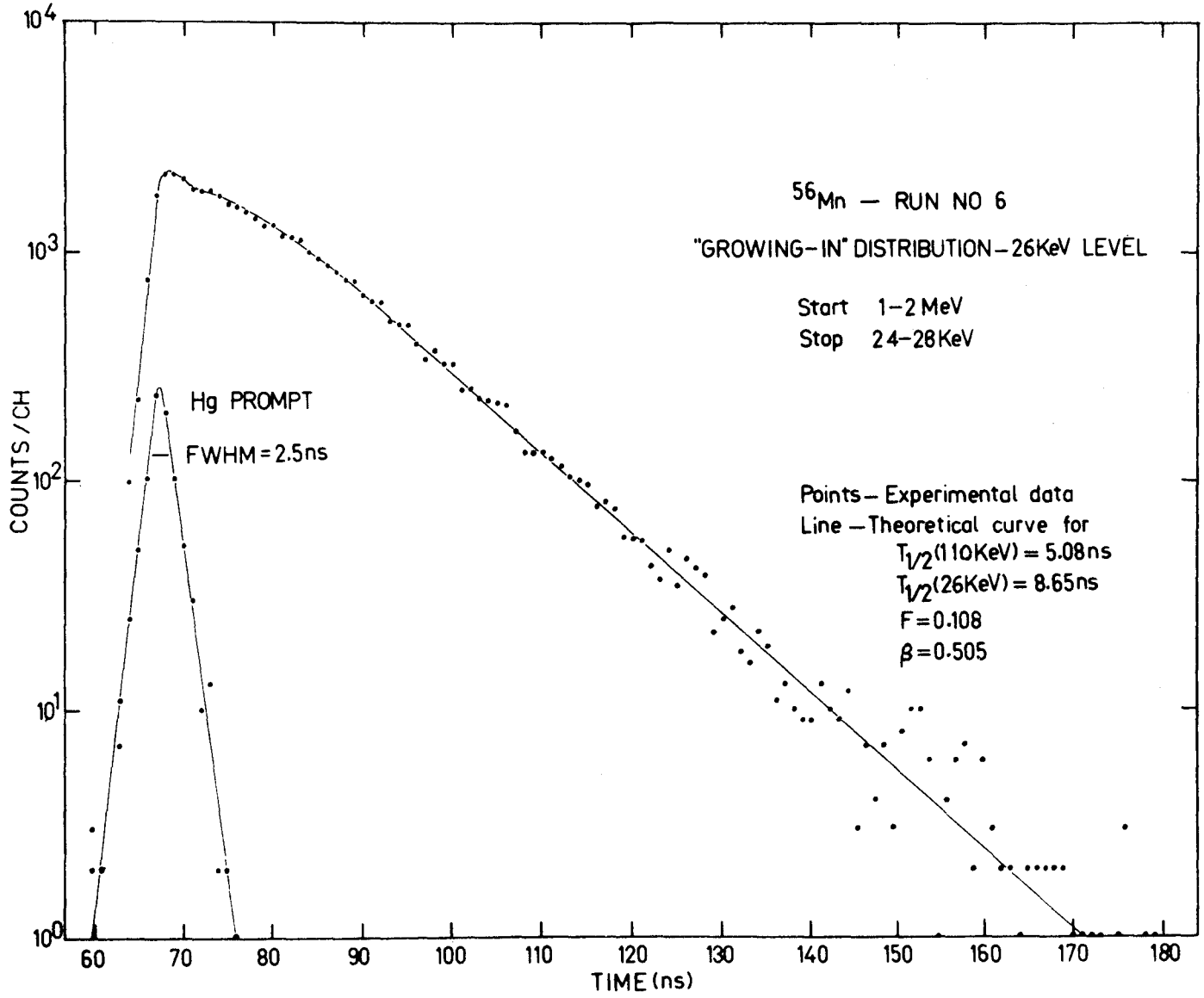

Fig. V.12 Measured time distribution for the 26 keV level in ^{56}Mn

TABLE V.10

M1 - E2 γ-RAY MIXING RATIOS

Nucleus	γ-ray Energy (keV)	α(Exp)	α_{M1}(Theory)	α_{E2}(Theory)	Assignment
^{28}Al	31.2	0.03 ± 0.07	0.052	11	M1
^{32}P	77	-	0.0065	0.42	M1
^{40}K	29.4	-	0.28	29	M1
^{46}Sc	52	4	0.11	5.5	E2
^{52}V	17.0	4.6 ± 1.8	2.0	26	90% M1, 10% E2
^{56}Mn	26.6	2.0 ± 0.2	1.3	70	99% M1, 1% E2
	85	0.4 ± 0.2	0.04	0.82	55% M1, 45% E2

$$T_{1/2}(E2) = T_{1/2}(exp)\ [1+\alpha_{exp}]\ [1 + \frac{I_{M1}}{E_{E2}}]$$

where I_{M1} and I_{E2} refer to the relative intensities of the M1 and E2 components. The B(M1) and B(E2) reduced transition probabilities, expressed in Weisskopf units, are also given in Table V.11. For cases where the experimental conversion coefficient has not been measured, the transition was assumed to be pure M1 and the theoretical M1 conversion coefficient was used.

TABLE V.11

SUMMARY OF EXPERIMENTAL HALFLIFE RESULTS

Nucleus	γ-Ray Energy (keV)	$T_{1/2}$(Exp)	$T_{1/2}$(M1)	$T_{1/2}$(E2)	B(M1)(w.u)	B(E2)(w.u)
^{28}Al	31.2	2.15 ± 0.06 ns	2.26 ns	--	0.29	--
^{32}P	77	0.253± 0.025 ns	0.25 ns	--	0.19	--
^{40}K	29.4	4.26 ± 0.08 ns	5.4 ns	--	0.16	--
^{46}Sc	52	9.62 ± 0.50 μs	--	48 μs	--	325
^{52}V	17.0	1.08 ± 0.22 ns	6.8±2.5 ns	--	0.8 ± 0.3	--
^{56}Mn	26.6	8.70 ± 0.50 ns	26 ns	26 μs	0.054	1700
	85	5.08 ± 0.20 ns	13 ns	15 μs	0.0028	660

CHAPTER VI

THEORETICAL TRANSITION PROBABILITY

A. Transition Probability

According to time dependent perterbation theory, the quantum mechanical transition probability per unit time for a transition from an initial state $\langle i|$ to a final state $|f\rangle$ is:

$$T_{i\to f} = \frac{2\pi}{\hbar} \rho_f \; |\langle f|H|i\rangle|^2 \qquad \text{VI.1}$$

where H is the interaction Hamiltonian and ρ_f is the density of final states. It can be shown (PR62, EN66), that for a nucleus changing from an initial state $\langle J_i|$ to final state $|J_f\rangle$ by the magnetic interaction M, the probability for emission of a γ-ray of energy E_γ and angular momentum λ is:

$$T_{i\to f} = \frac{2\ (\lambda+1)\ \mu_o}{\lambda[(2\lambda+1)!!]^2\ \hbar} \left[\frac{E_\gamma}{\hbar c}\right]^{2\lambda+1} B(M\lambda) \qquad \text{VI.2}$$

where the reduced transition probability, $B(\sigma\lambda)$, is

given by

$$B(M\lambda) = \frac{1}{2Ji+1} \sum_{M_i, M_f} |\langle J_f M_f | M_\lambda^\mu | J_i M_i \rangle|^2 \qquad \text{VI.3}$$

If the wave functions describing the initial and final states are known, Eq. VI.2 and VI.3 then allow a direct calculation of the transition probability. Because of the sensitivity to configuration mixing and collective effects, the use of model states in calculating the transition probability has generally produced a poor agreement with experimental results. A useful order of magnitude estimate for the transition probability has been obtained by Weisskopf (WE51) and by Moszkowski (MO53). For these approximations it was assumed that a single proton changes from an orbit with angular momentum λ to an orbit with 0 angular momentum and that the radial part of the wave functions are constant inside the nucleus and 0 outside. For M1 transitions, the Weisskopf estimate for the halflife is (PR62):

$$T_{1/2}(M1) = \frac{2.2}{E_\gamma^3(keV)} \times 10^{-5} \text{ sec.}$$

B. Derivation of Inter-Multiplet M1 Transition Probability

1. Introduction

The states of an odd-odd nucleus, denoted by $|j_n\ j_p\ JM\rangle$, are formed by coupling the proton state, $|j_p\ m_p\rangle$, to the neutron state $|j_n\ m_n\rangle$:

$$|j_n\ j_p\ JM\rangle = \Sigma\ (j_n\ j_p\ m_n\ m_p|JM)\ |j_n\ m_n\rangle|j_p\ m_p\rangle \qquad \text{VI.4}$$

where the Clebsh-Gordon coefficient, $(j_n\ j_p\ m_n\ m_p|JM)$ and the notation that will be used here, is defined in (PR62). For a given neutron and proton configuration, a number of different states, each representing a different coupling of j_n and j_p, can be formed. The members of this multiplet will have integral spins, J, ranging from $|j_n - j_p|$ to $j_n + j_p$ in unit steps, and each state will lie at a different excitation energy.

Using Eq. VI.2 and VI.3, and the states described by Eq. VI.4, an expression will be derived for the M1 transition probability between low energy members of the ground state multiplet, i.e. for transitions of the type:

$$|j_n\ j_p\ J_i\ M_i\rangle \rightarrow |j_n\ j_p\ J_f\ M_f\rangle$$

which require only a recoupling of the neutron and

proton spins.

2. Reduction of B(Ml)

The intermultiplet B(Ml) is given by

$$B(Ml) = \frac{1}{2J_i+1} \sum_{M_i M_f} |\langle J_f M_f | M'_\mu | J_i M_i \rangle|^2$$

Using the Wigner-Eckhart theorem (PR62):

$$\langle J_f M_f | M'_\mu | J_i M_i \rangle = (J_i \; 1 \; M_i \; \mu | J_f M_f)(J_f || M' || J_i)$$

this can be expressed in terms of an M independent matrix element:

$$B(Ml) = \frac{(J_f || M' || J_i)^2}{2J_i+1} \sum_{M_i M_f} (J_i 1 \; M_i \; \mu | J_f M_f)^* (J_i \; 1 \; M_i \; \mu | J_f M_f)$$

VI.5

The Clebsh-Gordon symmetry condition (PR62):

$$(J_i \; 1 \; M_i \; \mu | J_f \; M_f) = (-1)^{1-J_f-M_i} \left[\frac{2J_f+1}{3}\right]^{1/2} (J_i J_f - M_i M_f | 1\mu)$$

allows the double sum in VI.5 to be expressed in a closed form:

$$\sum_{M_i M_f} (J_i \; 1 \; M_i \; \mu | J_f M_f)^* (J_i \; 1 \; M_i \; u | J_f M_f)$$

$$= \frac{2J_f + 1}{3} \sum_{M_i M_f} (J_i J_f - M_i M_f | 1 \; \mu)^2$$

$$= \frac{2J_f + 1}{3}$$

so that:

$$B(M1) = \frac{2J_f + 1}{3(2J_i + 1)} \cdot (J_f || M' || J_i)^2$$

3. Reduction of Matrix Element

The magnetic dipole operator can be decomposed into proton and neutron operators:

$$M'_\mu = M'_\mu(n) + M'_\mu(p)$$

Consider a typical element of the neutron operator:

$$N = (j_p \; j_n \; J_f \; M_f | M'_\mu(n) | j_p \; j_n \; J_i \; M_i)$$

$$N = \sum_{m'_p m_p} (j_p \; j_n \; m'_p \; m'_n | J_f M_f)^* (j_p \; j_n \; m_p \; m_n | J_i M_i) \; X$$

$$\langle j_p \; m'_p | j_p \; m_p \rangle \; \langle j_n \; m'_n | M'_\mu | j_n \; m_n \rangle$$

$$N = \sum_{m_p} (j_p\ j_n\ m_p\ m_n' | J_f M_f)^* (j_p\ j_n\ m_p\ m_n | J_i M_i)\ x$$

$$\langle j_n\ m_n' | M_\mu' | j_n\ m_n \rangle$$

From the Wigner-Eckhart theorem:

$$(j_n\ m_n' | M_\mu' | j_n\ m_n) = (j_n\ 1\ m_n\ \mu | j_n\ m_n')(j_n || M' || j_n)$$

which gives for the matrix element:

$$N = (j_n || M' || j_n) \sum_{m_p} (j_p\ j_n\ m_p\ m_n' | J_f M_f)^*\ x$$

$$(j_p\ j_n\ m_p\ m_n | J_i M_i)\ (j_n\ 1\ m_n\ \mu | j_n\ m_n') \qquad \text{VI.6}$$

Thus, since the inter-multiplet transition involves a recoupling of spins only, the neutron and proton matrix elements are diagonal and therefore can be expressed in terms of the static magnetic moments.

4. Relation of Matrix Element to Static Magnetic Moment

The static neutron magnetic dipole moment is defined as:

$$u_n = (j_n\ j_n|M'_o|j_n\ j_n)$$

$$= (j_n\ 1\ j_n\ 0|j_n\ j_n)\ (j_n||M'||j_n) \qquad \text{VI.7}$$

so that

$$(j_n||M'||j_n) = \frac{u_n}{(j_n\ 1\ j_n\ 0|j_n\ j_n)}$$

The neutron matrix element, equation Vl.6, can then be expressed in terms of the static magnetic dipole moment:

$$N = \frac{u_n}{(j_n\ 1\ j_n\ 0|j_n j_n)} \sum_{m_p} (j_p\ j_n\ m_p\ m'_n|J_f M_f)^*\ x$$

$$(j_p\ j_n\ m_p\ m_n|J_i M_i)\ (j_n\ 1\ m_n\ \mu|j_n\ m'_n)$$

and by symmetry, a similar expression follows for the proton matrix element P.

The total matrix element is then

$$(j_p\ j_n\ J_f\ M_f|M'_u|j_p\ j_n\ J_i\ M_i) = N + P$$

$$= \frac{\mu_n}{(j_n 1 j_n\ 0|j_n\ j_n)} \sum_{m_p} (j_p\ j_n\ m_p\ m'_n|J_f M_f)^*\ x$$

$$(j_p\ j_n\ m_p\ m_n|J_iM_i)\ (j_n\ 1\ m_n\ \mu|j_n\ m_n')$$

$$+\ \frac{u_p}{(j_p 1 j_p 0|j_p\ j_p)}\ \sum_{m_n}(j_p\ j_n\ m_p'\ m_n|J_fM_f)^*\ x$$

$$(j_p\ j_n\ m_p\ m_n|J_iM_i)\ (j_p\ 1\ m_p\ \mu\ |\ j_p\ m_p') \qquad \text{VI.8}$$

5. Expression for the Inter-Multiplet Halflife

Taking the typical matrix element: $M_i = M_f = 0$, so that $\mu = 0$, $m_n'=m_n=-m_p$ and $m_p=m_p'=-m_n$, and using the Wigner-Eckhart theorem:

$$(J_f||M'||J_i) = \frac{(J_f\ 0|M_o'|J_i 0)}{(J_i 1 0\ 0|J_f\ 0)}$$

$$= \frac{1}{(J_i 1 0 0|J_f 0)}\quad \frac{u_n}{(j_n 1 j_n 0|j_n j_n)}\ \sum_{m_p}(j_p j_n m_p -m_p|J_f 0)^*\ x$$

$$(j_p j_n m_p -m_p|J_i 0)(j_n\ 1\ -m_p\ 0|j_n -m_p)$$

$$+\ \frac{u_p}{(j_p 1 j_p\ 0|j_p j_p)}\ \sum_{m_n}(j_p\ j_n\ -m_n m_n|J_f\ 0)^*\ x$$

$$(j_p j_n\ -m_n m_n|J_i 0)(j_p 1\ -m_n\ 0|j_p -m_n) \qquad \text{VI.9}$$

$$B(M1) = \frac{2J_f+1}{3(2J_i+1)}\ \left|(J_f||M'||J_i)\right|^2\ x\ \frac{3}{4\pi} \qquad \text{VI.10}$$

The intermultiplet B(Ml) transition probability is then given by equations VI.9 and VI.10 in terms of the magnetic moment and spin of the odd proton and neutron, and the initial and final spins of the nucleus. Since the static magnetic dipole moment is defined in terms of Legendre polynomials, P_λ, and the Ml transition probability in terms of spherical harmonic functions, Y_λ^μ, and since (e.g. ME61)

$$Y_1^0 = \sqrt{\frac{3}{4\pi}}\, P_1$$

the normalizing factor $\frac{3}{4\pi}$ has been included in Eq. VI.10.

For magnetic dipole transitions, Eq. VII.2 equals

$$T_{i\to f}(Ml) = \frac{4}{9}\,\frac{\mu_o}{\hbar^4 c^3}\, E_\gamma^3\, B(Ml)$$

which corresponds to a halflife

$$T_{1/2}(Ml) = \frac{.693}{T_{i\to f}}$$

$$T_{1/2}(Ml) = 3.93\,\frac{1}{E_\gamma^3\, B(Ml)} \times 10^{-5}\ \text{sec} \qquad \text{VI.11}$$

where B(Ml) is expressed in units of nuclear magnetons and is calculated using Eqs. VI.9 and VI.10, and E_γ is

in units of keV.

The basis of the approach is that rather than requiring the assumption of particular model states for the calculation of the matrix element, the ground state magnetic moments of the neighbouring odd-even and even-odd nuclei can be used for u_n and u_p. Quenching and collective effects which manifest themselves in the odd-A nuclei are then included in the matrix element. The main physical effects which are not accounted for are the residual neutron-proton interaction and the possible admixture of states from a nearby multiplet, i.e. from states which are present in the odd-odd nucleus but not in the odd-A cases. These effects are discussed in more detail in chapter VII.B.

C. Expression for the Magnetic Dipole Moment of the Odd-Odd Nucleus

This approach can be used to obtain an expression for the ground state static magnetic dipole moment (μ_{0-0}) of an odd-odd nucleus (with ground state spin J), in terms of the static moments of the corresponding odd-A nuclei. Taking the case M = J, the diagonal element of Eq. VI.8 (i.e. $J = J_i = J_f$) is then equal to the odd-odd magnetic moment. The calculation is performed by setting $M_i = M_f = J = J_i = J_f$ in Eq. VI.8 so that

$$\mu = 0$$

$$m_n = m_n' = J - m_p$$

$$m_p = m_p' = J - m_n$$

Eqs. VI.7 and VI.8 then give an expression for the ground state magnetic moment of the odd-odd nucleus:

$$\mu_{0-0} = (J\ J|M_o'|J\ J)$$

$$= \frac{\mu_n}{(j_n 1 j_n 0|j_n j_n)} \sum_{m_p} (j_p j_n\ m_p\ J-m_p|JJ)^2 (j_n 1 J-m_p\ 0|j_n J-m_p)$$

$$+ \frac{\mu_p}{(j_p 1 j_p 0|j_p j_p)} \sum_{m_n} (j_p j_n\ J-m_n m_n|JJ)^2 (j_p 1 J-m_n\ 0|j_p\ J-m_n) \qquad \text{VI.12}$$

CHAPTER VII

INTERPRETATION AND DISCUSSION OF RESULTS

A. Comparison of Experiment and Theory

Five low energy M1 transitions in the odd-odd nuclei ^{28}Al, ^{32}P, ^{40}K, ^{52}V and ^{56}Mn whose lifetimes were measured in this thesis are listed in table VII.1 along with two high energy transitions in ^{40}K which have been recently measured using the attenuated Doppler-shift method (SE70). Based on the assumed neutron and proton configurations, and the initial and final spins and parities of the odd-odd nuclei, (Fig. VII.1), these can be classified as transitions between members of the ground state multiplet. A survey over neighbouring regions of the periodic table indicated that these were the only inter-multiplet M1 transitions for which the experimental lifetime and magnetic moment information required for the theoretical B(M1) calculation is known. Since the 52 keV transition in ^{46}Sc is E2, the corresponding lifetime measurement reported in Chapter V has not been included in this analysis.

In Fig. VII.1, the low energy levels in the 5

TABLE VII.1

COMPARISON OF EXPERIMENTAL AND THEORETICAL RESULTS

Nucleus	Transition	B(M1) (w.u.)			Odd-Odd Static Gnd State μ(n.m.)		
		Experiment	Theory	Schmidt Limits	Experiment	Theory	Schmidt Limits
^{28}Al	31→0	0.34 ± 0.01	0.17	0.85	--	-0.56	-1.91
^{32}P	77→0	0.19 ± 0.02	0.056	0.39	-0.2523	0.53	0.94
^{40}K	29→0	0.160±0.003	0.049	0.037	-1.298	-1.46	-1.75
^{40}K	797→29	0.054±0.012	0.053	0.039			
^{40}K	885→0	0.019±0.004	0.024	0.018			
^{52}V	17→0	0.73 ± 0.28	0.32	0.86	--	0.00	0.00
^{56}Mn	26→0	0.045±0.003	0.038	0.030	3.218	0.091	0.63

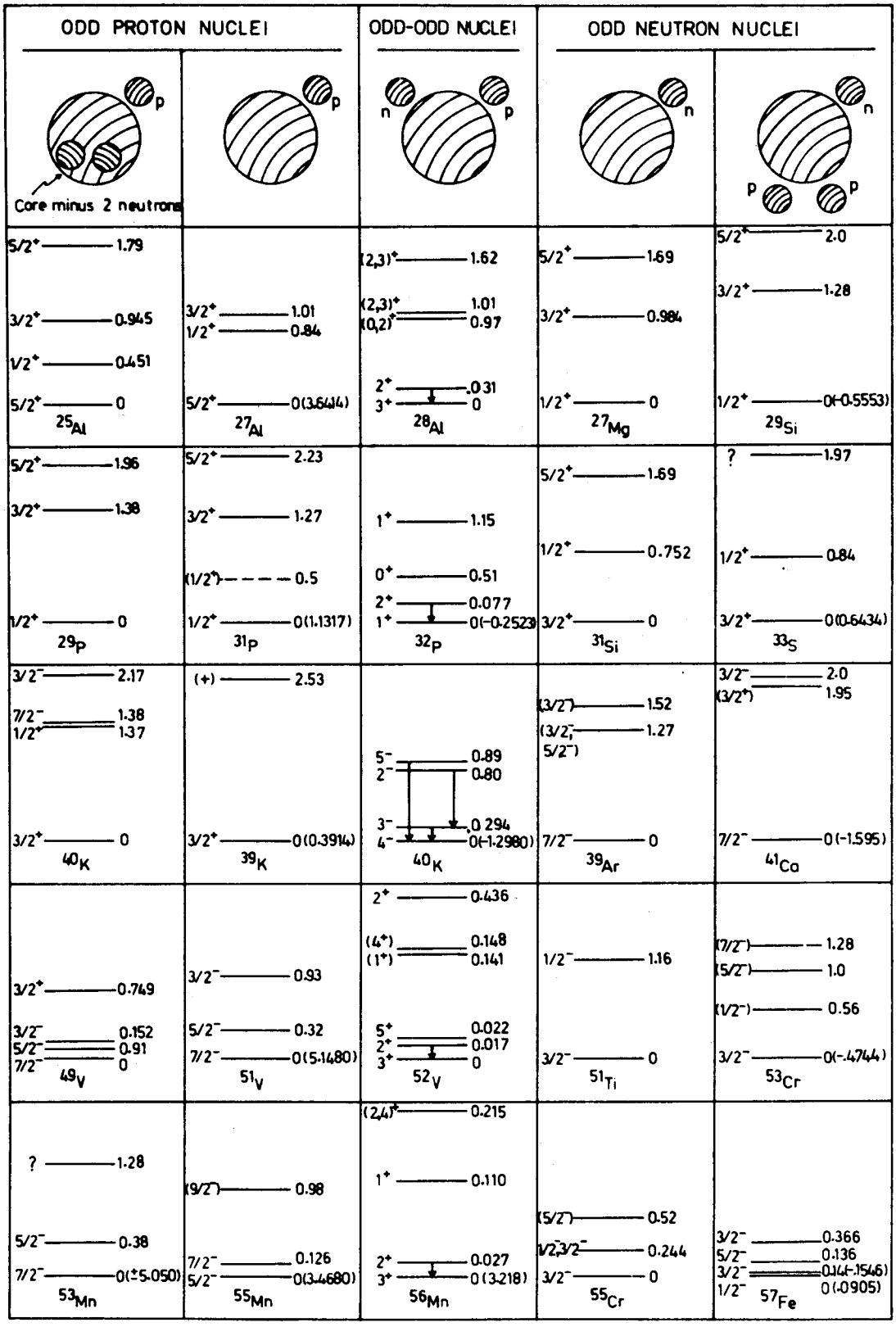

Fig. VII.1 Energy levels in the odd-odd and corresponding odd-A nuclei

odd-odd nuclei (core + neutron + proton), are shown along with the odd-A nuclei representing the 4 configurations:

core + proton - 2 neutrons

core + proton

core + neutron

core + neutron + 2 protons

which correspond to the cases about which the most experimental information is known. The seven inter-multiplet transitions are indicated by the arrows, and where known, the static magnetic dipole moment (in nuclear magnetons) is written in brackets to the right of the energy. In the odd-A nuclei corresponding to ^{28}Al, ^{32}P, ^{40}K and ^{52}V, it is evident that the states of the odd proton or neutron are only weakly dependent upon the filling of the shell of the other nucleon. The addition of 2 protons or the removal of 2 neutrons from the shell leaves the odd A ground states unchanged and in only one case, that of the ^{39}Ar-^{41}Ca pair, is the order of 2 excited levels below 2 MeV inverted. Since the ground state magnetic moments of the nuclei: core + neutron have in general not been measured, it then seems justified to use the ground state moments of the nuclei: core + neutron + 2 protons as μ_n in the B(M1) calculations. The odd proton magnetic moments, μ_p, were taken from the

core + proton nuclei.

In ^{56}Mn, there is ambiguity as to what shell model states to assign to the neutron and proton. Because of the proximity in energy, the $p_{3/2}$ and $p_{1/2}$ neutron states are possible and as can be seen from Fig. VI.1, the addition of 2 protons inverts the order of these 2 states. Similarly the order of the $(f^5_{7/2}, 7/2)$ and $(f^5_{7/2}, 5/2)$ proton states is inverted by the removal of 2 neutrons. The 2^+ (27 keV state) and 3^+ (ground state) members of the ground state multiplet can then be formed by 3 possible neutron-proton configurations:

1. $(p_{3/2})_n(f^5_{7/2},7/2)_p$ B(M1)=0.240w.u. μ(gnd)=0.000

2. $(p_{3/2})_n(f^5_{7/2},5/2)_p$ B(M1)=0.211w.u. μ(gnd)=-0.090

3. $(p_{1/2})_n(f^5_{7/2},5/2)_p$ B(M1)=0.038w.u. μ(gnd)=0.091

The theoretical B(M1) strength (in Weisskopf units) and odd-odd ground state magnetic dipole moment (in nuclear magnetons), were calculated for each configuration using Eqs. VI.9, VI.10 and VI.12. Assuming pure proton and neutron states, the best agreement with the experimental values:

$$B(M1)=0.045 \text{ w.u.} \quad \mu(gnd)=3.218 \text{ nm}$$

is then obtained for configuration 3.

The experimental and theoretical results for the 5 odd-odd ground state magnetic moments and for the 7 intermultiplet B(M1) transition strengths are listed in Table VII.2 and are plotted in Fig. VII.2. The experimental values for the reduced transition probability have been corrected for electron conversion and for the presence of any detected E2 mixture. The correlation coefficient (CR60, YO62) defined as

$$\rho = \frac{\sum_{i=1}^{N} (x_i - \bar{x})\,(Y_i - \bar{Y})}{\left[\sum_{i=1}^{N} (x_i - \bar{x})^2 \sum_{i=1}^{N} (Y_i - \bar{Y})^2 \right]^{1/2}}$$

where x_i and Y_i refer to the N pairs of experimental and theoretical B(M1) values, was calculated and the result

$$\rho = 0.980 \qquad \text{for } N = 7$$

indicates that there is a 99.95% probability that the theoretical results are correlated with experiment (i.e. there is an 0.05% probability for uncorrelated pairs exceeding this value of ρ). The use of the Schmidt limits for μ_n and μ_p (Fig. VII.3 and Table VII.1)

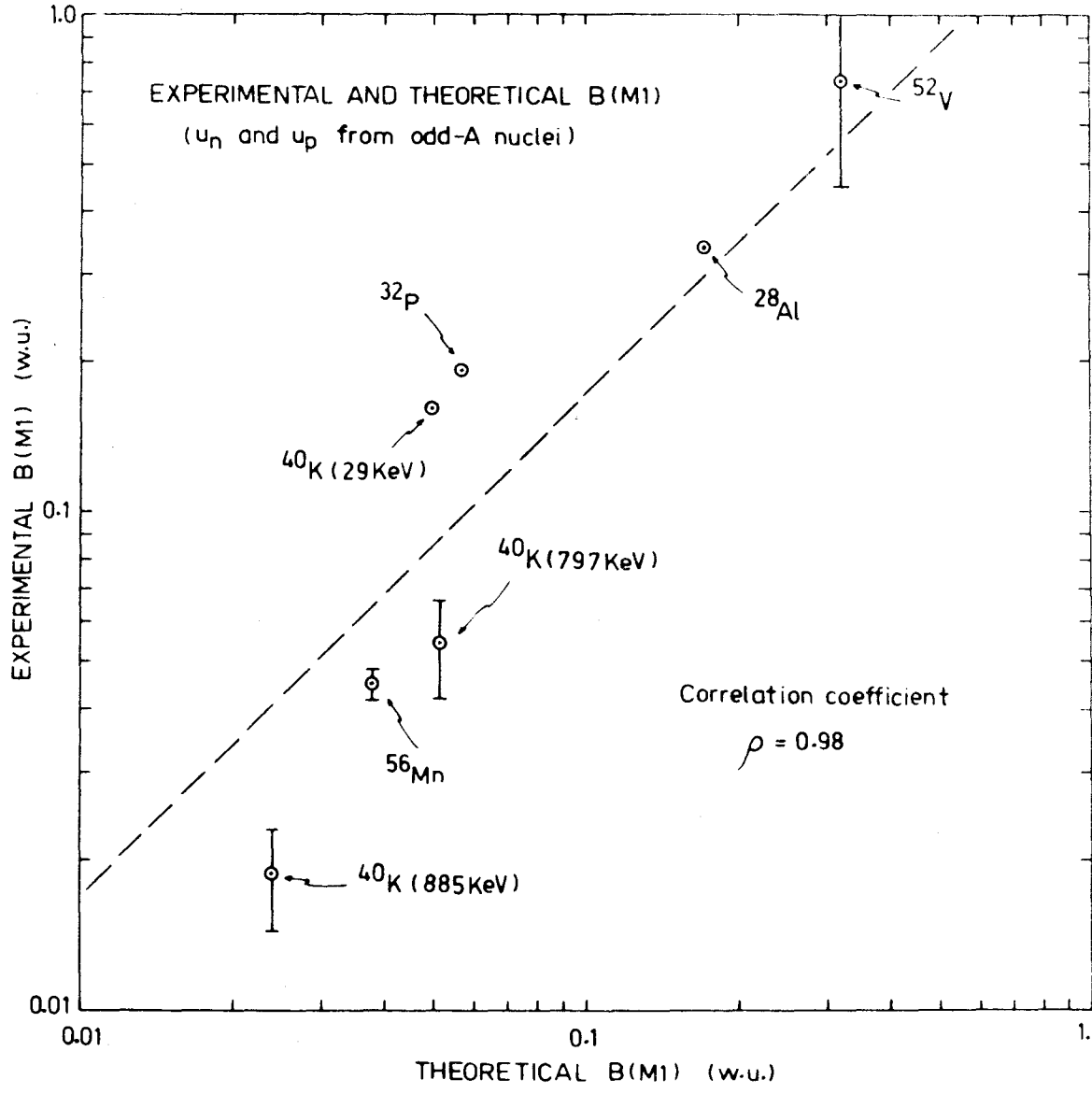

Fig. VII.2 Comparison of the experimental and theoretical B(Ml) strengths using μ_n and μ_p as obtained from the corresponding odd-A nuclei

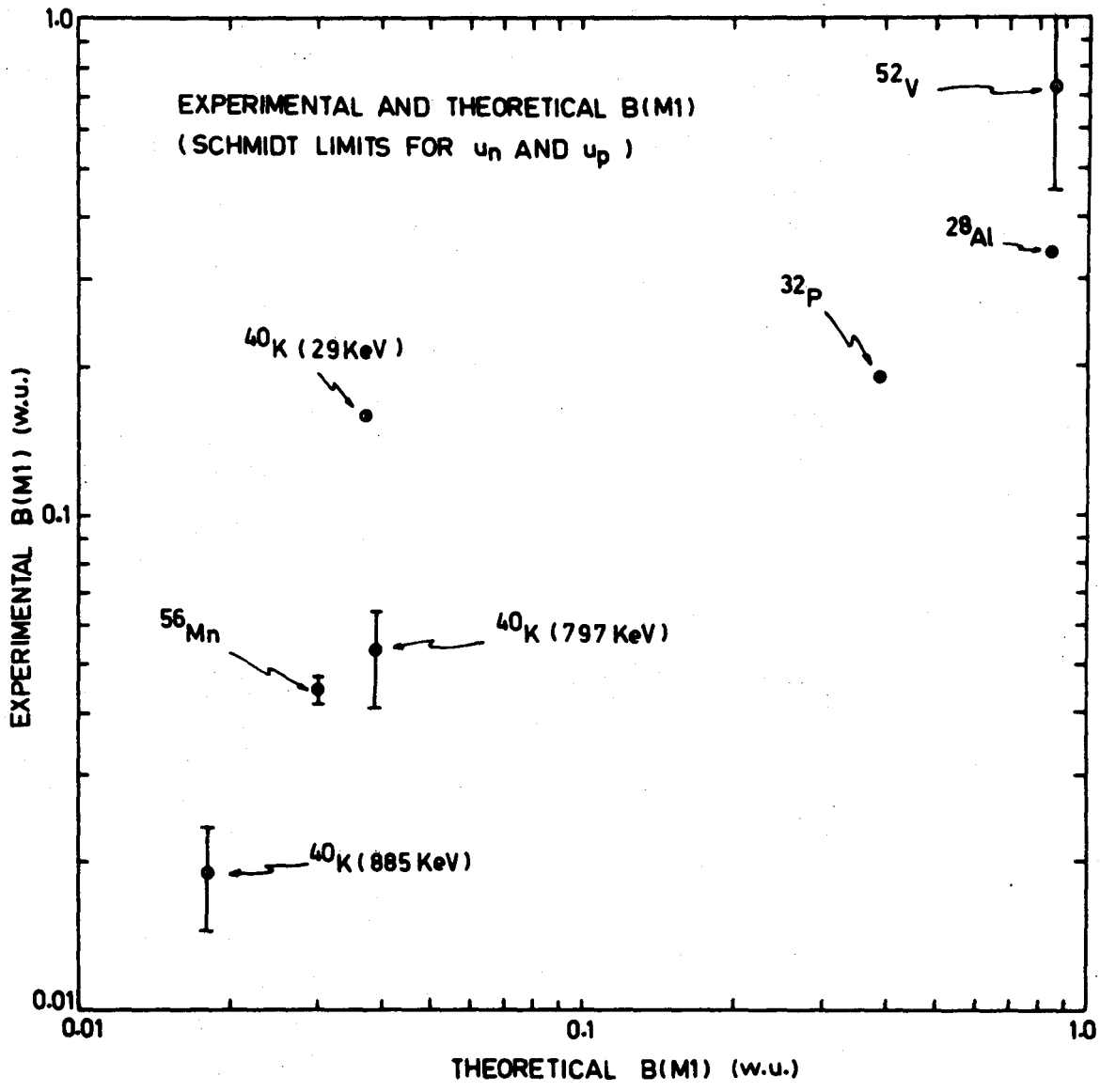

Fig. VII.3 Comparison of the experimental and theoretical B(M1) strengths setting μ_n and μ_p equal to the Schmidt limits.

reduced the correlation coefficient to $\rho = 0.87$ (corresponding to a 99.0% probability for a correlation), indicating that significant nuclear structure effects are manifested in this approach.

B. Correlation With (d,p) Results

Where it is a good approximation to assume that the neutron and proton are in pure shell model states, the above intermultiplet B(M1) treatment could be expected to give a good account of collective and quenching effects which appear in the corresponding odd-A nuclei. Configuration mixing between odd-odd multiplets based on different neutron or proton states, and the effect of the residual neutron-proton interaction is not included, and can lead to errors in the estimate for the theoretical B(M1) strength. Using existing (d,p) reaction data, an analysis has been made to determine if the differences between the experimental B(M1) value and the theoretical prediction can be correlated with the degree of configuration mixing present in the neutron state.

The (d,p) stripping reaction on the target nucleus: core + proton, yields information on the nature of the neutron state in the odd-odd multiplet. The state into which the neutron is transferred is identified by the energy of the proton and the corresponding proton angular distribution, which signifies the angular

momentum transfer to the nucleus, yields the ℓ value or mixture of ℓ values which characterize the neutron state. A spectroscopic factor, S, which measures the ratio of the observed (d,p) cross section to the cross section expected for transfer of the neutron into a pure single particle state can be defined as:

$$S = \frac{\left[\frac{d\sigma}{d\omega}\right]_{exp}}{\left[\frac{d\sigma}{d\omega}\right]_{sp}}$$

$$= \frac{\left[\frac{d\sigma}{d\omega}\right]_{exp}}{(2J+1)\left[\frac{d\sigma}{d\omega}\right]_{sp'}}$$

In the second expression, the J dependence of the theoretical single particle cross section has been factored out, leaving the term $\left[\frac{d\sigma}{d\omega}\right]_{sp'}$ which contains the remaining terms in the cross section. Because of the difficulty in measuring absolute reaction cross sections, it is useful to compare relative spectroscopic factors. For 2 multiplet states, A and B, in which the neutrons and protons are in the same shell model states, so that the $\left[\frac{d\sigma}{d\omega}\right]_{sp'}$ term is the same for the 2 states, the ratio of spectroscopic factors is given by:

$$\Omega = \frac{S_A}{S_B} = \frac{(2J_B + 1)}{(2J_A + 1)} \frac{\left[\frac{d\sigma_A}{d\omega}\right]_{exp}}{\left[\frac{d\sigma_B}{d\omega}\right]_{exp}}$$

This ratio, which equals 1 for pure shell model states, is then a measure of the amount of configuration mixing present in the neutron state.

The experimental (d,p) results for the 5 nuclei are listed in Table VII.2. The correlation between $| 1 - \Omega |$ and the quantity

$$R = 1 - \frac{\text{experimental B(M1)}}{\text{theoretical B(M1)}}$$

was calculated for 6 of the transitions, (the 3 levels in ^{56}Mn were not included because of the ambiguity in the neutron and proton states), and the result: $\rho = -0.13$ represents a negligible correlation. When experimental information on the nature of the proton states becomes available, e.g. from proton transfer reactions, it would be interesting either to make a more careful attempt to interpret the B(M1) discrepancies or to re-calculate the B(M1) values using improved estimates for the neutron and proton states.

C. Correlation With an Undetected E2 Mixture

Since the intensity of the E2 component has only

TABLE VII.2

SUMMARY OF (d,p) STRIPPING RESULTS

Nucleus	Energy (keV)	Spin	(2J + 1)S (relative)
^{28}Al	0	3^+	0.150 (ℓ_n=0)
	30	2^+	0.080 (ℓ_n=0)
^{32}P	0	1^+	0.20 (ℓ_n=0), 3.0(ℓ_n=2)
	77	2^+	4.25 (ℓ_n=2)
^{40}K	0	4^-	0.086 (ℓ_n=3)
	29	3^-	0.0017 (ℓ_n=1), 0.073 (ℓ_n=3)
	800	2^-	0.055 (ℓ_n=3)
	890	5^-	0.100 (ℓ_n=3)
^{52}V	0	3^+	1.00 (ℓ_n=1)
	17	2^+	3.25 (ℓ_n=1)
	23	5^+	
^{56}Mn	0	3^+	0.60 (ℓ_n=1), 1.5 (ℓ_n=3)
	27	2^+	0.85 (ℓ_n=1), 1.4 (ℓ_n=3)
	110	1^+	1.8 (ℓ_n=1)

been experimentally measured for the cases of ^{52}V and ^{56}Mn, an attempt was made to determine the influence of a possible undetected E2 mixture on the remaining 5 transitions. An E2 mixture of fractional intensity I(E2) present in any of the 5 transitions which were assumed to be pure M1 would lead to an overestimate of the experimental B(M1) strength by the fraction $\frac{I(E2)}{I(M1)}$ (Chapter V (J)), where I(M1) is the intensity of the M1 component. Using the Weisskopf estimates, the mass and energy dependence of the M1 and E2 transition probabilities are given by:

$$T(M1) \propto E_\gamma^3$$

$$T(E2) \propto A^{4/3} E_\gamma^5$$

For a transition in which M1 - E2 mixing is allowed, the size of the E2 component is then given by

$$\frac{I(E2)}{I(M1)} = \frac{T(E2)}{T(M1)} \propto A^{4/3} E_\gamma^2$$

The Weisskopf estimates are only expected to give an approximate estimate for the M1-E2 mixing. However, since the factor $A^{4/3} E_\gamma^3$ varied over a range of 1000 for the 5 transitions, which is much larger than the experiment <u>vs</u> theory variation expected for the Weisskopf

estimates, a significant correlation between the true intensity of the undetected E2 mixture and the quantity

$$R = \left| 1 - \frac{\text{experimental B(M1)}}{\text{theoretical B(M1)}} \right|$$

would then be expected to introduce a correlation between $A^{4/3} E_\gamma^2$ and R. The correlation coefficient between the quantities $A^{4/3} E_\gamma^2$ and R was calculated for the 5 transitions and the result, $\rho = -0.55$, indicates that the differences between the experimental and theoretical B(M1) strengths cannot be explained only in terms of an undetected E2 component. This result does not rule out the possibility of individual experimental B(M1) values being significantly affected by an undetected E2 mixture, but only that no systematic dependence could be found.

D. Summary of Low Energy Nuclear Properties

1. Introduction

The properties of the low lying energy levels for the 5 nuclei are summarized in this section. With the exceptions of ^{28}Al, which is assumed to be a distorted nucleus, and ^{56}Mn which displays a large amount of

configuration mixing and could possibly also be distorted (CO68), the shell model appears able to give a reasonable description of the low energy properties of the nuclei in this mass range.

2. ^{28}Al

The 3^+ (ground state) and 2^+ (31 keV) members of the ^{28}Al ground state multiplet were assumed to be formed by coupling a neutron in a $1/2^+$ (211) Nilsson orbit to a $(1d_{5/2})^5$ or $5/2^+$ (202) proton state. The (d,p) reaction (EN67) gives pure $\ell_n = 0$ stripping for the ground and 31 keV levels and the experimental ratio of reduced widths, 7 : 3.7 is to be compared with the theoretical ratio 7 : 5 for pure shell model states. The experimental conversion coefficient for the 31 keV transition, $\alpha_{exp} = 0.032 \pm 0.066$ (SH54), is consistent with a pure M1 assignment.

3. ^{32}P

A $(1d_{3/2})^1$ neutron state was assumed to couple to a $(2s_{1/2})^1$ or $1/2^+$ (211) proton state to form the 1^+ and 2^+ members of the ground state multiplet. In agreement with Nordheim's strong rule (NO50), the 1^+ level forms the ground state while the 2^+ level is at an excitation energy of 77 keV. From the (d,p) reaction (HO62), the 77 keV shows predominantly $\ell_n = 2$ stripping while the ground state was found to contain a 7%

mixture of $\ell_n = 0$ component. The experimental ratio of reduced widths for the 1^+ and 2^+ levels, 3.5 : 5 is close to the value 3 : 5 expected for pure shell model states.

4. ^{40}K

A proton in a $(1d_{3/2})^3$ state was assumed to couple to a $(1f_{7/2})^1$ neutron state to form the 2^-, 3^-, 4^- and 5^- members of the ground state multiplet. In agreement with the revised rules of Brennen and Bernstein (BR60) the 4^- level forms the ground state. With the exception of the 3^- state at 29 keV which contains a 2.3% mixture of $\ell_n = 1$ component, the (d,p) stripping reaction (EN59, EN66) indicates the 2^- state at 797 keV, the 4^- ground state, and the 5^- state at 885 keV all to be relatively pure $\ell_n = 3$. The experimental ratio of reduced stripping widths for the 2^-, 3^-, 4^- and 5^- states, 6.1 : 8.4 : 9.8 : 11 is in good agreement with the shell model estimate, 5 : 7 : 9 : 11.

5. ^{52}V

A proton in a $(1f_{7/2})^3$ state was assumed to couple to a $(2p_{3/2})^1$ neutron state to form the 4 members of the ground state multiplet: 3^+ (ground state), 2^+ (17 keV), 5^+ (23 keV) and 4^+ (148 keV). A 20 keV level observed by Catala et al (CA65) in a (d,p) reaction study probably consists of the unresolved 2^+ level at

17 keV and the 5^+ level at 23 keV. The stripping strength for this "20 keV" level was found to be 3.25 times stronger than for the ground state. Assuming the contributions to be proportional to 2J + 1 gives a strength of $\frac{5}{16}$ x 3.25 = 1.0 for the 2^+ level and a strength of $\frac{11}{16}$ x 3.25 = 2.25 for the 5^+ level. In this (d,p) experiment, the 4^+ member of the ground state multiplet at 148 keV was unresolved from a 1^+ level at 142 keV from a different multiplet, so that the stripping strenth for the 4^+ level cannot be estimated. The experimental ratio of the reduced widths for the 2^+, 3^+ and 5^+ levels is then 4.5 : 4.5 :11 compared with the shell model prediction 5 : 7 : 11.

The experimental conversion coefficient for the 17 keV transition which has been measured here, α_{exp} = 4.6 $\pm$ 1.8 gives a 90% M1 and 10% E2 mixture. The 148 keV level can decay by an M1 transition to the 22 keV level and to the ground state. The B(M1) strength for each transition can be assumed to be proportional to the γ-ray intensity divided by the energy cubed. Using the intensities: I (125 keV) = 17.2 and I (148 keV) = 3.8 from (AR67), gives an estimate for the ratio:

$$R = \frac{B(M1) \text{ for } 148 \rightarrow 22 \text{ keV transition}}{B(M1) \text{ for } 148 \rightarrow 0 \text{ keV transition}} = 7.5$$

which is in poor agreement with the theoretical inter-multiplet B(M1) ratio estimate: $R = \frac{.183}{.237} = 0.77$. The

halflife predicted for the 148 keV level, obtained by summing the theoretical intermultiplet decay constants, is 20 ps.

6. ^{56}Mn

As observed in Fig. VII.1, both the $(f^5_{7/2}, 7/2)$ and $(f^5_{7/2}, 5/2)$ proton states, and the $p_{3/2}$ and $p_{1/2}$ neutron states lie close in energy in the neighbouring odd-odd nuclei, and the ordering of both pairs of levels is inverted by the addition of 2 nucleons of the other type to the core. The (d,p) stripping results (CO68) however show a large $\ell_n = 3$ mixture in addition to the expected $\ell_n = 1$ component. The $\ell_n = 3$ stripping strength for the 3^+ ground state was found to be 2.5 times stronger than the $\ell_n = 1$ component and 1.7 times stronger than the $\ell_n = 1$ component for the 2^+ level at 27 keV. The 1^+ level at 110 keV showed predominantly $\ell_n = 1$ stripping with an upper limit of 30% placed on the $\ell_n = 3$ component. Therefore the $f_{5/2}$ neutron orbit, which is at an energy of 520 keV in ^{55}Cr and 136 keV in ^{57}Cr, must be included in the interpretation of the low energy properties of ^{56}Mn in addition to the $p_{1/2}$ and $p_{3/2}$ orbits.

The measured conversion coefficients for the 84 keV ($1^+ \rightarrow 2^+$) and 27 keV ($2^+ \rightarrow 3^+$) transitions both show considerable E2 mixing with the M1 component. The 1% E2 mixture in the 27 keV transition, and the 45%

E2 mixture in the 84 keV transition correspond, respectively, to the large E2 enhancements of 1700 w.u. and 660 w.u., which is further evidence that ^{56}Mn may be a distorted nucleus.

The theoretical B(M1) values corresponding to 3 different neutron-proton configurations were calculated for the 27 keV transition (section A of this chapter), and with the exception of the $(p_{1/2})_n\ (f^5_{7/2},\ 5/2)_p$ configuration, all cases predicted a faster transition speed than was experimentally observed. Without the inclusion of configuration mixing in the intermultiplet B(M1) theory, which could lead to a reduction in the predicted transition speed, definite conclusions regarding the nature of the neutron and proton states in ^{56}Mn probably cannot be obtained from the B(M1) results. Because of the different ℓ_n characters of the 110 keV and 27 keV levels, implying a large single particle transition component, the theoretical B(M1) strength for the 85 keV transition was not calculated.

E. Conclusion

As a first step in improving the theoretical calculation, either the neutron or proton state in the odd-odd nucleus could be assumed to consist of a mixture of 2 shell model states. Two additional quantities: a mixing parameter and a third magnetic dipole moment

would then be required. The magnetic moment would be that of an excited state in an odd-A nucleus, however these moments have not been measured for the 5 cases considered here. The mixing parameter for each odd-odd nucleus would be chosen so as to be consistent with all available experimental information, but such a treatment is beyond the scope of this thesis. In addition, since there is a general lack of knowledge of the experimental conversion coefficients which are used to determine the M1-E2 mixing ratios, the accuracy of the B(M1) values may not be high enough to warrant the use of fitted parameters. The basic validity of this approach has been established here however, and it is evident that this model can serve as a starting point for more refined calculations.

APPENDIX I

In this appendix the statistical error in the n^{th} moment estimate for τ is calculated. It is assumed that there is no prompt component, i.e. $\eta = 1$, and that the prompt response is a δ-function.

The experimental delayed spectrum, $d(t)$, is then equal to $f(t)$:

$$d(t) = \frac{N_o}{\tau} e^{-t/\tau}$$

where N_o is the total number of counts in the spectrum. The n^{th} moment of $d(t)$ about zero is

$$M_n(d) = \frac{N_o}{\tau} \int_o^\infty t^n \, e^{-t/\tau} \, dt$$

$$= N_o \, n! \, \tau^n$$

For a discrete distribution:

$$d_i = \frac{N_o}{\tau} e^{-t_i/\tau}$$

the error in the n^{th} moment of d_i, defined as $\varepsilon_i(M_n)$, due to the error in the i^{th} data point, defined as $\varepsilon_i = \sqrt{d_i}$, is

$$\varepsilon_i \, (M_n) = t_i^n \, \varepsilon_i$$

$$= t_i^n \left[\frac{N_o}{\tau} e^{-t_i/\tau} \right]^{1/2}$$

The total statistical error in the n^{th} moment due to all data points is $\varepsilon(M_n)$ where

$$\varepsilon^2(M_n) = \sum_i \varepsilon_i^2(M_n)$$

$$= \sum_i t_i^{2n} \frac{N_o}{\tau} e^{-t_i/\tau}$$

Returning to the continuous distribution and replacing the sum by an integral gives

$$\varepsilon^2(M_n) = \frac{N_o}{\tau} \int_o^\infty t^{2n} e^{-t/\tau} dt$$

$$= N_o (2n)! \tau^{2n}$$

The fractional error in the n^{th} moment is then

$$\varepsilon_n = \frac{\varepsilon(M_n)}{M_n(f)}$$

$$= \frac{\sqrt{(2n)!}}{n!} \frac{1}{\sqrt{N_o}}$$

The error in the n^{th} moment estimate for τ (assuming $\eta = 1$ and $p(t) = \delta(0)$) is proportional to $[M_n(d)]^{1/n}$.

Neglecting the error in the centroid position, the error in τ due to the error in the n^{th} moment is then

$$\varepsilon_n(\tau) = \frac{\varepsilon_n}{n\tau}$$

$$\varepsilon_n(\tau) = \frac{\sqrt{(2n)!}}{nn!} \frac{1}{\sqrt{N_o}} \text{ (no centroid variance)} \qquad \text{A1.1}$$

Since the higher moments are calculated about the centroid of the distribution, an error will be introduced in τ because of the statistical error in the centroid position. For $n \geq 2$ the error in τ due to the centroid variance is

$$\varepsilon_n(CV) = \varepsilon_1 = \sqrt{\frac{2}{N_o}}$$

For 2 variates x, y and for z = f(x,y), the corresponding errors are related:

$$\sigma_z^2 = \left[\frac{\partial f}{\partial x}\right]_{\bar{x}} \sigma_x^2 + \left[\frac{\partial f}{\partial y}\right]_{\bar{y}}^2 \sigma_y^2 + 2\left[\frac{\partial f}{\partial x}\right]_{\bar{x}} \left[\frac{\partial f}{\partial y}\right]_{\bar{y}} \sigma_{xy}$$

$$= \alpha^2 + \beta^2 + \gamma$$

If γ can be constrained to $-2\alpha\beta \leq \gamma \leq 2\alpha\beta$ then $(\alpha-\beta)^2 \leq \sigma_z^2 \leq (\alpha+\beta)^2$.

Thus neglecting the covariance between the error in the

n^{th} moment and the error in the centroid position, upper and lower limits for the total fractional error in the n^{th} moment estimate for τ, $\varepsilon'_n(\tau)$ can be obtained by linearly combining the 2 errors:

$$\varepsilon'_n(\tau) = \left| \varepsilon_n(\tau) \pm \varepsilon_n(CV) \right|$$

An upper limit for the total error in the n^{th} moment estimate for τ is then

$$\varepsilon'_n(\tau) = \varepsilon_n(\tau) + \varepsilon_n(CV)$$

$$\varepsilon'_n(\tau) = \frac{1}{\sqrt{N_o}} \left[\frac{\sqrt{(2n)!}}{nn!} + \sqrt{2} \right] \text{(including centroid variance)}$$

A1.2

REFERENCES

AN60 N. D'Angelo, Phys. Rev. 117, 510 (1960)

AR60 N. P. Archer, W. V. Prestwich and G. L. Keech, Nucl. Instr. and Meth. 44, 114 (1960)

AR67 N. P. Archer and T. J. Kennett, Can. J. Phys. 45, 2683 (1967)

AS66 P. Van Assche, U. Gruber, B. P. Maier, H. R. Koch, and O. W. B. Schult, Nucl. Phys. 84, 661 (1966)

AS66 P. Van Assche, U. Gruber, B. P. Maier, H. R. Koch, O. W. B. Schult and J. Vervier, Nucl. Phys. 79, 565 (1966)

BA60 E. Bashandy, Nucl. Instr. and Meth. 6, 289 (1960)

BA50 Z. Bay, Phys. Rev. 77, 419 (1950)

BA55 Z. Bay, V. P. Henri and H. Kanner, Phys. Rev. 100, 1197 (1955)

BA68 C. A. Baker, C. J. Batty and L. E. Williams, Nucl. Instr. and Meth. 59, 125 (1968)

BE66a G. Bertolini, M. Cocchi, V. Mandl and A. Rota, IEEE Tran. Nucl. Sci. NS-13, 119 (1966)

BE66b G. Bertolini, V. Mandl and A. Rota, Nucl. Instr. and Meth. 42, 109 (1966)

BE67 E. Ye. Berlovich and V. V. Lukashevich, Nucl. Instr. and Meth. 55, 323 (1967)

BE69 B. Bengtson and M. Moszynski, Nucl. Instr. and Meth. 75, 152 (1969)

BI59 M. Birk, G. Goldring and Y. Wolfson, Phys. Rev. 116, 730 (1959)

BI64 J. B. Birks, The Theory and Practice of Scintillation Counting (Pergamon Press, 1964)

BO68 H. H. Bolotin, Phys. Rev. 168, 1317 (1968)

BO69 J. F. Boulter, W. V. Prestwich and B. Arad, Can. J. Phys. 47, 591 (1969)

BO70a J. F. Boulter, W. V. Prestwich and T. J. Kennett, Nucl. Instr. and Meth. 77, 163 (1970)

BO70b J. F. Boulter and W. V. Prestwich, Can. J. Phys. 48, 868 (1970)

BO70c J. F. Boulter, W. V. Prestwich and B. Arad, Nucl. Instr. and Meth. 83, 29 (1970)

BR65a J. Braunsfurth and H. J. Körner, Nucl. Instr. and Meth. 34, 202 (1965)

BR60 M. H. Brennan and S. A. Bernstein, Phys. Rev. 120, 927 (1960)

BR65b G. Brianti, Report CERN 65-10 (1965)

CA65 J. Catala, A. Garcia, J. M. Bolta, S. Hinds, H. Marchant and A. E. Forest, Nucl. Phys. 74, 1 (1965)

CH67 Z. H. Cho, L. Gidefeldt and L. Eriksson, Nucl. Instr. and Meth. 52, 273 (1967)

CO68 J. R. Comfort, Ph.D. Thesis, Yale University (1968)

CR60 E. L. Crow, F. A. Davis and M. W. Maxfield, Statistics Manual (Dover, New York, N.Y., 1960)

CU61 W. M. Currie, R. E. Azuma and G. M. Lewis, Nucl. Instr. and Meth. 13, 215 (1961)

DO70 S. Donati, E. Gatti and V. Svelto, Nucl. Instr. and Meth. 77, 179 (1970)

EG64 EG & G Nano-Notes, Time-to-Height Converter Calibration 1, No. 2 (Jan. 1964)

EN59 H. A. Enge, E. J. Irwin and D. H. Weaner, Phys. Rev. 115, 949 (1959)

EN66 H. A. Enge, Introduction to Nuclear Physics, (Addison-Wesley Publishing Company, Inc., Reading Mass., 1966)

EN67 P. M. Endt and C. Van der Leun, Nucl. Phys. 105, 1 (1967)

ES61 I. V. Estulin, A. S. Melioransky and L. F. Kalinkin, Nucl. Phys. 24, 118 (1961)

FO68 D. B. Fossan, C. Chasman and K. W. Jones, Phys. Rev. 168, 1200 (1968)

FR62 J. E. Freund, P. E. Livermore and I. Miller, Manual of Experimental Statistics (Prentice-Hall Inc., Englewood Cliffs, N.J., 1962)

GA66 E. Gatti and V. Svelto, Nucl. Instr. and Meth. 43, 248 (1966)

GE66 J. S. Geiger, R. L. Graham, I. Bergström, and F. Brown, Nucl. Phys. 68, 352 (1966)

GE67 D. A. Gedcke and W. J. McDonald, Nucl. Instr. and Meth. 55, 377 (1967)

GE68 D. A. Gedcke and W. J. McDonald, Nucl. Instr. and Meth. 58, 253 (1968)

GR62 R. L. Graham, J. S. Geiger, R. L. Bell and R. Barton, Nucl. Instr. and Meth. 15, 40 (1962)

GR65 R. C. Greenwood and J. H. Reed, AEC Report TID4500 (1965)

HA59 Handbook of Chemistry and Physics, (Chemical Rubber Publishing Company, Cleveland, Ohio)

HA65 D. W. Hafemeister and E. B. Shera, Phys. Rev. Lett. 15 593 (1965)

HA69 R. S. Hager and E. C. Seltzer, Nuclear Data Tables A6, 1 (1969)

HE68 L. C. Henry and T. J. Kennett, Can. J. Phys. 46, 1984 (1968)

HE70 L. J. Heistek and L. Van der Zwain, Nucl. Instr. and Meth. 80, 213 (1970)

HO62 T. Holtebekk, Nucl. Phys. 37, 353 (1962)

HO68 A. Houdayer, S. K. Mark and R. E. Bell, Nucl. Instr. and Meth. 59, 319 (1968)

HU66 L. B. Hughes, T. J. Kennett and W. V. Prestwich, Nucl. Phys. 80, 131 (1966)

JE58 J. V. Jelley, Čerenkov Radiation and its Applications (Pergamon Press, 1958)

JO68 F. A. Johnson, Nucl. Instr. and Meth. 59, 237 (1968)

JO70a F. A. Johnson, Nucl. Instr. and Meth 78, 1 (1970)

JO70b L. V. Johnson and T. J. Kennett, Can. J. Phys. 48, 1109 (1970)

KA66 R. Kästner, A. Andreef and P. Manfrass, in International Conference on the Study of Nuclear Structure with Neutrons (North Holland Publishing Co., Amsterdam, 1966), p. 515.

KE67 Cordon R. Kerns, IEEE Tran. Nucl. Sci. NS-14, No.1, 449 (1967)

KR65 H. R. Krall, IEEE Tran. Nucl. Sci. NS-12, 39 (1965)

LE67 C. M. Lederer, J. M. Hollander and I. Perlman, Table of Isotopes, 6th Edition (John Wiley and Sons, Inc., 1967)

LY59 F. J. Lynch and R. E. Holland, Phys. Rev. 114, 825 (1959)

LY66 F. J. Lynch, IEEE Tran. Nucl. Sci. NS-13, 140 (1966)

LY67 H. Lycklama and T. J. Kennett, Can. J. Phys. 45, 3039 (1967)

LY69 H. Lycklama, T. J. Kennett and L. B. Hughes, Can. J. Phys. 47, 665 (1969)

MA68 I. G. Main, N. Dawson, D. Kewley, N. Lawley, M. F. Thomas and P. J. Twin, Phys. Rev. Lett. 26B, 295 (1968)

MC65 R. L. McGuire, E. C. Yates, D. G. Crandall and C. R. Hatcher, IEEE Tran. Nucl. Sci. NS-12, No. 1, 24 (1965)

ME61 E. Merzbacher, Quantum Mechanics, (John Wiley and Sons, Inc., 1961)

ME67 R. A. Mendelson Jr., Ph.D. Thesis, University of Iowa (1967)

ME68 R. A. Mendelson, Jr., and R. T. Carpenter, Phys. Rev. 165, 165 (1968)

MI66 J. A. Miehe, E. Ostertag and A. Coche, IEEE Tran. Nucl. Sci. NS-13, 127 (1966)

MO Motorola Integrated Circuit Application Notes, AN409 (Multivibrator), AN417 (100 Mhz Oscillator), AN418 (Shaper)

MO53 S. A. Moszkowski, Phys. Rev. 89, 474 (1953)

MO68 G. A. Morton, H. M. Smith and H. R. Krall, Publication No. ST-3881, RCA Electronic Components, Princeton, New Jersey, (1968)

MR65 W. R. Mruk, Nucl. Instr. and Meth. 35, 61 (1965)

NE50 T. D. Newton, Phys. Rev. 78, 490 (1950)

NO50 L. W. Nordheim, Phys. Rev. 78, 294 (1950)

OG68 A. Ogata, S. J. Tao and J. H. Green, Nucl. Instr. and Meth. 60, 141 (1968)

PO50 R. F. Post and L. I. Schiff, Phys. Rev. 80, 1113 (1950)

PR70 G. Present and D. B. Scarl, Rev. Sci. Instr. 41, 771 (1970)

PR62 M. A. Preston, Physics of the Nucleus (Addison-Wesley, Reading, Mass., 1962)

RC RCA Phototubes and Photocells (Technical Manual PT-60)

RU65 S. L. Ruby and R. E. Holland, Phys. Rev. Lett. 15, 591 (1965)

SC63 Arthur Schwarzschild, Nucl. Instr. and Meth. 21, 1 (1963)

SE70 R. E. Segal, G. B. Beard and G. H. Wedberg, Argonne National Laboratory Report ANL-7728 (March 1970)

SI67 B. Sigfridsson, Nucl. Instr. and Meth. 54, 13 (1967)

ST57 E. Storm, E. Gilbert and H. Israel, Gamma Ray Absorption Coefficients, Los Alamos Scientific Laboratory, University of California, Los Alamos, N. M., Report LA-2237 (1957)

TA68 H. E. Taylor, Nucl. Instr. and Meth. 59, 237 (1968)

TA69 H. E. Taylor, Nucl. Instr. and Meth. 68, 160 (1969)

TH62 P. Thieberger, Arkiv. Fysik 22, 127 (1962)

TO61 S. J. du Toit and L. M. Bollinger, Phys. Rev. 123, 629 (1961)

TS68 P. K. Tseng, S. L. Ruby and D. H. Vincent, Phys. Rev. 172, 249 (1968)

VO62 A. De Volpi and K. G. Porges, IRE Trans. Nucl. Sci. NS-7, 320 (1962)

WA70 M. A. El-Wahab and M. A. El-Salam, Nucl. Instr. and Meth. 78, 325 (1970)

WE60 R. S. Weaver and R. E. Bell, Nucl. Instr. and Meth. 9, 149 (1960)

WE51 V. F. Weisskopf, Phys. Rev. 83, 1073 (1951)

WH65 D. H. White, B. G. Saunders, W. John and R. W. Jewell, Jr., Nucl. Phys. 72, 241 (1965)

YA66 E. C. Yates and D. G. Crandall, IEEE Tran. Nucl. Sci. NS-13, 153 (1966)

YO62 H. D. Young, Statistical Treatment of Experimental Data (McGraw-Hill, New York, N.Y., 1962)